uOttawa

L'Université canadienne
Canada's university

FACULTÉ DES ÉTUDES SUPÉRIEURES ET POSTOCTORALES

uOttawa

L'Université canadienne
Canada's university

FACULTY OF GRADUATE AND POSDOCTORAL STUDIES

Peter Jong Ho Kim
AUTEUR DE LA THÈSE / AUTHOR OF THESIS

M.A.Sc. (Mechanical Engineering)
GRADE / DEGREE

Department of Mechanical Engineering
FACULTÉ, ÉCOLE, DÉPARTEMENT / FACULTY, SCHOOL, DEPARTMENT

Development and Validation of Stimulation Software for RTM and VARTM Processes
TITRE DE LA THÈSE / TITLE OF THESIS

François Robitaille
DIRECTEUR (DIRECTRICE) DE LA THÈSE / THESIS SUPERVISOR

CO-DIRECTEUR (CO-DIRECTRICE) DE LA THÈSE / THESIS CO-SUPERVISOR

Michel Nganbe

Jeremy Laliberté

Gary W. Slater
Le Doyen de la Faculté des études supérieures et postdoctorales / Dean of the Faculty of Graduate and Postdoctoral Studies

Development and validation of simulation software for RTM and VARTM processes

Peter Jong Ho Kim

A thesis submitted to the Faculty of Graduate and Postdoctoral Studies in partial fulfilment of the requirements for the Degree of

MASTER OF APPLIED SCIENCE

In Mechanical Engineering

Ottawa-Carleton Institute for Mechanical and Aerospace Engineering

University of Ottawa

Ottawa, Canada

December 2009

Your file Votre référence
ISBN: 978-0-494-65548-1
Our file Notre référence
ISBN: 978-0-494-65548-1

Abstract

Liquid Composite Moulding (LCM) identifies a group of composite manufacturing processes which have become conventional choices in industry due to their versatility and economic advantages. Resin Transfer Moulding (RTM) and Vacuum Assisted Resin Transfer Moulding (VARTM) have established themselves as the two main LCM options.

In this thesis, a Finite Difference Method (FDM) approach is developed and implemented for predicting the flow of resin during the filling stage of RTM and VARTM. For RTM filling simulation, the discretized partial differential equations are stored in a matrix and solved using a standard numerical solution approach of Lower-Upper Decomposition. For VARTM filling simulation, solutions are obtained using an iterative method. These two different approaches were used as a result of physical differences between the two manufacturing processes, and also for investigation purposes.

The RTM simulation software is capable of simulating flat moulds of any shape and the user can define any positions for the multiple inlet ports and multiple outlet vents. The user controls all the critical parameters for the process such as permeability, viscosity and porosity. Impermeable walls can be inserted in any position in order to simulate complex geometries. The distribution of resin pressure in the cavity can be seen in color scale as well as in actual numbers along with the fill time. Validation of the software was performed by running several RTM experiments and comparing the experimental and simulated flow patterns, as well as the fill times.

The VARTM simulation software is developed in 1D where the important parameters such as permeability and porosity behave as variables. The governing equations are developed and discretized. The 1D solution is compared visually and numerically other results obtained from a creditable source.

Acknowledgements

First of all, I would like to show my deepest gratitude to my research supervisor Dr. Francois Robitaille for his devoted support and guidance throughout the research. As a teacher, a mentor, and a friend, I could not have asked for anyone better. Once again, my sincere appreciation goes out to him.

I also need to thank my colleagues from B-08D for sharing quality times together in and out of the faculty: Nicholas Burnford, Zachary Doerr, Patrick Dumond, Veronique Millette, Shaun Saborin, Reza Samadi, and Edem Sena.

Finally, my special thanks go out to my family for their continuous love and support throughout the ups and downs. I also would like to dedicate this thesis to my grandparents in Korea.

Table of Contents

List of Figures

List of Tables

Nomenclature

Roman letters		Units
A	Total cross-section area	m^2
AMP	Amplitude of vector movement	
$\hat{e}_z$	Unit vector in z direction	
g	Acceleration due to gravity	m/s^2
$\vec{g}$	Vector form of gravity	m/s^2
h	Local material thickness	m
h_{layer}	Thickness of a single preform layer	m
$IAMP$	Ideal amplitude of vector movement	
$i-1$	Node to the left of node i in a rectangular grid	
$i+1$	Node to the right of node i a rectangular grid	
$i-m$	Node one row above node i in a rectangular grid	
$i+m$	Node one row below node i in a rectangular grid	
K	Permeability	m^2
K_x	Permeability along direction x	m^2
K_y	Permeability along direction y	m^2
k	Kozeny constant	m^2
l	Distance between nodes	m
M_{NET}	Net mass flow	kg
$\overrightarrow{MR}$	Right hand term movement vector	

$\overrightarrow{MX}$	x component movement vector	
$\overrightarrow{MY}$	y component movement vector	
$\overrightarrow{MZ}$	z component movement vector	
n	Number of preform layers	
P_0	Atmospheric pressure	Pa
P_c	Compaction pressure	Pa
P_i	Inlet pressure	Pa
P_o	Outlet pressure	Pa
P_r	Resin pressure	Pa
Q	Volume flow rate	$m^3 \cdot s^{-1}$
$\vec{q}$	Vector form of volume flow rate	$m^3 \cdot s^{-1}$
R_f	Radius of the circular flow front	m
R_o	Radius of the inlet port	m
t	Time increment	s
$\vec{u}$	Velocity vector	$m \cdot s^{-1}$
u	Velocity component along direction x	$m \cdot s^{-1}$
u_1	Velocity component along axis 1	$m \cdot s^{-1}$
u_2	Velocity component along axis 2	$m \cdot s^{-1}$
u_3	Velocity component along axis 3	$m \cdot s^{-1}$
$u_{i,j}$	Velocity at point (i, j) in plane x, y	$m \cdot s^{-1}$
$u\overrightarrow{MR}$	Right hand term movement unit vector	

$u\overline{MX}$	x component movement unit vector	
$u\overline{MY}$	y component movement unit vector	
$u\overline{MZ}$	z component movement unit vector	
V_x	Actual velocity in direction x	$m \cdot s^{-1}$
v	Velocity component along direction y	$m \cdot s^{-1}$
v_x	Seepage velocity in direction x	$m \cdot s^{-1}$
v_f	Fibre volume fraction	
W	Distance of separation between two parallel walls for fluid flow	m
w	Velocity component along direction z	$m \cdot s^{-1}$
Δx	Saturated distance along x between two nodes	m
Δy	Saturated distance along y between two nodes	m

Greek letters		**Units**
γ	Specific weight	$N \cdot m^{-3}$
κ	Permeability tensor	m^2
μ	Dynamic viscosity	$Pa \cdot s$
ρ	Density	$kg \cdot m^{-3}$
ϕ	Porosity	

1 Introduction

1.1 Composite Materials

Composite materials – often referred to as 'composites' – are engineering materials made of two distinct constituents: fibres and resin. The fibres are also referred to as the reinforcement, and the resin is also referred to as the matrix. In structural polymer composites, fibres carry the majority of the load; the proportion of load carried by the fibres is much larger than the fraction of volume that they occupy within the composite. Typical fibre volume fractions from 55% to 75% can be reached depending on the fabrication techniques, and more than 98% of the load is usually carried along the fibres. The polymeric resin sets the shape of the composite part and transfers external loads to the fibres while protecting them from damage. Polymer composites are generally much less dense than metals and alloys, yet they generally provide strength and stiffness superior to those of conventional metals when compared on a mass basis. Due to these characteristics, polymer composites have become the materials of choice for many structural engineering components, especially in aerospace and transport applications where it is essential to reduce weight while maintaining structural properties. Fuel consumption of aircraft can be greatly reduced through the use of polymer composites. The following table clearly illustrates the advantage of polymer composites over some common metal alloys.

Table 1-1 Typical material properties [1]

Material	Density (g/cm^3)	Elastic Modulus (GPa)	Cost ($/kg)
Aluminum	2.71	69	7.25 – 10.00
Titanium	4.51	103	28.00 – 65.00
Stainless Steel	8.00	193	2.15 – 3.50
Carbon-Epoxy Composite	1.70	220 (longitudinal) 6.9 (transverse)	175 – 225

1.2 Resin Transfer Moulding (RTM) and Vacuum Assisted Resin Transfer Moulding (VARTM)

Resin Transfer Moulding (RTM) is a type of Liquid Composite Moulding (LCM) process in which a thermoset resin is injected into a closed mould with a fibrous reinforcement or preform already in place. This process is commonly used in the composites industry as it can be highly automated and yields finished products with excellent surface finish and dimensional tolerances.

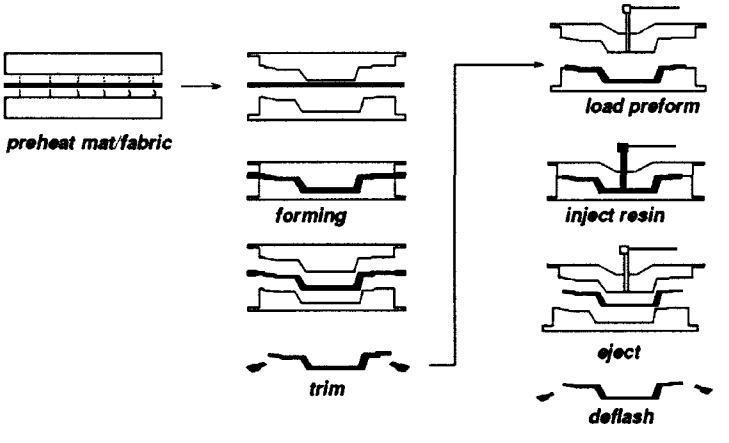

Figure 1-1 RTM process [2].

Vacuum Assisted Resin Transfer Moulding (VARTM) is an alternative version of RTM where the resin is drawn in the preform using a partial vacuum instead of being injected under imposed pressure. VARTM has advantages over RTM, primarily the fact that only one rigid half-mould is required for tooling instead of two. In VARTM, a vacuum film and flow-enhancing ancillaries are placed over the preform and mould, which is sealed. The imposed vacuum also allows the preform to compact prior to infusion.

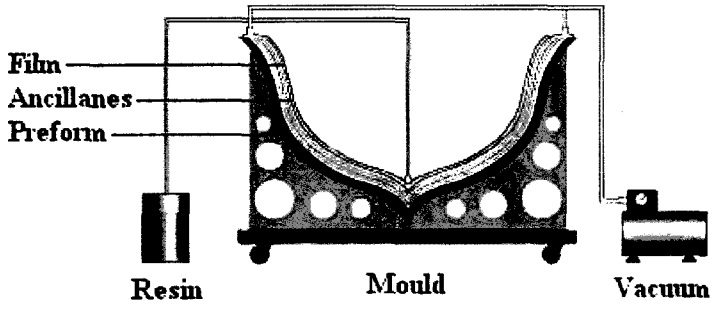

Figure 1-2 VARTM process [3].

RTM and VARTM are favoured options for liquid composite moulding and software packages have been developed to simulate flow front progression, edge effects, fill-time, and pressure distribution [4-7]. Liquid Injection Moulding System (LIMS) from the University of Delaware is a well-known software which is capable of handling the aforementioned cases. It is, however, proprietary. Furthermore, the numerical methods used in this package differ from those used in the present work; here the finite differences (FD) method was used while the finite elements (FE) or finite volumes (FV) are often preferred in commercial codes. Also, nothing is known of the detailed implementation of

the flow front progression algorithm in LIMS or other packages. The implementation developed in this thesis is amenable to further developments which are considered for future work.

1.3 Thesis Overview

The purpose of this work is to develop software capable of predicting resin flow in the RTM and VARTM processes. For the RTM simulation tool, the capability of visualizing the pressure distribution and flow front progression during infusion constitutes the end result of this thesis. The software is also able to process media of different porosity and permeability, while any planar shape and size of preform can be used in simulations. The user controls the critical factors such as locations of inlet or vent ports – thus the optimum configuration for the filling process can be determined from simulation. If desired, multiple inlet or vent ports can be configured to further optimize the filling process. The simulation software was validated numerically by running cases in 1D and 2D, and then comparing the fill times recorded to the values obtained from theoretical solutions. Once the software was validated, actual experiments were simulated and then carefully compared. Flow front shapes and fill timse from the simulations should ideally resemble the values obtained from the actual experiments, since the goal is to develop the software with dependable accuracy so that RTM can be optimized; decreasing waste of labour time, process time, and cost of manufacturing. A similar approach was followed for the development of the VARTM simulation tool – however, the time constraint limited our scope to the development of 1D simulation tool only.

Chapter 1 of this thesis consists of introduction to composite materials as well as to main manufacturing methods: RTM and VARTM. Chapter 2 continues with the literature review on the related topics along with the development of key theories used in the simulation software. It also illustrates examples which explain the implementation of these theories. Chapter 3 introduces the equipments, setup, and procedures that was used during the RTM experiments. Chapter 4 discusses the 7 different simulation cases that were performed, and features comparisons that were made with RTM experiments conducted in the same conditions. A validation for the 1D VARTM software was also made by comparing the results with an authoritative source. Lastly, chapter 5 concludes the thesis with recommendations for future work.

2 Literature Review

2.1 Permeability in Liquid Composite Moulding

French engineer Henry Darcy (1803 – 1858) made a key contribution to the field of flow through porous media with the development of Darcy's law, which is a relationship between the instantaneous flow rate of a fluid through a porous medium, the viscosity of the fluid and the fluid pressure gradient. The initial expression developed by Darcy [4] for the flow of water through a column of sand is:

$$Q = KA\frac{\gamma}{\mu} \tag{2.1}$$

This can be rewritten more generally in 3D vector form with gravity included:

$$\vec{q} = \frac{-\kappa}{\mu}(\nabla P - \rho g \hat{e}_z) \tag{2.2}$$

The negative sign accounts for the fact that fluids flow from high pressures to low pressures. As seen in Equation (2.2), Darcy's law is heavily dependent on permeability. Permeability is an important factor to liquid composite moulding processes as it determines resin flow characteristics in RTM and VARTM. Any simulation of these processes requires permeability data for the reinforcement. Permeability data is also critical to balancing processing and performance aspects in the development of high-permeability fibre reinforcements and high performance composite parts. Thus much

research effort was devoted to developing standard techniques for the measurement of in-plane reinforcement permeability [5-17], and a substantial base of in-plane permeability data became available in the literature. Figure 2-1 displays in-plane radial unsaturated flow measurements done by Parnas *et al.* [18].

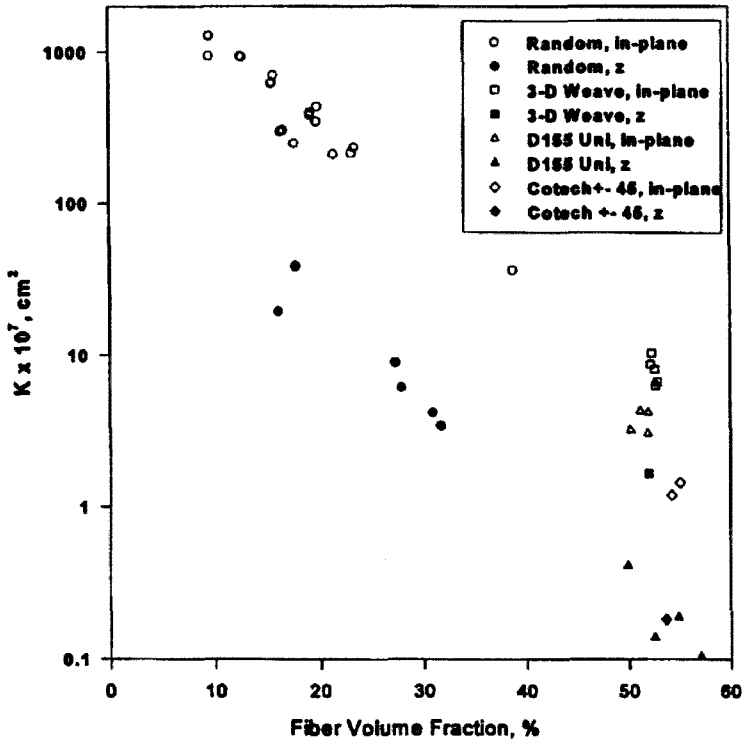

Figure 2-1 Permeability data of various textile reinforcements with different fibre volume fractions

Some key methods for calculating and measuring the permeability related to the work presented in this thesis appear in the work K. L. Adams, B. Miller and L. Rebenfeld [12]. Their work included the analysis of a radial in-plane flow apparatus which they developed; the apparatus allows strict control of all important experimental variables as well as direct observation of the experiment. From the shape and position of the

advancing flow front as a function of time, effective directional permeability values are obtained.

Another related work was done by P. Ferland, D. Guittard and F. Trochu [15], in which they propose concurrent methods for low-cost permeability estimation. The permeability is measured by recording the time at which an advancing flow front reaches various locations; various methods to calculate the permeability are proposed. Figure 2-2 shows the convergence of three different data processing methods: elementary, single point, and interpolation.

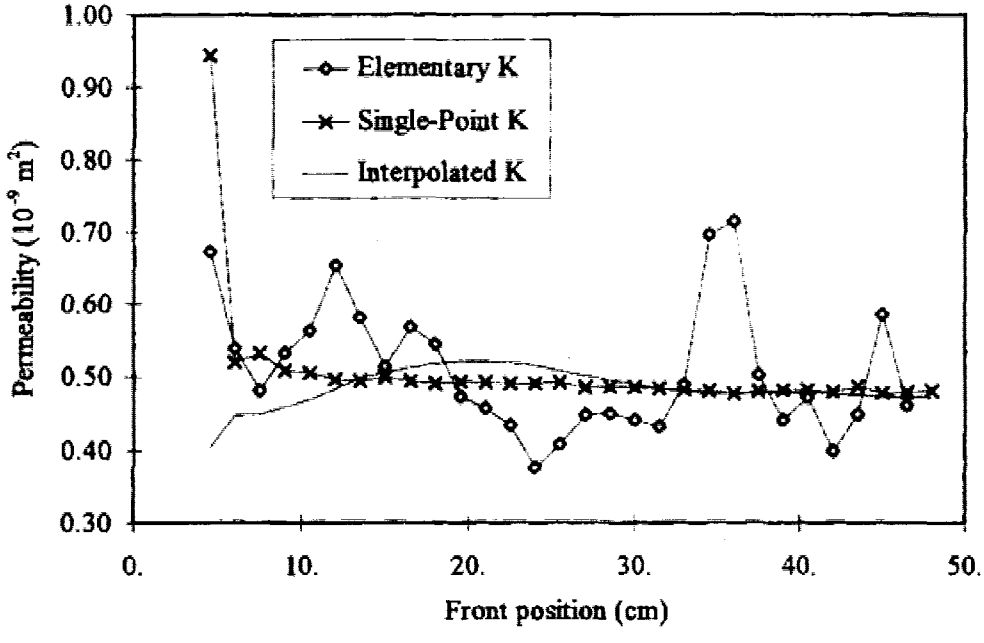

Figure 2-2 Convergence of data processing methods [15]

However, these standard methods disregard many important practical factors such as edge effects [19-24], preform curvature, non-planar geometry [25-29], joints [30], runners [31, 32], surface effects [33] or convergent flows [34]. They are also not designed to handle readily the effects of randomness and local variation inherent to textile structures [35-41]. Such issues pushed many authors to develop models that would predict the permeability of a porous reinforcement from the geometric definition of its structure. A permeability model was developed by Kozeny and Carman [42] who introduced a simple equation for estimation of the permeability for oriented fibres.

$$K = k\frac{\left(1-v_f\right)^3}{v_f^{\,2}} \tag{2.3}$$

The equation relates the permeability and fibre volume fraction through the Kozeny constant *k*. The constant is determined experimentally and it varies with the geometry of the fibre reinforcement. Equation (2.3) still features as the base of many newly developed models and simulations.

Filling simulations for industrial parts require a large amount of permeability data to take into account factors such as local shear, local compaction, local changes in the layout of textiles, ply dropoffs, cuts, and inserts. Moreover, local permeability values vary over uniform zones of a part since textile reinforcements are statistical by nature. Some methods were developed by Lundstrom [43] , Senoguz [44] and Robitaille [45-51] which show credible results in industrial applications.

2.2 Computational Fluid Dynamics (CFD)

Computational fluid dynamics (CFD) are used in numerous engineering problems involving fluid flow, such as the analysis of air flow around airfoils or of streamline patterns for submarines. Modern CFD software features powerful tools that replace explicit integrals or partial derivatives formulations of continuity, momentum and energy equations with discretized algebraic forms. The discretized equations are solved over a set physical domain and in time leading to numerical answers. The convergence of these answers with increased levels of discretization is often used as a criterion for evaluating their validity. CFD software often requires intensive computational power, especially when highly non-linear equations are discretized. Many believe that the biggest influence on the development of supercomputers is indeed the CFD community.

There are many different ways of discretizing partial derivatives to obtain numerical solutions. The three most common methods are the Finite Volume Method (FVM), Finite Element Method (FEM) and Finite Differences Method (FDM). FVM is the most classical approach method and it is widely used in research and commercial codes. FVM is very effective at recasting the partial differential equations of the Navier-Stokes equation in the conservative form and then discretizing it, which guarantees the conservation of fluxes through a particular control volume. However, this method is sensitive to distorted elements which can prevent convergence if such elements are in critical flow regions. Also, the problem at hand for this project is not the solution to the Navier-Stokes equation, thus this method was disregarded. FEM is a popular method for structural analysis of solids as well as for fluids and it has proven to be more stable than

FVM especially for solving the Navier-Stokes equations. However, a FEM formulation requires much more effort in its implementation to ensure a conservative solution. It also requires far more memory than FVM, thus it was disregarded. The method of choice for discretization for this work is FDM, which is the simplest method to implement out of all three. It can also be highly efficient and accurate in dealing with complex geometries – especially when meshing geometries in curvilinear coordinates [52].

2.3 Continuity Equation in Fluid Mechanics

The first governing equation for modelling resin flow in the filling phase of RTM is the continuity equation [53], determined from a classical approach for analysing a fluid-filled volume. This equation can be used to obtain the pressure distribution across the resin-filled zones. An infinitesimally small volume fixed in space with fluid moving through it is considered, with a Cartesian coordinate system adopted where velocity and density are functions of (x, y, z) in space, and of time t.

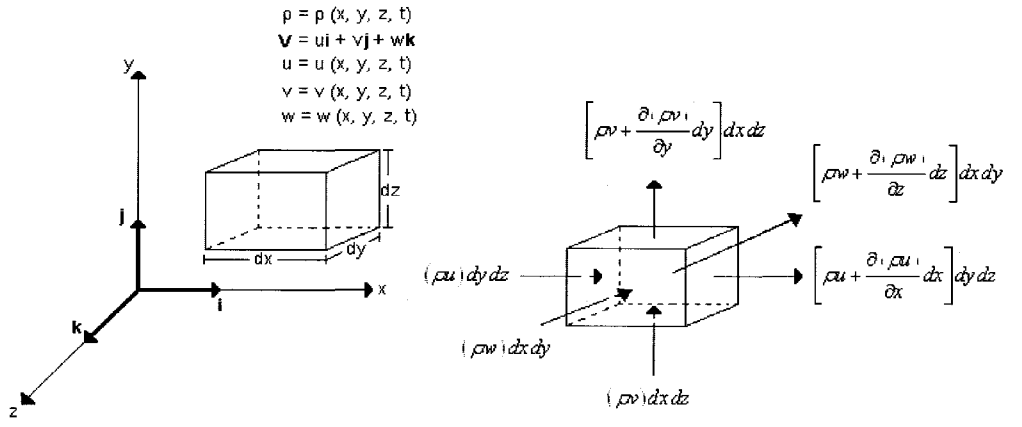

Figure 2-3 Infinitesimal volume fixed in space

The left and right faces of the volume, which are perpendicular to the x axis, have areas $dydz$. Since the velocity is a function of spatial location, the values of the mass fluxes across the left and right faces will differ; this difference is expressed as $\left[\partial(\rho u)/\partial x\right]dy\,dz$. Thus, the mass flows across the right face can be expressed as $\{\rho u+\left[\partial(\rho u)/\partial x\right]\}dy\,dz$. Similarly, the mass flow through both the bottom and top faces which are perpendicular to the y axis, are $(\rho v)dx\,dz$ and $\{\rho v+\left[\partial(\rho v)/\partial y\right]dy\}dx\,dz$, respectively. The mass flows through both the front and back faces, which are perpendicular to the z axis, are $(\rho w)dx\,dy$ and $\{\rho w+\left[\partial(\rho w)/\partial z\right]dz\}dx\,dy$, respectively. By denoting a net outflow of mass as a positive quantity, the net outflows in the x, y and z directions are:

$$\left[\rho u+\frac{\partial(\rho u)}{\partial x}dx\right]dy\,dz-(\rho u)dy\,dz=\frac{\partial(\rho u)}{\partial x}dx\,dy\,dz \tag{2.4}$$

$$\left[\rho v+\frac{\partial(\rho v)}{\partial y}dy\right]dx\,dz-(\rho v)dx\,dz=\frac{\partial(\rho v)}{\partial y}dx\,dy\,dz \tag{2.5}$$

$$\left[\rho w+\frac{\partial(\rho w)}{\partial z}dz\right]dx\,dy-(\rho w)dx\,dy=\frac{\partial(\rho w)}{\partial z}dx\,dy\,dz \tag{2.6}$$

Hence, the net mass flow out of the element is given by:

$$M_{NET}=\left[\frac{\partial(\rho u)}{\partial x}+\frac{\partial(\rho v)}{\partial y}+\frac{\partial(\rho w)}{\partial z}\right]dx\,dy\,dz \tag{2.7}$$

The total mass of fluid in the infinitesimal element is $\rho(dx\,dy\,dz)$; hence the time rate of increase of mass inside the element is given by $\partial\rho/\partial t(dx\,dy\,dz)$. The principle of mass conservation can be expressed in words as: the net mass flow out of the element must equal the time rate of decrease of mass inside the element. Denoting the mass decease by negative quantities, this statement can be expressed in terms of Equations (2.7) and (2.8) as:

$$\frac{\partial\rho}{\partial t}+\left[\frac{\partial(\rho u)}{\partial x}+\frac{\partial(\rho v)}{\partial y}+\frac{\partial(\rho w)}{\partial z}\right]=\frac{\partial\rho}{\partial t}+\nabla\cdot(\rho\vec{u})=0 \tag{2.8}$$

Since the problem of solving the resin pressure field is independent of time, the problem at hand reduces to steady-state flow of an incompressible fluid. The relation can be simplified to:

$$\nabla \cdot (\vec{u}) = \frac{\partial u_1}{\partial x} + \frac{\partial u_2}{\partial y} + \frac{\partial u_3}{\partial z} = 0 \tag{2.9}$$

When modeling the actual resin flow, the time variable is introduced and the problem is no longer a case of steady-state flow. The detail of formulation and solution to this problem is discussed in section 2.10.

2.4 Momentum Equation in Fluid Mechanics: Darcy's Law

The conservation of momentum, which relates the sum of the forces acting on an element of fluid to its acceleration, can be described by Darcy's law in this work. As described previously, Darcy's law in 3D is:

$$\bar{q} = \frac{-\kappa}{\mu}(\nabla P - \rho g \hat{e}_z)$$

The permeability tensor κ and the viscosity of the fluid μ are assumed to be constant throughout the RTM process in this work; the cure is assumed to start after the infusion. Comparing this to a conventional momentum equation for the case of frictionless flow which is Euler's equation [54]:

$$\rho \frac{D\vec{V}}{Dt} = \rho \vec{g} - \nabla p \tag{2.10}$$

The order of Darcy's law is less than that of Euler's equation which means that the problem at hand is simpler to solve than problems involving the conventional momentum equation.

Another key relation derived from Darcy's law is the relation between the seepage velocity and actual fluid particle velocity. Referring back to Darcy's law as introduced in Equation (2.1), it is important to note that A represents the cross-section of pores and solid inclusions as well. By replacing γ with $\Delta P / L$ through the hydrostatic pressure relation, expressions for the seepage velocity are obtained:

$$\vec{q} = -\frac{\kappa}{\mu} \nabla P \tag{2.11}$$

The seepage velocity is defined as the ratio of the volumetric fluid flow rate through the porous medium, divided by the total cross section including the solid inclusions. The ratio between the seepage velocity and the actual velocity of fluid particles inside the column is expressed by the Dupuit-Forchheimer relation [55, 56]:

$$u_1 = \phi V_x \ ; \ u_2 = \phi V_y \ ; \ u_3 = \phi V_z \tag{2.12}$$

Since the section which is actually open to the fluid flow is smaller within the porous medium, the actual velocity of fluid particles is larger than the seepage velocity. Equations (2.11) and (2.12) constitute the foundation on which the solution to the pressure distribution is based, as well as the flow front progression part.

The energy equation, which is another key component to analytical fluid mechanics, is omitted in this work since the flow is assumed to be isothermal. During the infusion process, the temperature of the fluid stays essentially constant. The energy equation, which is based on the analysis of net heat flux in an element of fluid, can be left out.

2.5 Hagen-Poiseuille Relation: Edge Effects

The Hagen-Poiseuille relation is the other equation of importance in the formulation of the complete problem solved in this work, regarding the prediction of edge effects within the simulations. Edge effects occur during the filling process if the fabric is slightly smaller in size than the cavity itself. The expression refers to the fast progression of resin along the edges of the preform, through the gaps that can be present between the preform and mould walls. The term racetracking is also used in the literature. Leaving a gap of even 1 mm between the cavity wall and the fabric can create a preferential flow path for the resin which leads to a significant disruption of the filling process.

According to Hagen-Poiseuille [57] and Gebart [58], the following relation describes the volumetric flow rate of fluid between two parallel walls separated by a distance w:

$$Q = \frac{AW^2}{12\mu}\frac{\Delta P}{L} \tag{2.13}$$

Gebart [58] used this equation to replace the permeability K in Equation (2.1) by $W^2/12$; as such, an equivalent permeability for the channel flow can be described by this relation. For example, a 0.5 *mm* wide channel would result in a flow which is equivalent to a flow through a fabric with a permeability of 2.08×10^{-8} m^{-2}. A twice wider channel of 1.0 *mm* would nearly quadruple the permeability to 8.33×10^{-8} m^{-2}. The rest of the relation takes the exact same form as Darcy's law, thus modelling the edge effects becomes straightforward.

2.6 Pressure Distribution in the Saturated Domain

Using the continuity equation, Darcy's law and the Hagen-Poiseuille relation, solving for the pressure distribution in the saturated domain becomes possible. Considering a 2D case, the problem formulation is simple. From the continuity equation in 2D,

$$\frac{du_1}{dx} + \frac{du_2}{dy} = 0 \tag{2.14}$$

Substituting Darcy's law into Equation (2.14):

$$\frac{du_1}{dx}+\frac{du_2}{dy}=\frac{d}{dx}\left(-\frac{K}{\mu}\frac{\partial P}{\partial x}\right)+\frac{d}{dy}\left(-\frac{K}{\mu}\frac{\partial P}{\partial y}\right)=0 \tag{2.15}$$

Assuming that the viscosity μ and permeability K do not vary with x and y, as would be the case in RTM before resin cure, we have:

$$-\frac{K}{\mu}\left(\frac{d^2P}{dx^2}+\frac{d^2P}{dy^2}\right)=0 \tag{2.16}$$

Equation (2.16) is a form of partial differential equation and must be discretized in order to obtain the pressure distribution over the saturated domain.

2.7 Finite Differences Method (FD)

FD is a method of discretizing partial differential equations into a system of algebraic equations that can be solved for the appropriate variables at discrete grid points [53]. Taylor's series expansion is the most common finite differences representation of derivatives:

$$P_{i+1,j}=P_{i,j}+\left(\frac{\partial P}{\partial x}\right)_{i,j}\Delta x+\left(\frac{\partial^2 P}{\partial x^2}\right)_{i,j}\frac{(\Delta x)^2}{2}+\left(\frac{\partial^3 P}{\partial x^3}\right)_{i,j}\frac{(\Delta x)^3}{6}+\cdots \tag{2.17}$$

Equation (2.17) is an exact expression for $P_{i+1,j}$ if and only if the number of terms is infinite, the series converges and Δx approaches zero. Solving this equation in terms of $(\partial P / \partial x)_{i,j}$,

$$\left(\frac{\partial P}{\partial x}\right)_{i,j} = \frac{P_{i+1,j} - P_{i,j}}{\Delta x} - \left(\frac{\partial^2 P}{\partial x^2}\right)_{i,j} \frac{\Delta x}{2} - \left(\frac{\partial^3 P}{\partial x^3}\right)_{i,j} \frac{(\Delta x)^3}{6} + \cdots \tag{2.18}$$

a finite differences representation of the partial derivative $\left(P_{i+1,j} - P_{i,j}\right)/\Delta x$ can be obtained, which is the first term on the right hand side. The remainder of the right hand side is called the truncation error – part of the solution that is neglected during the approximation:

$$\left(\frac{\partial P}{\partial x}\right)_{i,j} = \frac{P_{i+1,j} - P_{i,j}}{\Delta x} \tag{2.19}$$

Since the lowest-order term in the truncation error involves Δx to the first power, Equation (2.19) is known to be accurate to the first-order. Furthermore, it uses the information to the right of grid point which is $P_{i+1,j}$, hence Equation (2.19) is called a first-order forward difference.

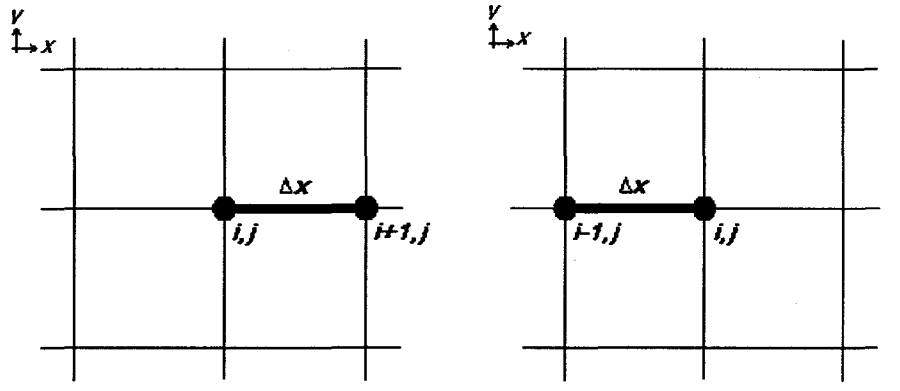

Figure 2-4 First-order forward and rearward differences with respect to x

Similarly, the Taylor series can be expanded for $P_{i-1,j}$ and lead to:

$$\left(\frac{\partial P}{\partial x}\right)_{i,j} = \frac{P_{i,j} - P_{i-1,j}}{\Delta x} + O(\Delta x) \tag{2.20}$$

This is known as the first-order rearward (or backward) difference.

Approximation accuracy can be improved by decreasing the truncation error. This can be done by including both sides of the finite differences quotient $P_{i+1,j}$ and $P_{i-1,j}$:

$$\left(\frac{\partial P}{\partial x}\right)_{i,j} = \frac{P_{i+1,j} - P_{i-1,j}}{2\Delta x} + O(\Delta x)^2 \tag{2.21}$$

This is known as the second-order central difference.

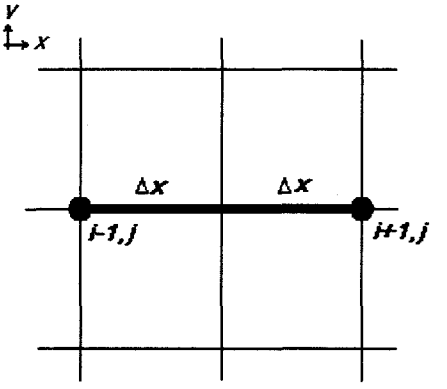

Figure 2-5 Second-order central difference with respect to x

Since the equations to be solved in determining the pressure distribution involve second order derivatives, there is a need for discretized equations that can handle derivatives beyond the first order. Discretizing a second-order derivative is done by manipulating the Taylor's series, this time solving for $\left(\partial^2 P / \partial x^2\right)_{i,j}$:

$$\left(\frac{\partial^2 P}{\partial x^2}\right)_{i,j} = \frac{P_{i+1,j} - 2P_{i,j} + P_{i-1,j}}{(\Delta x)^2} + O(\Delta x)^2 \tag{2.22}$$

This is called the second-order central second difference.

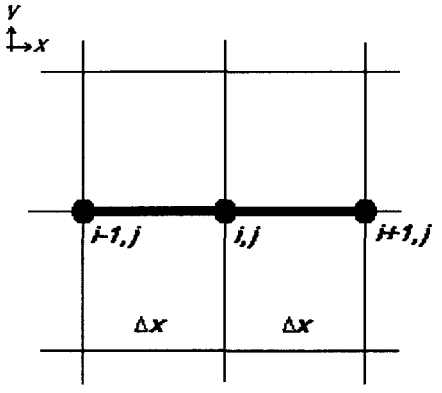

Figure 2-6 Second-order central second difference with respect to x

Similarly for $\left(\partial^2 P/\partial y^2\right)_{i,j}$:

$$\left(\frac{\partial^2 P}{\partial y^2}\right)_{i,j} = \frac{P_{i,j+1} - 2P_{i,j} + P_{i,j-1}}{(\Delta y)^2} + O(\Delta y)^2 \tag{2.23}$$

2.8 Boundary Conditions

Upon expanding the theory to 2D, the formulation of finite differences equations remains generally similar to the 1D case. However, implementing these equations for simulating resin flow in a mould raises questions pertaining to boundary conditions: how to express flow at boundaries parallel and/or perpendicular to wall, and how to apply second-order differences at boundary nodes. These issues can be illustrated using the following nine-node grid:

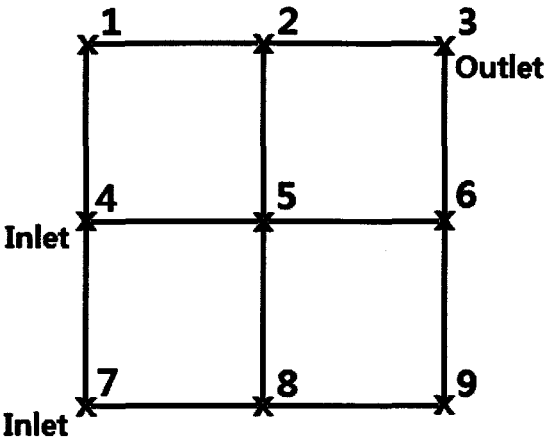

Figure 2-7 Nine-node FD grid

In this example, pressure at circled nodes 3, 4 and 7 is known whilst pressure at other nodes indicated by an x is unknown. There are 9 nodes in this simple case with 6 unknowns and 3 known pressures, thus 6 finite difference equations need to be formulated. Coefficients of the equations at each node vary depending on node position within the grid.

Recalling the case of a second order central second difference at node i on a 1D mesh, pressure had to be analyzed over three different nodes: i , $i-1$ and $i+1$. Similarly, a second order central second difference at node i, j in a 2D mesh requires the analysis of pressure at five different nodes; i , $i-1$, $i+1$, $i-m$ and $i+m$ as shown in Figure 2-8 where m denotes the number of columns in the grid, $i-m$ represents the node located one row above node i, and $i+m$ represents the node located one row below node i.

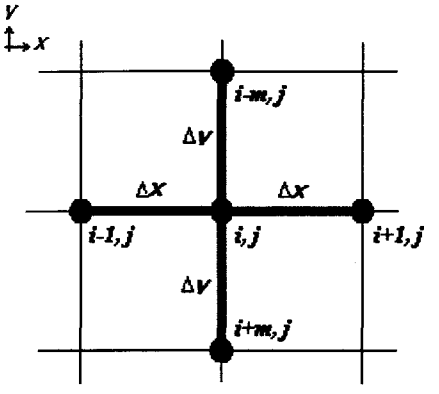

Figure 2-8 Second-order central difference in 2D

Coming back to Figure 2-7, consider node i=1 located at the top left boundary. Under the FD formulation, resin flow can only enter the node from one way and exit through the other – if the flow enters node 1 from node 4, it must exit node 1 towards node 2. Hence the conventional second order difference equations can not be used, since they require 5 nodes per equation but there are only 3 nodes available in this case: node 1, node 2 and node 4. Therefore, another expression for the second order difference at node i is needed. A method called the polynomial approach is used to develop said equation. Reverting to a 1D case for discussion, nodes 1, 2 and 3 from Figure 2-7 can be seen as the following.

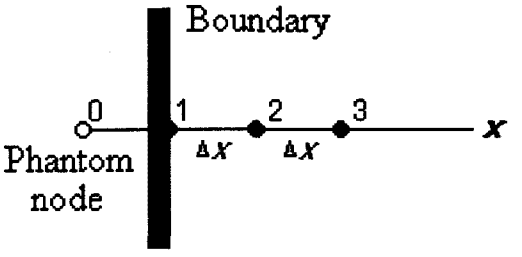

Figure 2-9 Grid points at a boundary, 1D case

Assuming that pressure P_1 at boundary node 1 shown in Figure 2-9 can be expressed by the following polynomial:

$$P_1 = a + bx + cx^2 \quad ; \quad \frac{dP_1}{dx} = b + 2cx \quad ; \quad \frac{d^2P_1}{dx^2} = 2c \tag{2.24}$$

in order to solve the constant c needs to be found. This can be done by applying the first part of the Equation (2.24) to the three nodes in Figure 2-9. At node 1 where $x = 0$,

$$P_1 = a \tag{2.25}$$

At node 2 where $x = \Delta x$,

$$P_2 = a + b\Delta x + c(\Delta x)^2 \tag{2.26}$$

At node 3 where $x = 2\Delta x$,

$$P_3 = a + b(2\Delta x) + c(2\Delta x)^2 \tag{2.27}$$

Since Equation (2.25) does not contain the constant c it is disregarded. Combining Equation (2.26) and (2.27) to solve for c:

$$c = \frac{P_1 - 2P_2 + P_3}{2(\Delta x)^2} \tag{2.28}$$

Thus the last part of Equation (2.24) yields:

$$\frac{\partial^2 P_x}{\partial x^2} = 2c = \frac{P_1 - 2P_2 + P_3}{(\Delta x)^2} \tag{2.29}$$

This is the same equation as the central difference equation that was introduced earlier – Equation (2.22) and (2.23). Thus the problem remains. To resolve this issue a simple manipulation of Equation (2.29) is made. When looking at node 1 in Figure 2-9, P_1 is used as the central node for the equation instead of P_2 and a phantom node 0 is added left of P_1. As for the phantom node left to the central node – left to node 1, which is over the boundary – it is specified with pressure P_1 again. Assigning the same pressure for these two nodes ensures a null pressure gradient between the node on the boundary and the phantom node, over the boundary as well as zero flow entering from the boundary, which is the correct boundary condition. Thus the second order difference is now expressed as:

$$\frac{\partial^2 P_x}{\partial x^2} = \frac{u_1 - 2P_1 + P_2}{(\Delta x)^2} = \frac{-P_1 + P_2}{(\Delta x)^2} \tag{2.30}$$

The equation now requires only 2 nodes. Going back to Figure 2-7 and expanding the problem in 2D, the conventional second order difference along x can be rewritten as:

$$\left(\frac{d^2 P}{dx^2}\right)_i = \frac{P_{i+1} - 2P_i + P_i}{\Delta x^2} = \frac{P_{i+1} - P_i}{\Delta x^2} = 0 \tag{2.31}$$

This is essentially equivalent to the first-order forward difference, assuming $\Delta x = \Delta y = 1$. Similarly for y:

$$\left(\frac{d^2 P}{dy^2}\right)_j = \frac{P_{j-1} - 2P_j + P_j}{\Delta y^2} = \frac{P_{j-1} - P_j}{\Delta y^2} = 0 \tag{2.32}$$

Thus, using Equation (2.31) and (2.32) successfully eliminates the unneeded components within the FD equations along the boundary nodes. Next section shows examples of use of these equations both in 1D and 2D.

2.9 Examples: 1D and 2D cases

For the 1D case, Equation (2.16) is the fundamental equation to be solved. This can be discretized using Equation (2.22):

$$\left(\frac{d^2P}{dx^2}\right)_i = \frac{P_{i+1} - 2P_i + P_{i-1}}{\Delta x^2} = 0 \tag{2.33}$$

Pressure at each node can be obtained by solving at every non-boundary node. Then velocities at the nodes can be obtained from Equation (2.11) as shown in the following five-node example.

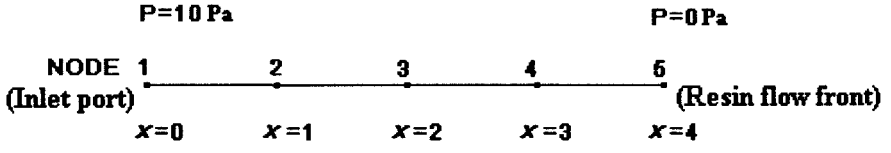

Figure 2-10 Five-node 1D example

Pressure is imposed at the inlet and outlet and there are three unknown pressures P_2, P_3 and P_4 – there must always be an inlet pressure and an outlet pressure in order to solve. Assuming an equal value for the distance between all nodes, linear algebraic equations at each node can be obtained from Equation (2.33):

$$\begin{aligned} P_3 - 2P_2 + 10 &= 0 \\ P_4 - 2P_3 + P_2 &= 0 \\ 0 - 2P_4 + P_3 &= 0 \end{aligned} \tag{2.34}$$

In matrix form this is expressed as:

$$\begin{bmatrix} -2 & 1 & 0 \\ 1 & -2 & 1 \\ 0 & 1 & -2 \end{bmatrix} \begin{bmatrix} P_2 \\ P_3 \\ P_4 \end{bmatrix} = \begin{bmatrix} -10 \\ 0 \\ 0 \end{bmatrix} \tag{2.35}$$

The above system can be solved directly using various numerical algorithms leading to $P_2 = 7.5\ Pa, P_3 = 5\ Pa$ and $P_4 = 2.5\ Pa$.

Moving on to a 2D example more closely related with the filling of an RTM mould, the system of equations to solve is expressed as:

$$\frac{\partial^2 P}{\partial x^2} + \frac{\partial^2 P}{\partial y^2} = 0 \tag{2.36}$$

In the discrete form there is one variable and one equation per node, thus the solution is obtainable. Reintroducing the nine-node FD grid with known boundary pressure values:

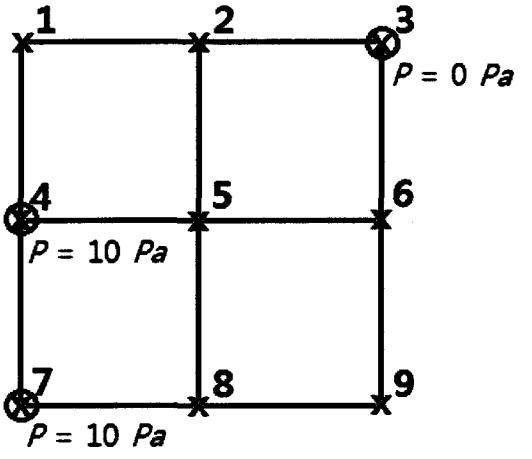

Figure 2-11 Nine-node FD grid with imposed pressures

By substituting the appropriate numbers for i and j in Equations (2.31) and (2.32) for node 1, the second order differences along x and y can be combined into:

$$\frac{\partial^2 P}{\partial x^2}+\frac{\partial^2 P}{\partial y^2}=P_4-2P_1+P_2=0 \tag{2.37}$$

The known pressures at P_3, P_4 and P_7 become part of the solution of the linear equations and get stored in the right-hand-side matrix. The set of linear equations in matrix form then looks like:

$$\begin{bmatrix} -2 & 1 & 0 & 0 & 0 & 0 \\ 1 & -3 & 1 & 0 & 0 & 0 \\ 0 & 1 & -4 & 1 & 1 & 0 \\ 0 & 0 & 1 & -3 & 0 & 1 \\ 0 & 0 & 1 & 0 & -3 & 1 \\ 0 & 0 & 0 & 1 & 1 & -2 \end{bmatrix} \cdot \begin{bmatrix} P_1 \\ P_2 \\ P_5 \\ P_6 \\ P_8 \\ P_9 \end{bmatrix} = \begin{bmatrix} -10 \\ 0 \\ -10 \\ 0 \\ -10 \\ 0 \end{bmatrix} \tag{2.38}$$

Various algorithms can be used to solve such systems of linear equations. The results are in this case:

$$\begin{bmatrix} P_1 \\ P_2 \\ P_5 \\ P_6 \\ P_8 \\ P_9 \end{bmatrix} = \begin{bmatrix} 7.308 \\ 4.615 \\ 6.538 \\ 4.103 \\ 7.436 \\ 5.769 \end{bmatrix} \tag{2.39}$$

The results can be analyzed more easily through the following figure:

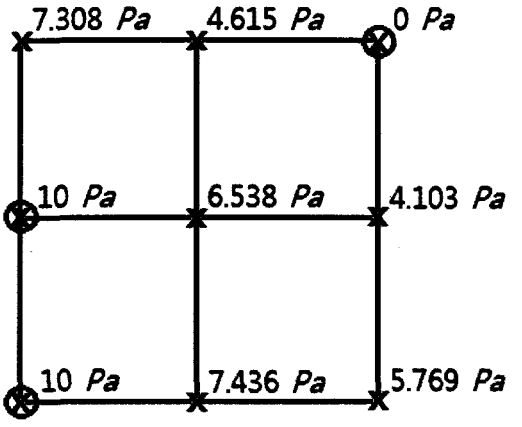

Figure 2-12 Pressure distribution of 2D example (*Pa*)

The results are validated by calculating the total volume of resin flowing in and out of each node, and checking agreement with Darcy's law. Referring to Figure 2-11, the central node 5 is subjected to fluid flow incoming from nodes 4 and 8 where the pressure is 10 Pa and 7.436 Pa, respectively. Assigning the unit value to variables K, μ and ϕ in Darcy's law, the total in-flow velocity is 4.360 *m/s* which is simply the sum of pressure gradients between nodes 4 – 5 and nodes 8 – 5. The total out-flow velocities can be calculated in similar matter by summing the pressure gradients between nodes 5 – 2 and nodes 6 – 5, which gives 4.358 *m/s*. Discrepancy results from rounding error. The validation is satisfied for all nodes within this mesh.

2.10 Flow Front Progression

As demonstrated in the previous section, the pressure distribution can be solved over the saturated domain as long as the inlet and outlet pressures are known. The

pressure distribution obtained also can lead to the calculation of velocities between nodes by solving the seepage velocity equation, Equation (2.11). Rewriting in 1D to be more specific:

$$u_x = -\frac{K_x}{\mu\phi}\frac{(P_i - P_o)}{\Delta x} \tag{2.40}$$

The velocity obtained from this relation is used as the basis for moving the flow front towards the unsaturated domain. With the introduction of time, this calculation is done at every time step to progress the flow front. As shown in the following flow chart:

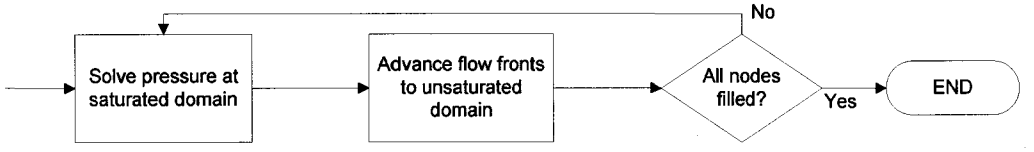

Figure 2-13 Flow front progression algorithm

The central box in Figure 2-13 involves that the continuous line corresponding to the advancing flow front in 2D will be located between nodes. As a consequence, the last nodes saturated by resin will be at a pressure higher than 0 *Pa*. The remainder of this section details the positioning process for the flow front.

At every instant, the outlet pressure values for solving the finite differences are the pressure values of the nodes which are recognized as the 'last saturated' nodes. These values are updated at every time step by iterating Darcy's law until the flow front reaches

the next unsaturated node. The distance by which the flow front progresses is determined by the flow front velocity. The following figure illustrates the flow front progression algorithm.

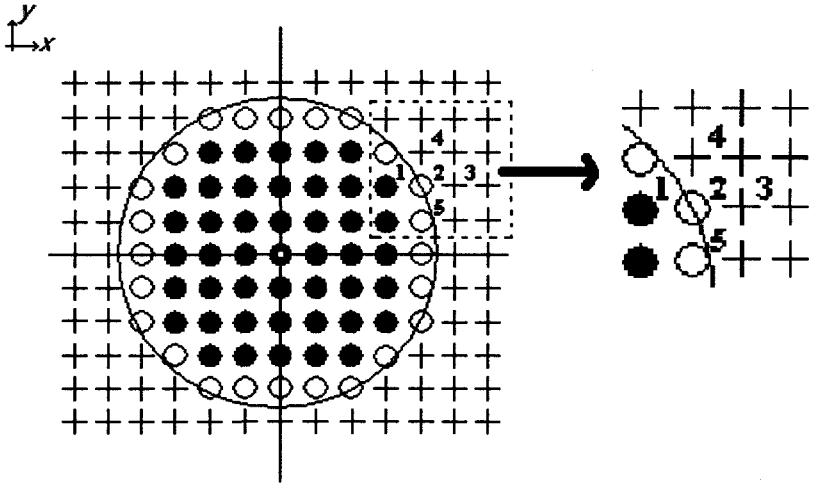

Figure 2-14 Example of radial flow front progression

The saturated nodes are denoted by solid circles in the Figure 2-14, while unsaturated nodes are denoted by crosses. The last saturated nodes are denoted by hollow circles, meaning that the flow always moves from a hollow circle to a plus sign. The pressures at the last saturated nodes must be known in order to determine the pressures at other nodes in the domain – other than the inlet. Assuming that the flow has just reached node 2 in Figure 2-14, if the nodes are separated by the distance of 1, Δx and Δy at node 2 need to increase and eventually become 1 in order for the nodes 3 and 4 to be saturated, and for the flow front to progress further. Considering the flow in the x-direction first, the following equation can be obtained from Darcy's law which gives the real velocity of the flow front along x:

$$v_x = \frac{K_x}{\mu\phi}\frac{(P_1 - P_2)}{\Delta x} \tag{2.41}$$

Thus the flow front is progressed along x as stated in the following relation:

$$\Delta x = v_x t \tag{2.42}$$

The saturated distance between two nodes – Δx is then used to recalculate the last saturated node's pressure, through the relation:

$$P_2 = \frac{v_x \Delta x \mu\phi}{K_x} \tag{2.43}$$

which is essentially reordering Equation (2.41) and solving for the last saturated node's pressure P_2. It is assumed that the distribution of pressure is linear from node $i-1$ to the flow front. If Δt is sufficiently small, the error resulting form this assumption becomes negligible.

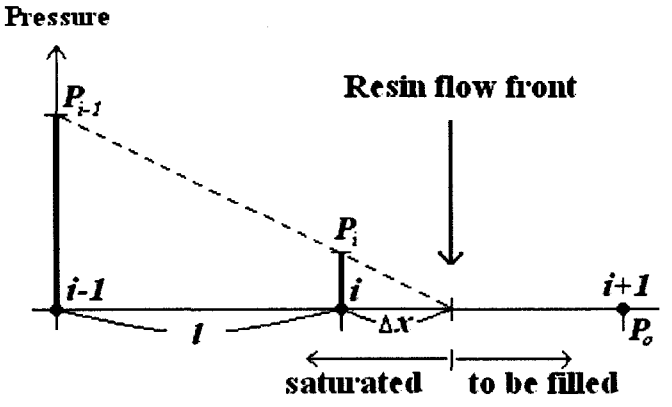

Figure 2-15 Algorithm for solving the last saturated node

The distance between the nodes is represented by l. The pressure at the last saturated node, P_i, can be recalculated at each time step since the pressure at previously filled node P_{i-1} and the outlet pressure P_o are always known. Once the front is progressed, the pressure at each saturated node is recalculated using the updated parameters.

2.11 RTM Simulation Validation in 1D and 2D

Results from the filling simulation software were validated against analytical results. In the 1D case, Darcy's law is solved in terms of the time variable t to obtain:

$$t = \frac{x^2 \phi \mu}{2KP_i} \tag{2.44}$$

This equation was evaluated at every node and compared to simulation results. A 1D simulation was done using a 10-node grid laid on a straight line. The parameters used in the simulation and analytical solutions were:

$$K = 2.13\times10^{-8}\ m^2$$

$$P_i = 101\ KPa$$

$$P_o = 0\ KPa$$

$$\phi = 0.71$$

$$\mu = 0.048\ Pa\cdot s$$

Permeability K was calculated from the Kozeny-Carman equation [42]. The value chosen for the Kozeny constant was $5\times10^{-11}\ m^2$ which is based on the work of Correia *et al* [42]. The node spacing was set at 0.02 m while the time step used was 0.1 seconds. The results showed slight improvements in terms of convergence towards the theory when a smaller time step was used. The results could be further improved by using a denser mesh. Another set of validation trials were done with reduced node spacing of 0.01 m.

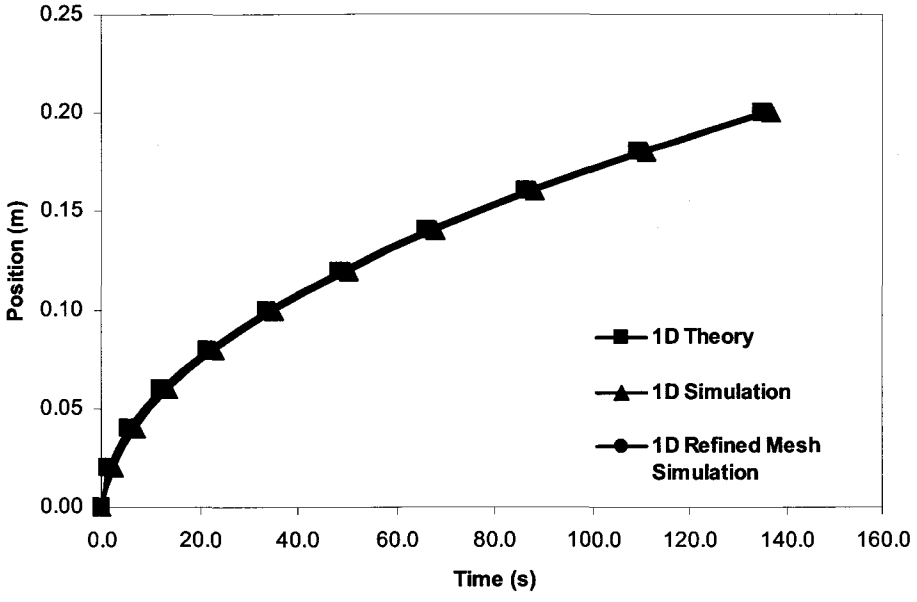

Figure 2-16 Analytical solution vs. simulation results in 1D

Table 2-1 Analytical solution vs. simulation results in 1D

Position (*m*)	Theoretical fill time (*s*)	Simulation fill time (*s*)	Error (%)
0.00	0.0	0.00	0.00
0.02	1.35	2.70	100.04
0.04	5.40	6.80	25.95
0.06	12.15	13.60	11.96
0.08	21.60	23.10	6.97
0.10	33.74	35.30	4.62
0.12	48.59	50.20	3.31
0.14	66.14	67.80	2.52
0.16	86.38	88.10	1.99
0.18	109.33	111.10	1.62
0.20	134.97	136.80	1.36

Table 2-2 Improved 1D simulation results using refined mesh

Position (*m*)	Theoretical fill time (*s*)	Refined simulation fill time (*s*)	Error (%)
0.00	0.0	0.00	0.00
0.02	1.35	1.70	25.95
0.04	5.40	5.80	7.43
0.06	12.15	12.70	4.55
0.08	21.60	22.20	2.80
0.10	33.74	34.50	2.24
0.12	48.59	49.40	1.67
0.14	66.14	67.00	1.31
0.16	86.38	87.40	1.18
0.18	109.33	110.50	1.07
0.20	134.97	136.20	0.91

As shown in Figure 2-16, both simulations resulted in accurate results although the simulation based on a denser mesh was more accurate. The downside to the refined mesh simulation was that it required far more computational power, which led to more run time. An ideal approach would be to refine the nodes around the inlet only, which would lead to the reduction of large error during the beginning phase of fill time. However, this capability is not yet developed within this software.

For the 2D case, the equations describing the filling of a planar cavity developed by Adams, Miller and Rebenfeld [12] are introduced:

$$\frac{dR_f}{dt} = \frac{K\Delta P}{\mu\phi R_f \ln\left(R_f / R_0\right)} \tag{2.45}$$

where R_f denotes the radius of the flow front and R_o denotes the radius of the inlet boundary, which was set at 6 mm. By integrating and solving for the fill time t, the equation becomes:

$$t = \frac{\mu\phi}{KP_i}\left[\frac{R_f^{\,2}}{2}\ln\left(\frac{R_f}{R_0}\right) - \frac{R_f^{\,2}}{4}\right] \tag{2.46}$$

Much as in 1D, this equation was solved at various locations of the radius starting from 0 m to 0.20 m and the results were compared with the measured times obtained from the simulation at the same locations. The simulation was done using a rectangular grid with a size of 21 by 23 nodes with spacing of 0.02 m. Another test was done using a refined mesh with the grid spacing of 0.01 m for comparison purposes. Other parameters, including the time step, were identical from those used in the test in 1D. The results are:

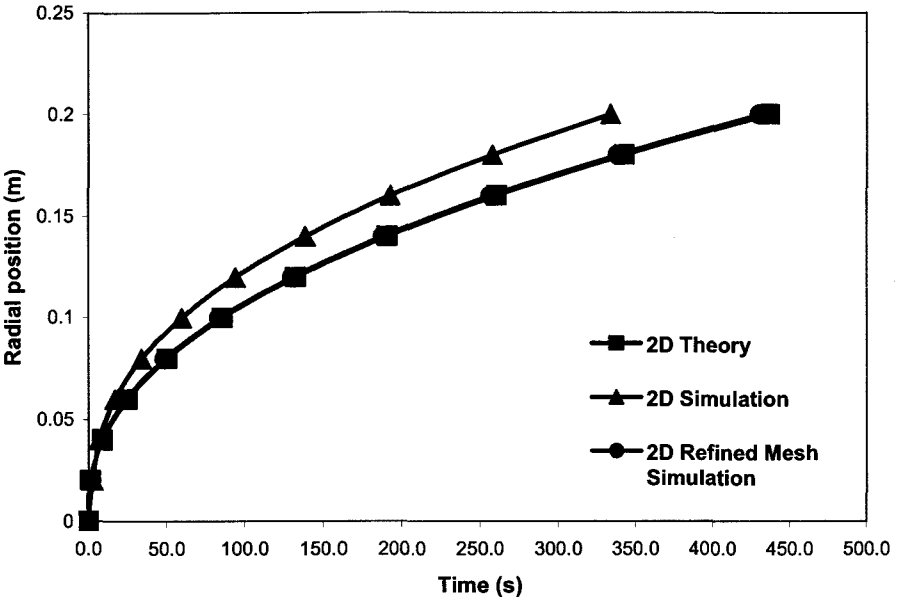

Figure 2-17 Analytical solution vs. simulation results in 2D

Table 2-3 Analytical solution vs. simulation results in 2D

Position (*m*)	Theoretical fill time (*s*)	Simulation fill time (*s*)	Error (%)
0.00	0.00	0.00	0.00
0.02	1.26	2.70	113.96
0.04	8.79	6.80	22.64
0.06	24.70	16.80	31.99
0.08	50.13	33.70	32.77
0.10	85.85	59.60	30.58
0.12	132.49	94.00	29.05
0.14	190.53	138.50	27.31
0.16	260.39	192.30	26.15
0.18	342.43	257.50	24.80
0.20	436.97	333.60	23.66

Table 2-4 Improved 2D simulation results using refined mesh

Position (*m*)	Theoretical fill time (*s*)	Refined simulation fill time (*s*)	Error (%)
0.00	0.00	0.00	0.00
0.02	1.26	1.70	34.72
0.04	8.79	8.60	2.16
0.06	24.70	23.80	3.65
0.08	50.13	48.70	2.85
0.10	85.85	83.90	2.28
0.12	132.49	130.20	1.73
0.14	190.53	187.80	1.43
0.16	260.39	256.80	1.38
0.18	342.43	338.20	1.23
0.20	436.97	430.20	1.55

Simulation fill time for the coarse mesh showed relatively large discrepancies with the theoretical results; however the refined mesh showed accurate results with an error range of 3% or less. Similarly to the 1D test, the refined test required much more memory to process. The computational time to flow the resin up to 0.20 *m* was near 20 minutes as opposed to about a minute for coarse mesh test. As mentioned, the large error near the inlet could be greatly reduced if the software was capable of doing refined meshing at selected regions – near the inlet in this case.

The last validation to be done was for cases of reinforcements with different permeability values along two different directions. An example would be a unidirectional fabric, which is a fabric with majority of its fibres running in one direction only. A small amount of fibre may run in other directions with the main purpose of holding the primary fibres in position. A simulation was run using properties which represent these types of

fabrics, with permeability values along x and y of $5.00\times10^{-11}\,m^{-2}$ and $3.00\times10^{-11}\,m^{-2}$, respectively. The radial flow distance along x and y were measured at ten different locations. The results were then compared with theoretical values obtained from the relation derived by Chan, Larive and Morgan [59] describing filling of a cavity enclosing an orthotropic fabric. The relation describes the ratio of flow distances between two orthogonal axes x and y:

$$y=\left(\frac{K_y}{K_x}\right)^{1/2} x \tag{2.47}$$

The relation was evaluated for y using the permeability values stated above. The results were:

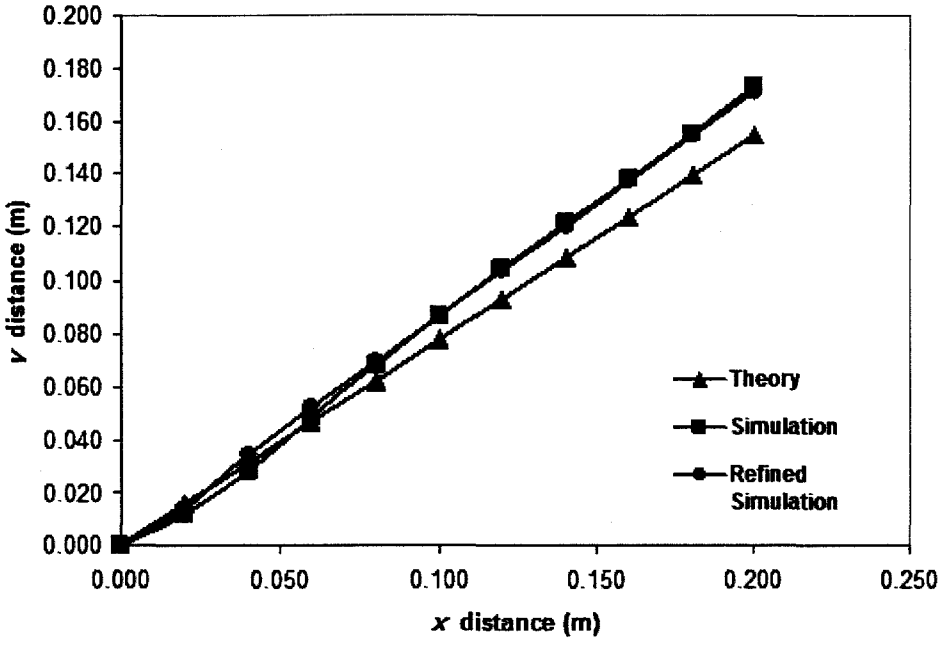

Figure 2-18 Radial distance comparison of two axes in ellipse

The first three points in Figure 2-18 show very similar results from theory and simulation; however the results show some discrepancies starting from the 4th point. The error fluctuates within the range of 10%, which is acceptable in practice since no flow would ever behave exactly like what the theory describes. Another test was done using a refined mesh, anticipating improved results much like the other validations. A definite improvement was made near the inlet region; however the remaining region did not show significant improvement. Nevertheless, the results of these trials were regarded as satisfactory for practical applications, with errors generally around 10%.

Table 2-5 Radial distance comparison of two axes in elliptical flow front

Radial position in x (m)	Theoretical radial position in y (m)	Simulation radial position in y (s)	Error (%)
0.000	0.000	0.000	0.000
0.020	0.015	0.012	22.540
0.040	0.031	0.028	8.080
0.060	0.046	0.048	3.820
0.080	0.062	0.068	10.010
0.100	0.077	0.087	11.930
0.120	0.093	0.104	12.390
0.140	0.108	0.121	12.000
0.160	0.124	0.138	11.590
0.180	0.139	0.156	11.530
0.200	0.155	0.173	11.610

Table 2-6 Improved radial distance comparison of two axes in elliptical flow front with refined mesh

Radial position in x (m)	Theoretical radial position in y (m)	Simulation radial position in y (s)	Error (%)
0.000	0.000	0.000	0.000
0.020	0.015	0.014	10.790
0.040	0.031	0.034	9.900
0.060	0.046	0.052	12.360
0.080	0.062	0.069	11.650
0.100	0.077	0.086	11.540
0.120	0.093	0.104	11.450
0.140	0.108	0.121	11.150
0.160	0.124	0.138	11.110
0.180	0.139	0.155	11.030
0.200	0.155	0.171	10.380

2.12 VARTM Analysis in 1D

VARTM differs from RTM in many ways. First, the tooling is significantly different as VARTM only requires a single lower mould along with an upper film, whereas RTM requires both upper and lower moulds to produce the composite part. VARTM therefore yields much lower tooling costs especially when producing large parts. Secondly, VARTM uses vacuum to draw the resin into the mould whereas in RTM, resin is usually injected using positive pressure, enabling stronger pressure gradients. Lastly, the vacuum inside the VARTM mould creates a variation in the distribution of atmospheric pressure between the resin and preform. As the local resin pressure changes during the flow, the local compaction pressure on the preform changes as well. This ultimately leads to a change in thickness of the part being infused. The pressure applied onto the preform is also known as the compaction pressure. The consequence of changes in compaction pressure is changes in thickness, porosity and permeability of the part being infused, as the resin flow front advances.

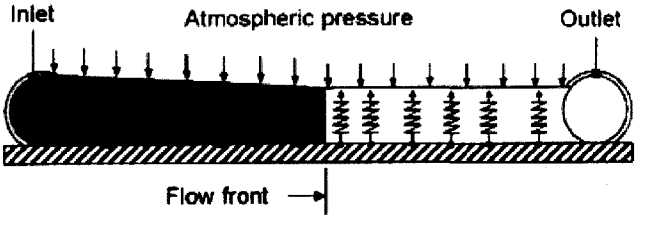

Figure 2-19 Effect of fluid pressure on compaction [42]

According to Hammami [60], VARTM can be discretized quantitatively using the same governing equations for flow as in RTM, i.e., Darcy's law. However, a few assumptions

need to be made to account for the flexible nature of the upper film. One is to introduce an equation for the transverse equilibrium of forces:

$$P_c + P_r = P_0 \tag{2.48}$$

The expression states that the sum of the compaction pressure and the resin pressure are equal to the atmospheric pressure. Since the compaction pressure varies along the distance between the inlet and outlet, the thickness of the preform also varies. This is known as the compaction function:

$$h = f(P_c) \tag{2.49}$$

Similarly, a function relating the permeability of the preform to the thickness of preform is needed. Since the problem at hand is 1D, only isotropic permeability needs to be considered:

$$K = g(h) \tag{2.50}$$

This function is known as the permeability function. As for the continuity, the analysis of 1D in-plane flow in a compacting porous medium by Gutowski *et al.* [61] can be followed:

$$\frac{\partial h}{\partial t} = -\frac{\partial (uh)}{\partial x} \tag{2.51}$$

This expression clearly differs from equation (2.14) which is the continuity expression for flow in an incompressible medium, i.e. in RTM. Combining equation (2.51) with Darcy's law in 1D:

$$\frac{\partial h}{\partial t} = \frac{1}{\mu}\left[hK\frac{\partial^2 P_r}{\partial x^2} + K\frac{\partial P_r}{\partial x}\frac{\partial h}{\partial x}\right] \tag{2.52}$$

Equation (2.52) features quantities h and K which are functions of v_f. According to Robitaille and Gauvin [62], the compaction pressure P_c is related to the fibre volume fraction by:

$$v_f = AP_c^B \tag{2.53}$$

Coefficient A represents the fibre volume fraction for a compaction pressure P_c equal to 1 Pa and B represents the compaction stiffening index. These coefficients are obtained through experiments and are tabulated in [62]. The preform thickness h is related to the fibre volume fraction by:

$$h = \frac{h_{layer} n}{v_f} \tag{2.54}$$

The thickness of single fabric layers is represented by h_{layer} and the number of layers is represented by n. Moreover, an expression of K as a function of v_f can be obtained from the permeability database by Parnas, Flynn and Dal-Favero [18]. The database provides the permeability of various preform materials over a wide range of fibre volume fractions.

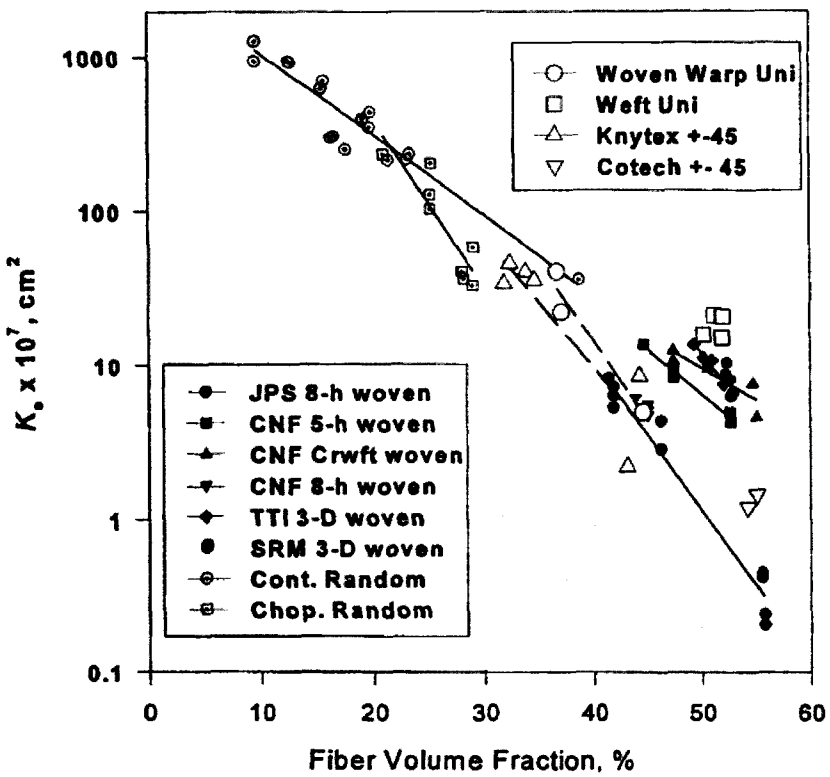

Figure 2-20 In-plane saturated flow measurements of various materials [18]

As seen in Figure 2-20, the trend line for the data points can be approximated as a straight line on the semi-logarithmic graph. Thus, using an algebraic relation for the slope of a line, the required permeability parameter as a function of v_f can be obtained by:

$$\log(K) = mv_f + b \tag{2.55}$$

Selecting any two data points on the curve allows calculating the slope m and the y-intercept b. Once h and K are related in terms of v_f, the calculation of P_r can be done using an explicit approach of iterative method. The iteration algorithm is shown below:

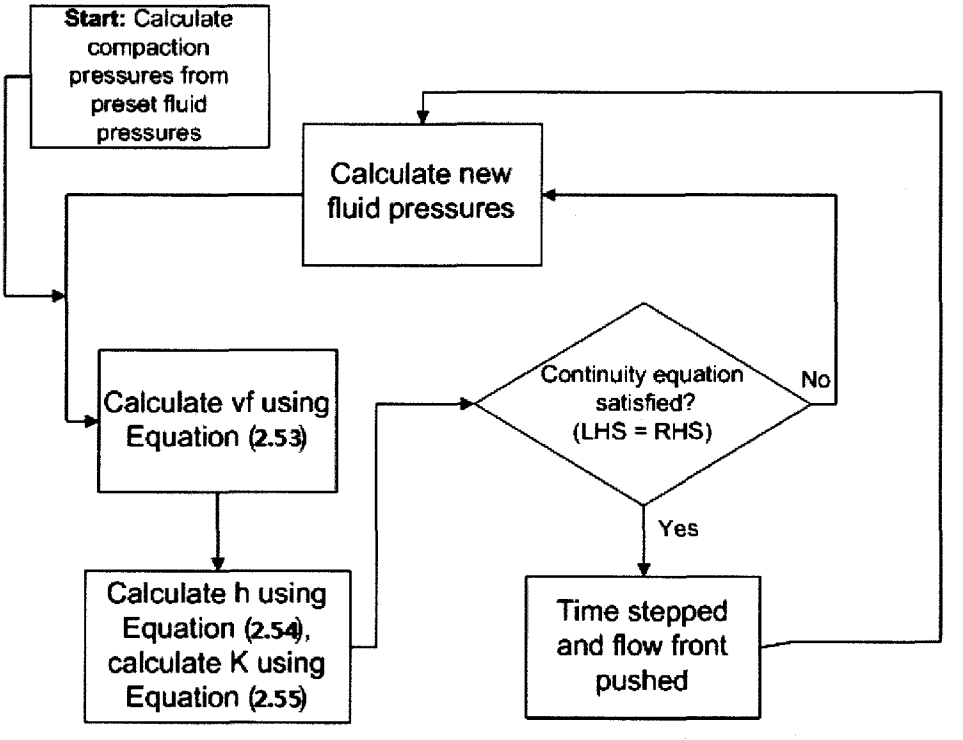

Figure 2-21 Iterative algorithm

It is important to remark that Equations (2.53) and (2.55) are approximations developed from the models of Robitaile *et al.* and data of Parnas *et al.*, respectively, which themselves are simplifications.

One important issue arises in the analysis of VARTM: the finite differences formulation for VARTM differs from that of RTM due to the fact that permeability and porosity do not remain constant. As described through Equations (2.14) to (2.16), the 2nd order partial difference equation which is solved by the 1D RTM simulation software is simply:

$$-\frac{K}{\mu\phi}\frac{\partial^2 P}{\partial x^2}=0$$

In this expression, pressure is the only variable that changes with respect to position. However for VARTM, permeability and porosity need to be taken into the partial difference equation since they also change with respect to position.

$$\frac{\partial}{\partial x}\left(-\frac{K}{\mu\phi}\frac{\partial P}{\partial x}\right)=0 \tag{2.56}$$

Applying Equation (2.56) over three nodes of $i-1$, i and $i+1$, the equations can be discretized to:

$$\left(-\frac{K_i}{\phi_i}\right)P_{i-1}+\left(\frac{K_i}{\phi_{i+1}}+\frac{K_{i+1}}{\phi_i}\right)P_i+\left(\frac{K_i}{\phi_i}-\frac{K_i}{\phi_{i+1}}-\frac{K_{i+1}}{\phi_i}\right)P_{i+1}=0 \tag{2.57}$$

Equation (2.57) can be applied at all nodes within the 1D grid to formulate the necessary finite differences equations. These equations are solved explicitly – using iterative approach – in VARTM simulations, whereas they were solved implicitly – using matrix inversion – in RTM simulations. The explicit approach is easier to program than the implicit approach and it also requires less computer processing, however the solution obtained from the explicit approach is less stable than the implicit approach; convergence is less certain. The implicit approach deals with massive matrix manipulations at each time step which leads to the requirement of more computer processing power. However, this method leads to a more stable solution despite the disadvantages. The reason for choosing the explicit approach in this segment of work was to obtain an accurate result without devoting the majority of effort to programming. To illustrate the explicit iterative method in details, an example with three different linear algebraic equations is introduced as follows:

$$x+2y+3z=1$$

$$2x-y+z=4$$

$$x+y-4z=5$$

An arbitrary initial solution is set at $(x,y,z)=(1,1,1)$, which is far off from the actual solution. This can be checked as follows:

$$(1)+2(1)+3(1)=6$$

$$2(1)-(1)+(1)=2$$

$$(1)+(1)-4(1)=-2$$

The objective is to arrive at the right hand side of $(1,4,5)$, but the arbitrary input results in $RHS=(6,2,-2)$. In order to converge towards the solutions, *x, y,* and *z* need to be altered so that the *RHS* moves to the correct terms by:

$$\overrightarrow{MR}=(1-6,4-2,5+2)=(-5,2,7)$$

Similarly, the effect of each term *x, y,* and *z* on the solution can be described as vectors:

$$\overrightarrow{MX}=(1,2,1)$$

$$\overrightarrow{MY}=(2,-1,1)$$

$$\overrightarrow{MZ}=(3,1,-4)$$

The goal is to balance changes along *x, y* and *z* into a displacement vector that will reduce the difference between correct right terms, and right terms that are obtained at the given position. Note that the more parallel $\overrightarrow{MX}$, $\overrightarrow{MY}$ or $\overrightarrow{MZ}$ are to $\overrightarrow{MR}$, the more each coordinate will be used in the changes. Parallelism of vectors is determined using the dot product. The three coordinates *x, y,* and *z* need to change in proportion to the level of

parallelism of $\overrightarrow{MX}$, $\overrightarrow{MY}$ and $\overrightarrow{MZ}$ to $\overrightarrow{MR}$. Also, the ratios of amplitudes of $\overrightarrow{MX}$ to $\overrightarrow{MR}$, $\overrightarrow{MY}$ to $\overrightarrow{MR}$ and $\overrightarrow{MZ}$ to $\overrightarrow{MR}$ need to be considered when building the 'change *xyz*' vector, because that change needs to be inversely proportional to its effect. Continuing with the example, the unit vectors $u\overrightarrow{MX}$, $u\overrightarrow{MY}$, $u\overrightarrow{MZ}$ and $u\overrightarrow{MR}$ can be calculated as:

$$u\overrightarrow{MR} = (-0.5661, 0.2265, 0.7926)$$

$$u\overrightarrow{MX} = (0.4082, 0.8165, 0.4082)$$

$$u\overrightarrow{MY} = (0.8165, -0.4082, 0.4082)$$

$$u\overrightarrow{MZ} = (0.5883, 0.1961, -0.7845)$$

The dot products of these unit vectors are:

$$u\overrightarrow{MR} \cdot u\overrightarrow{MX} = 0.2774$$

$$u\overrightarrow{MR} \cdot u\overrightarrow{MY} = -0.2311$$

$$u\overrightarrow{MR} \cdot u\overrightarrow{MZ} = -0.9104$$

The numbers indicate that the ideal change should be along the direction of positive *x*, and the direction of negative *y* and *z*. As far as the amplitude is concerned, a comparison can be made for the amplitude of the change in right terms resulting from the change $(0.2774, -0.2311, -0.9104)$ to the change in right terms that is ideal, and apply a factor

between 0 and 1 to that value. Solving the three equations with $(0.2774, -0.2311, -0.9104)$ results in the following values:

$$1(0.2774)+2(-0.2311)+3(-0.9104)=-2.9162$$

$$2(0.2774)-1(-0.2311)+1(-0.9104)=-0.1246$$

$$1(0.2774)+1(-0.2311)-4(-0.9104)=3.6879$$

The three right hand terms above are the components of the 'change *xyz*' vector. The amplitude of this change is:

$$AMP=\left[(-2.9162)^2+(-0.1246)^2+(3.6879)^2\right]^{1/2}=4.0733$$

The amplitude of the ideal change is:

$$IAMP=\left[(1-6)^2+(4-2)^2+(5+2)^2\right]^{1/2}=8.8318$$

To be cautious, the 'change *xyz*' vector can be factored so that the amplitude of the change in right terms is 50% – a factor that is adjustable – of the amplitude of the change needed. Therefore the final change in *x*, *y* and *z* that will be made from one iteration is:

$$\Delta x = \left(u\overline{MR} \cdot u\overline{MX}\right) 0.5 \frac{IAMP}{AMP} = 0.2604$$

$$\Delta y = \left(u\overline{MR} \cdot u\overline{MY}\right) 0.5 \frac{IAMP}{AMP} = -0.2170$$

$$\Delta z = \left(u\overline{MR} \cdot u\overline{MZ}\right) 0.5 \frac{IAMP}{AMP} = -0.8548$$

The above changes are made to the initial solutions of x, y and z. Upon iterating, the values of x, y and z converge to a solution:

$$x = 2.4$$

$$y = 0.2$$

$$z = -0.6$$

This explicit iteration method is implemented upon development of finite difference equations obtained from equation (2.57).

To validate the iteration method, early tests were done using a Microsoft Excel Macro function. The test consisted of a 10-node 1D grid with initial pressures pre-assigned to each node. At this stage the solution was implmented for solving the pressure distribution at a given time. This early test did not feature flow front progression, which is discussed in Chapter 4. The material chosen for the test was Vetrotex U101 provided by Owens Corning which is a chopped random mat with a surface density of 450 g/m^2. According to Robitaille and Gauvin [62], 6 layers of this preform have compaction

coefficients A and B of 0.0209 and 0.219 respectively. In Figure 2-20, chopped random mats are presented by hollow squares with a dot, and the points were taken from the trend line for analysis. After much iteration, the initial assigned values converged towards the solution and produced the distribution shown in Figure 4-151:

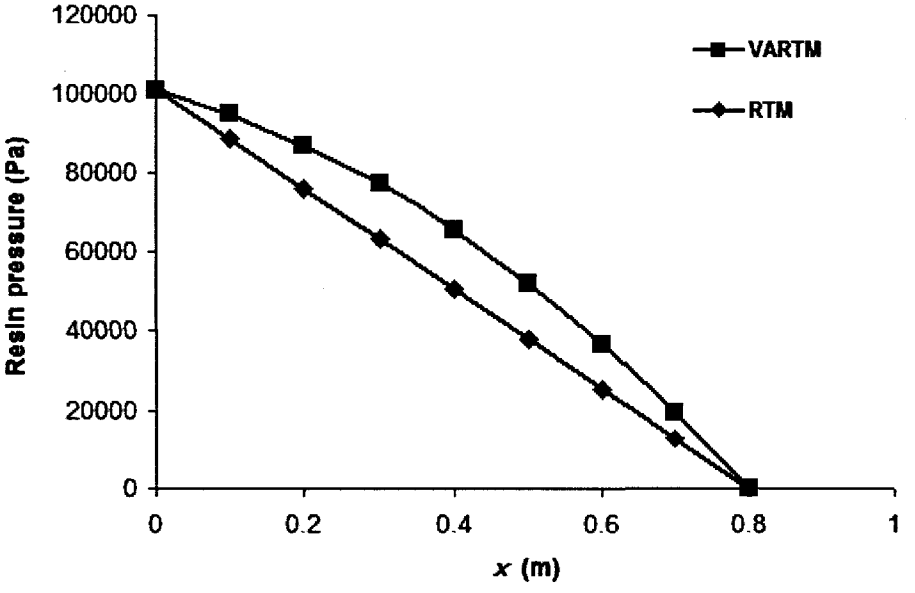

Figure 2-22 Resin pressure vs. Position (for VARTM and RTM)

Figure 2-22 shows the difference in VARTM and RTM resin pressure fields. In RTM, the pressure decreases linearly whereas in VARTM the pressure decreases non-linearly. This is due to the fact that the thickness, fibre volume fraction and permeability are no longer fixed parameters as they were in the case of RTM. The pressure gradient at $x = 0m$ is lower, indicating a preform that is less compacted and has a larger permeability. Conversely, a more compacted preform at $x = 0.8m$ leads to a lower permeability and a

larger pressure gradient. The fibre volume fraction is affected greatly by the compaction pressure. The fibre volume fraction is highest at the region where the compaction pressure is highest, close to the resin flow front where the resin pressure is lowest. Figure 2-22 compares very well with Figure 2-23 which shows similar results obtained by Correia *et al* [42].

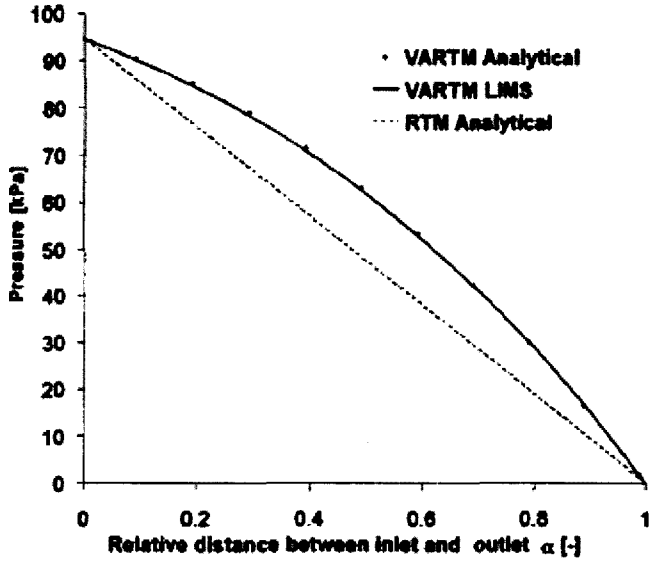

Figure 2-23 Pressure fields in 1D VARTM and RTM

Correia *et al.* validated their analytical pressure field for VARTM with the use of Liquid Injection Moulding Simulation (LIMS), which is proprietary software from University of Delaware.

3 Validation Setup and Procedures

3.1 Experimental Setup

To compare the simulated infusion process with actual infusions, seven different RTM experiments were conducted. RTM experiments were conducted on a flat rectangular mould measuring 850.0 *mm* in length and 600.8 *mm* in width, Figure 3-1. The actual cavity area was smaller at 784.0 *mm* by 530.0 *mm*. In a given test the preform was inserted in the cavity which had a depth of 3.18 *mm*, and then a cover made of polymethylmethacrylate (PMMA) with a thickness of 12.7 *mm* was placed on top, Figure 3-2 and Figure 3-3. Great care was taken in cutting layers of reinforcement that fitted the cavity dimensions as closely as possible. The mould cavity was created by the use of four aluminum bars which became the walls of the cavity. The cavity cover was bolted together with these bars, and then silicone sealant was applied to the gaps to ensure minimum air ingress. The reason for selecting a relatively thick cover was to reduce bending from the pressure difference between vacuum and atmospheric pressure on both sides of the cover.

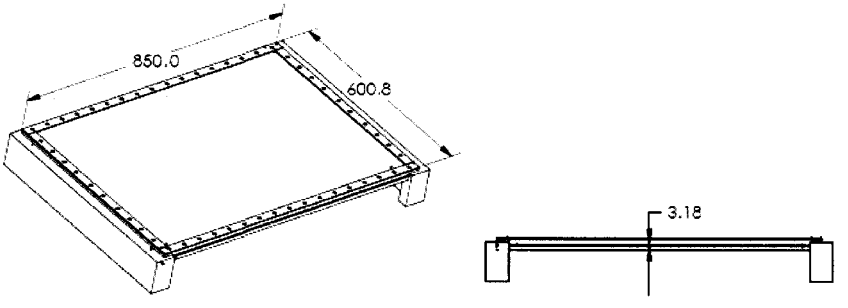

Figure 3-1 Mould dimension (*mm*)

Figure 3-2 Isometric and front view of the mould cavity

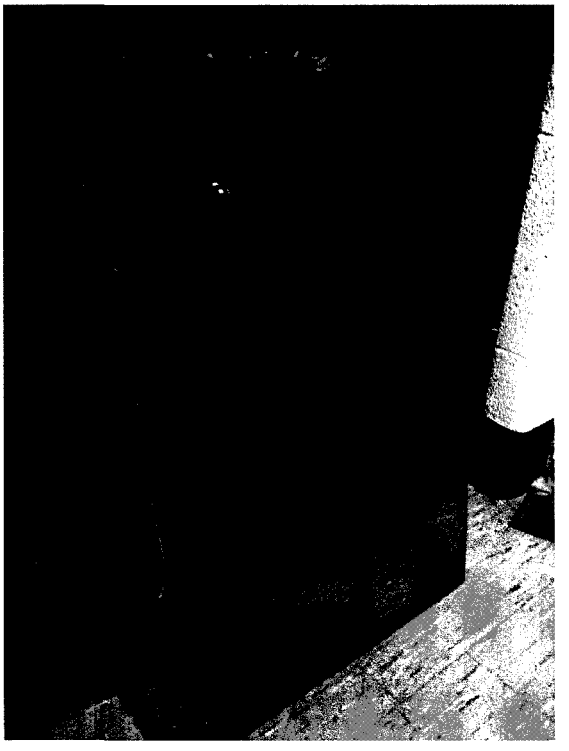

Figure 3-3 Polymethylmethacrylate mould cover

The mould also features 17, ¼" NPT filleted holes machined in the bottom plate as numbered in Figure 3-4. Any one of these can be used as an inlet hole for resin to enter or

as a vacuum port. The holes can also be used for connecting the high-accuracy pressure transducer Cole-Parmer Instrument, EW-68073-06 having an accuracy of ±0.13% full scale; the transducer keeps track of pressure, or vacuum level in the dry section of the cavity.

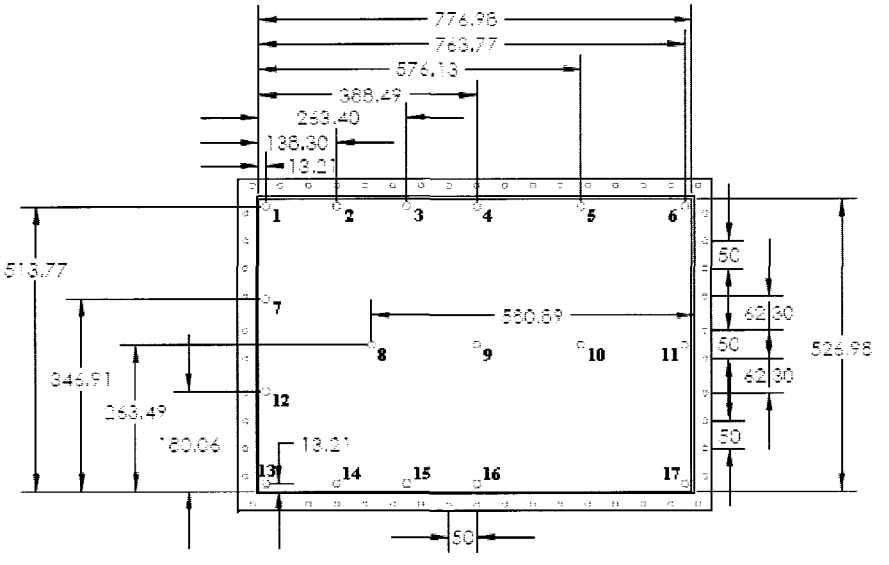

Figure 3-4 Bottom plate of the mould with 1/4" NPT holes (*mm*)

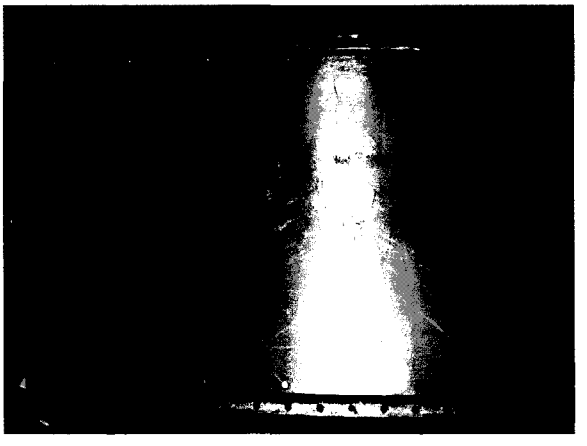

Figure 3-5 Top view of mould cavity

Two different types of reinforcements were used during the experiments. Reinforcement 1 is a U101-600 glass fibre random mat sourced from Owens Corning with a surface density of 0.600 kg/m^2. The number of layers used for the experiments are either two or four depending on the case; these are specified further in the text.

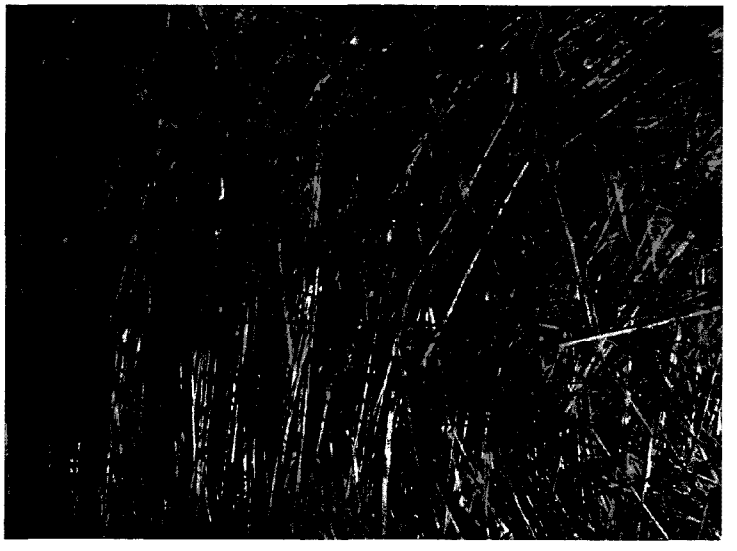

Figure 3-6 Reinforcement 1: U101-600 E-glass random fabric from Owens Corning

Figure 3-7 Magnified view of Reinforcement 1

Reinforcement 2 is TG18U50 woven glass fibre unidirectional mat sourced from JB Martin. In order to gain stability, fibres running perpendicular to the main load bearing yarns are added at every centimetre across the main yarns. There are about 5 main yarns per centimetre. This particular unidirectional fabric has a surface density of 0.603 kg/m^2, which is close to the value obtained for Reinforcement 1.

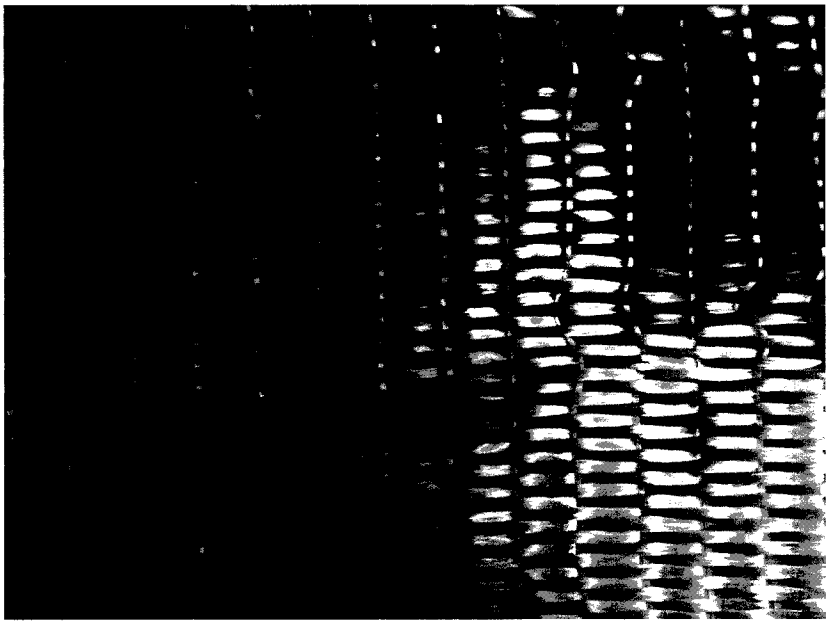

Figure 3-8 Reinforcement 2: TG18U50 E-glass unidirectional fabric from JB Martin

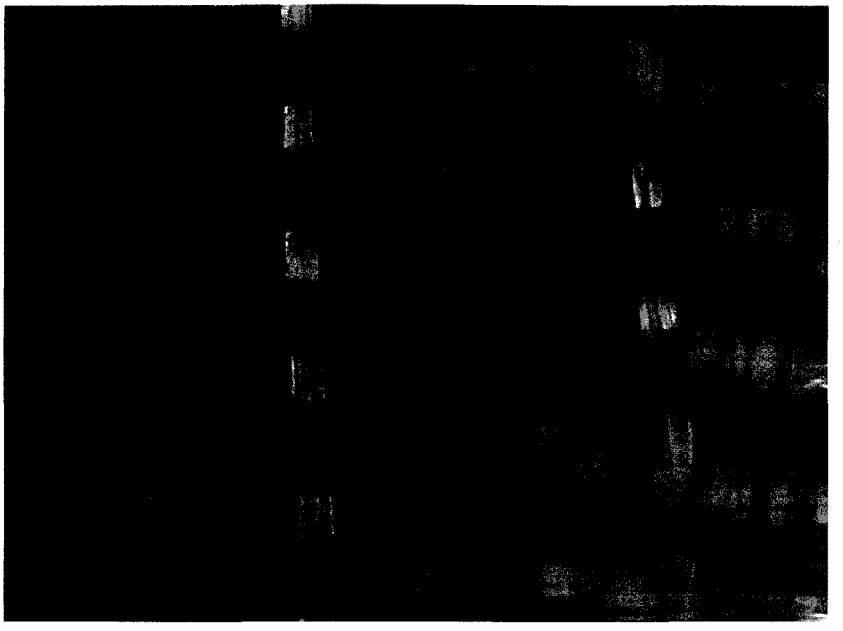

Figure 3-9 Magnified view of Reinforcement 2

Resin was substituted by a silicone fluid from Clearco Products Co., Inc. PSF-50-*cSt* with a room temperature viscosity of 50 *cSt* or 0.048 $Pa \cdot s$. According to the supplier, the viscosity of 50 *cSt* remains constant over time and it is sufficient to simulate the flow characteristics of low viscosity VARTM epoxy resin. Silicone oil is also substantially easier to clean up than resin. The viscosity was compared directly to Glycol epoxy resin D. E. R. ^{TM} 736 from Dow Epoxy, which ranged from 30 *cSt* to 60 *cSt* at room temperature depending on molecular chain length [63]. Furthermore, silicone fluid does not cure like epoxy – which means that the viscosity will remain constant throughout the experiments unless a dramatic temperature change occurs. According to Clearco, PSF-50-*cSt* will have constant viscosity of 50 *cSt* up to $38^{\circ}C$, which is well above room temperature [64].

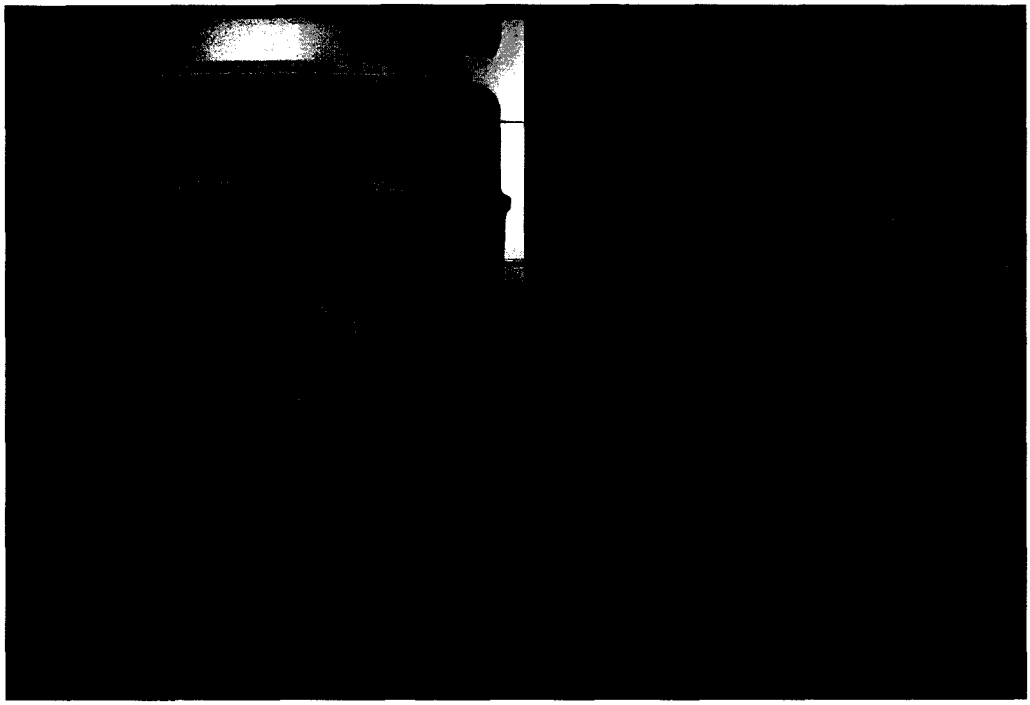

Figure 3-10 Silicone fluid Clearco Product Co., Inc. PSF-50-*cSt*

Some properties of the silicone fluid are given in the Table 3-1:

Table 3-1 Properties of the silicone fluid

Viscosity	Specific gravity	Specific heat @ 25°C	Boiling point
50 *cSt* (0.048 *Pa.s)*	0.96	0.36 *Cal/g/°C*	>250°*C*

Upon installing all equipments and instruments introduced above, the experimental setup looks like:

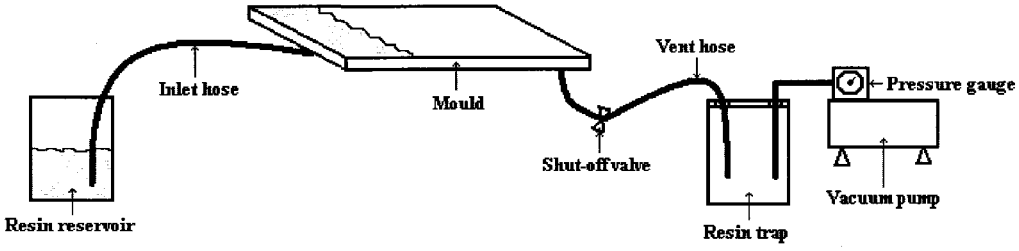

Figure 3-11 RTM experimental setup

Vacuum in the mould was generated using oil-less diaphragm pump GAST Manufacturing DAA-V715A-EB capable of achieving a maximum pressure of 4 atm and pulling a maximum vacuum of approximately 1 atm, as used in the present thesis.

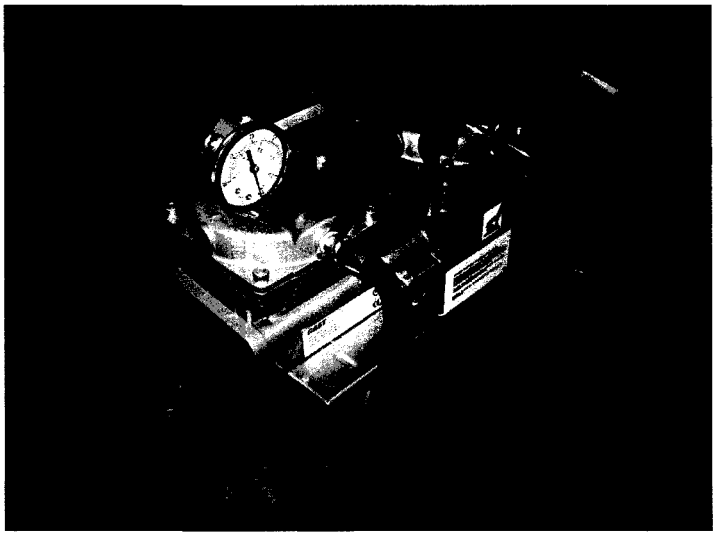

Figure 3-12 Vacuum pump GAST Manufacturing DAA-V715A-EB

The resin trap is an apparatus which serves as a tool preventing resin from entering the pump inlet. Use of a trap is mandatory in all cases and it is especially critical

in cases where the vacuum port is located in the centre of the mould. In this case, some resin will enter the vacuum vent prior to the complete filling of the mould. Without the trap, the resin will enter directly into the pump inlet which could lead to permanent damage.

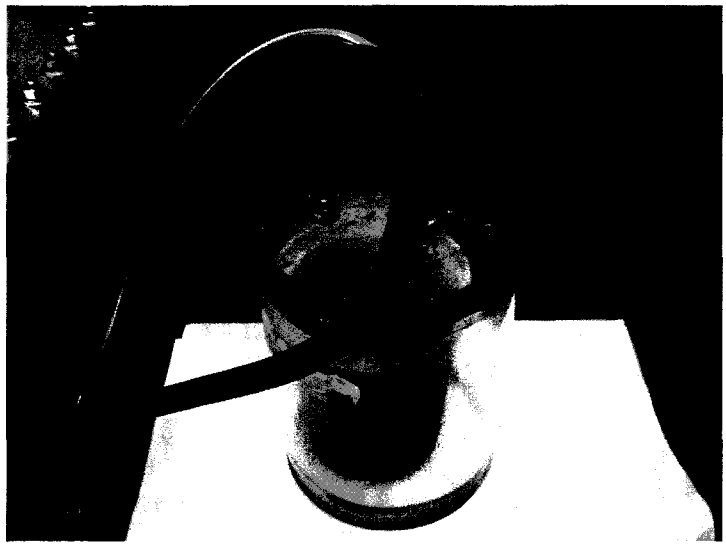

Figure 3-13 Resin trap

The trap is sealed to ensure vacuum at all time and a safety bucket is placed inside to avoid the resin from dripping directly into the trap. Once the safety bucket is full, the trap is opened to empty the safety bucket. The vacuum hose connected to the pump has an inner diameter of 9.53 *mm* and is capable of withstanding a pressure of 2 *MPa* at 21*°C*.

3.2 Procedure

It is crucial to ensure consistent vacuum within the mould. As mentioned previously, all gaps between the mould base plate and cover plate were sealed using Silicone sealant P-W6H284 from GE Sealant & Adhesives. To validate the seal, leak tests were done by reading the vacuum level indicated by the pressure transducer while the pump was running. Once near full vacuum was reached, the pump was turned off and the inlet valve was shut – ensuring that no air could get in. If the vacuum level remained constant, a so-called perfect seal was achieved. The pressure was read using pressure transducer reader software built in LabVIEW as shown in Figure 3-14. A few leak tests indicated that there were some leaks within the mould, however the vacuum level remained constant when the pump was running continuously, as seen in Figure 3-14.

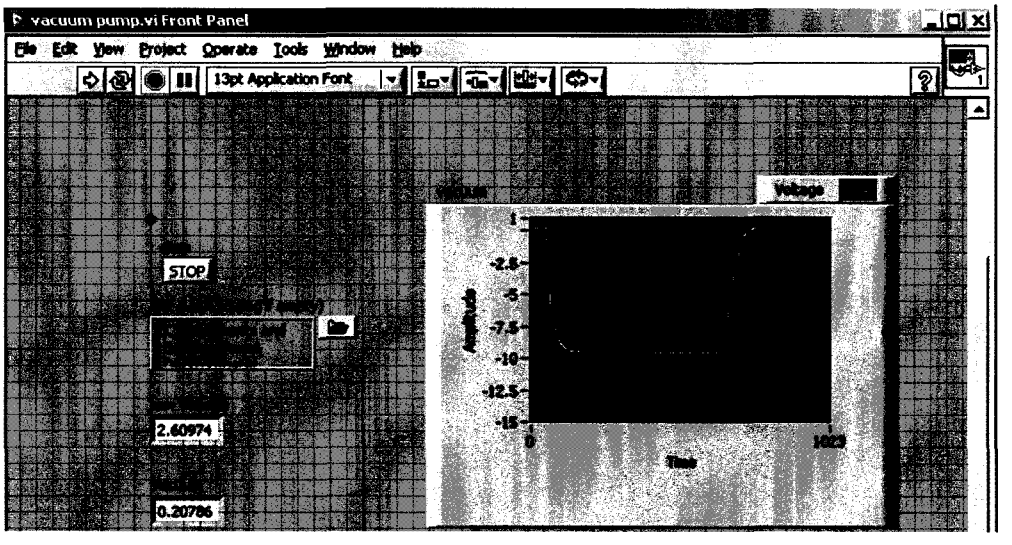

Figure 3-14 Pressure transducer reading application using LabVIEW 7.0

Once the vacuum test was done, the inlet PVC hose with inner diameter of 0.95 *cm* was clamped and placed inside the resin reservoir as shown in Figure 3-15. The reservoir had a capacity of 2 litres.

Figure 3-15 Resin reservoir with inlet PVC hose

Once the vacuum state was achieved, the clamp was released and the resin was drawn in to the mould. The infusion process was then recorded with a digital video camera – Canon PowerShot S2 IS.

4 Results and Validation

4.1 RTM Simulation in 2D and Experiments

For the RTM experiments seven different cases were selected, each characterised by varying factors such as the number of layers of reinforcement, location of inlets, location of a vent, permeability of fabrics and the presence of inserts. In all cases, a first simulation was run using approximate permeability values. Then, these values were adjusted according to results of the first simulation, so as to replicate the fill time and the flow front shape seen in experiments. The number of nodes used in the simulations was 1107 with a grid spacing of 0.02 *m*. These values were based on computational power available at the time. General indication of run times with the exception of cases 2 and 7, four layers of Reinforcement 1 were used in order to achieve a fibre volume fraction of 29%, which is an appropriate value for a random mat. Case 2 used two layers of Reinforcement 1, and the fibre volume fraction achieved from that case was 15%. Case 7 used two layers of Reinforcement 2; the fibre volume fraction achieved was also near 15%. The permeability values assigned to each case varied within the range of $1.2\times10^{-10}\ m^2$ and $2.1\times10^{-9}\ m^2$ – this was due to the fact that the simulations were strictly based on replicating the experimental results. Permeability measurements are very sensitive to various factors. According to many research works [18, 43, 65-68], a large scatter in identified permeability values is very common. A possible explanation to these variations can be shown by the study carried out by R. Gauvin *et al.* This showed that surface density variation on reinforcements could influence the local flow behaviour and affect the flow parameter's prediction with Darcy's law [69]. The results from the study

indicate the differences between the calculated fill time using minimum and maximum values of the mat surface density taken from measurements. The difference is quite large as shown in Figure 4-1.

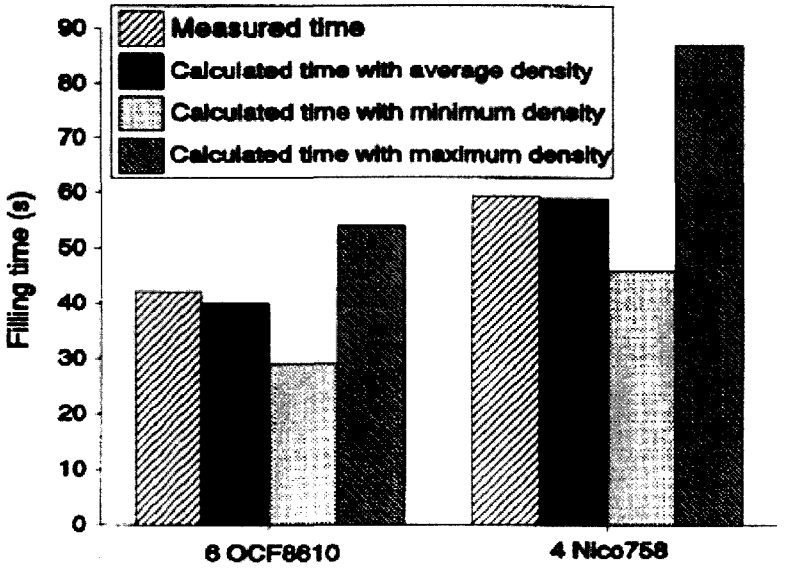

Figure 4-1 Comparison of mold fill time calculated using the average, minimum and maximum surface densities and the experimentally measured fill time [69]

A large variation in experimental permeability and calculated permeability can also be seen in a study done by Merotte, Simacek and Advani [70]. In this work, Kozeny-Carman relation was used to calculate the permeability of woven E-glass fabric at different fibre volume fractions, and then the values were compared to the experimental data.

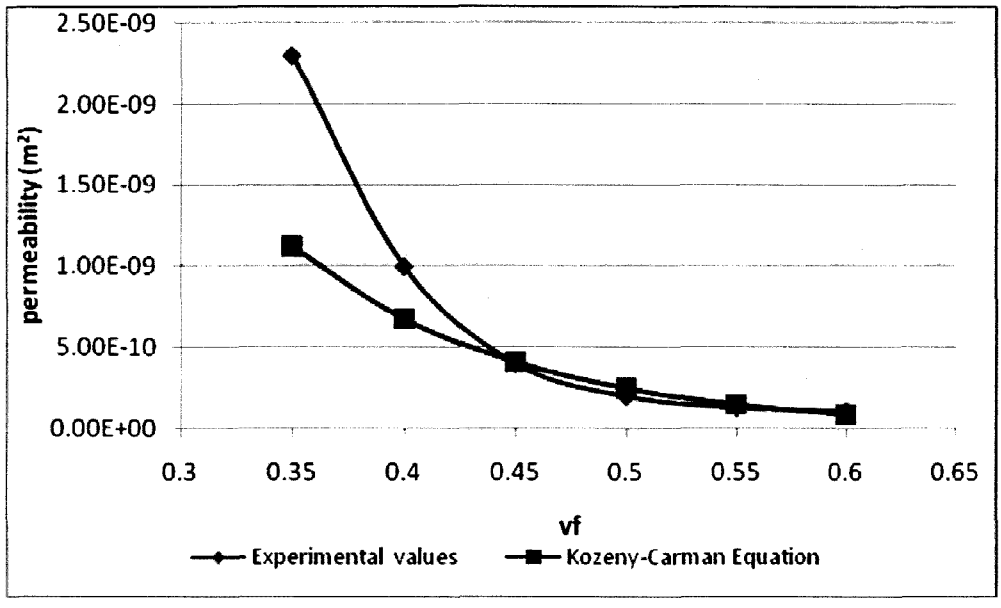

Figure 4-2 Permeability values for E-glass woven fabric and its fit with the Kozeny-Carman relation at higher fiber volume fractions

The large variation in permeability can be seen in Figure 4-2 where the fibre volume fraction is 0.35. The experimental and calculated permeabilities differ by a factor of almost 2 which is a tremendous variation considering how important this value is for simulations. The material used in the experiment done by Merotte *et al.* is also a woven fabric which in theory should be more consistent in permeability than a random mat that is used in the present work. Another example of variation in permeability is the round-robin study that was performed and presented in a seminar at the Flow Processes in Composite Materials (FPCM) conference in Montreal, 2009. Samples of fabrics were handed out to different laboratories which were asked to report the in-plane permeability of the samples using their own methods of measurements. The variation in the in-plane permeability values returned was tremendous –up to 200% discrepancies between certain values were seen. Thus, it can be noted that a large variation in predicted permeability

values and measured permeability values is very common, and it is usual practice to identify permeability data in order to fit the results obtained by the experiment.

4.1.1 Case 1: 4 layers of random mat with a single inlet at port 8

Case 1 featured a resin inlet at port 8 and a vacuum port at port 11. All other ports remained closed and sealed tightly. For convenience, the walls are noted as north, east, west and south on the mould.

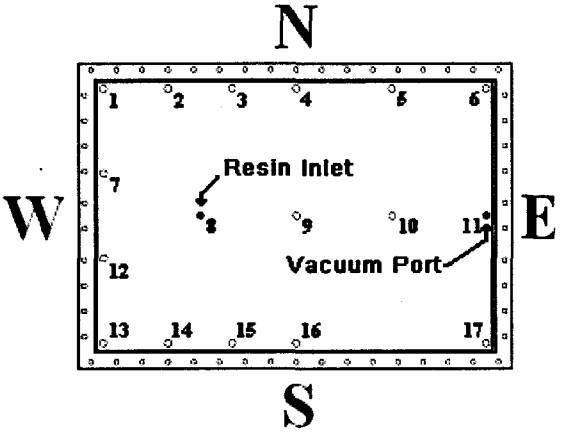

Figure 4-3 Case 1 configuration

With this configuration the flow front should progresses evenly in all radial directions around the inlet, creating a circular saturated zone that expands in radial shape until the flow front reaches the mould walls. Resin flow should speed up along the wall eventually catching up with resin flowing along the longer centre line of the mould and leading to a relatively straight flow front progressing to the east. However, this scenario could be disrupted by the presence of edge effects which would make the flow front accelerate

near the wall creating a 'w' shaped flow front. After adjusting the permeability value to fit the experiment, an isotropic permeability value of $1.2\times10^{-10}\,m^2$ was used in this simulation. The circles inside the grid represent the saturated preform and the colors represent the level of resin pressure.

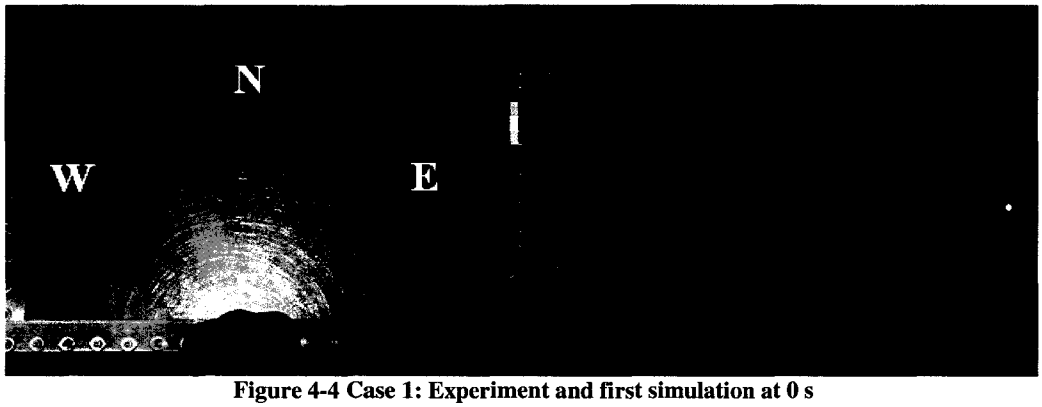

Figure 4-4 Case 1: Experiment and first simulation at 0 s

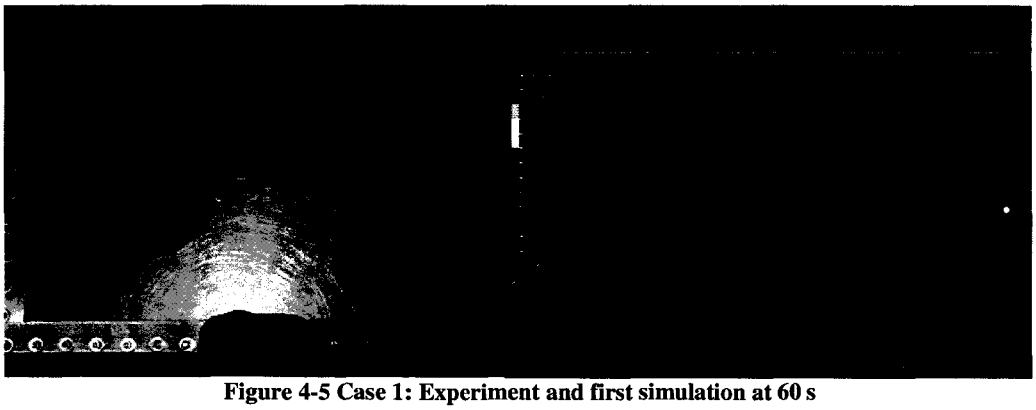

Figure 4-5 Case 1: Experiment and first simulation at 60 s

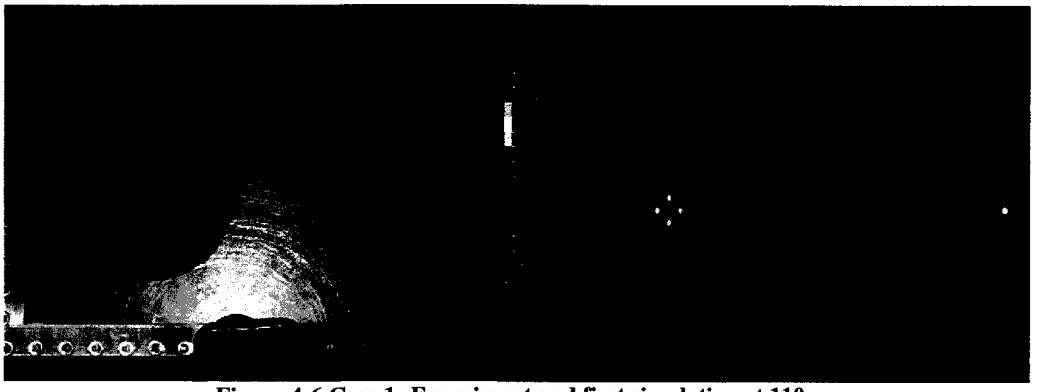

Figure 4-6 Case 1: Experiment and first simulation at 110 s

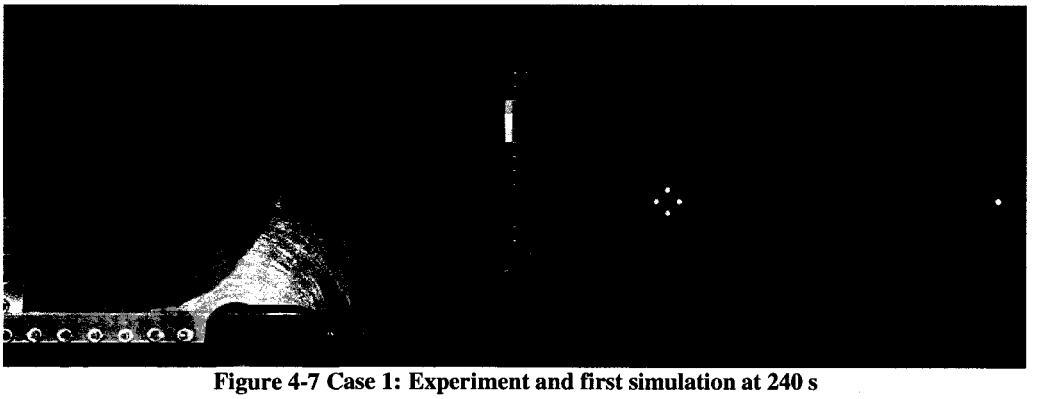

Figure 4-7 Case 1: Experiment and first simulation at 240 s

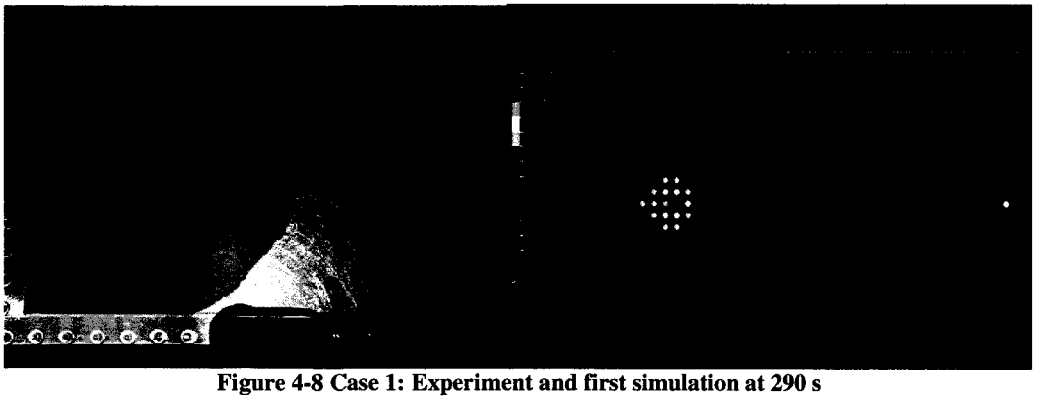

Figure 4-8 Case 1: Experiment and first simulation at 290 s

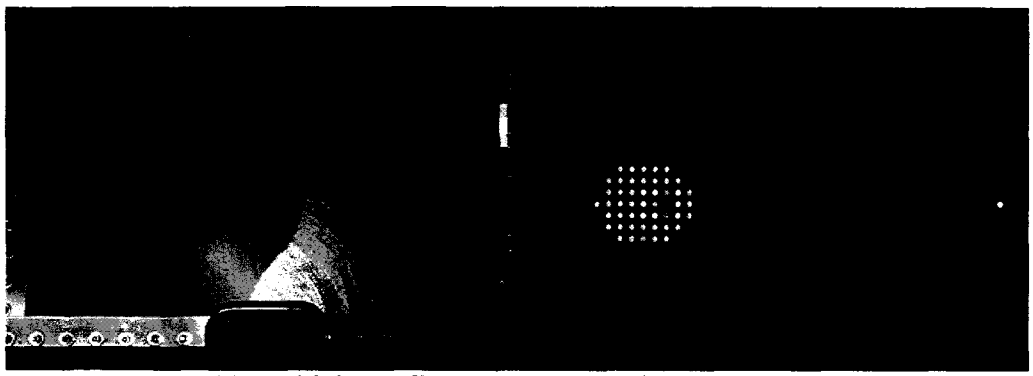

Figure 4-9 Case 1: Experiment and first simulation at 360 s

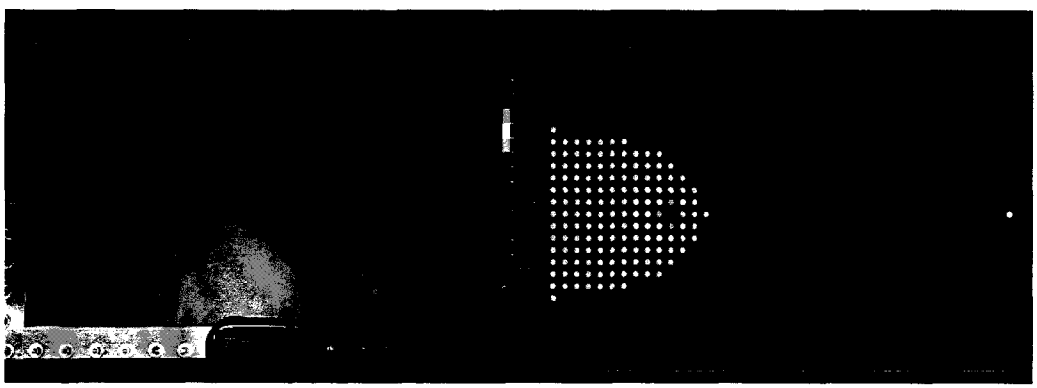

Figure 4-10 Case 1: Experiment and first simulation at 540 s

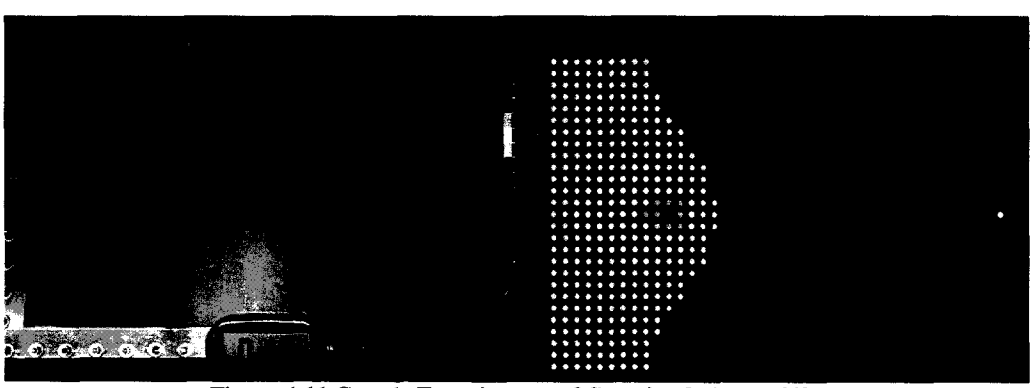

Figure 4-11 Case 1: Experiment and first simulation at 660 s

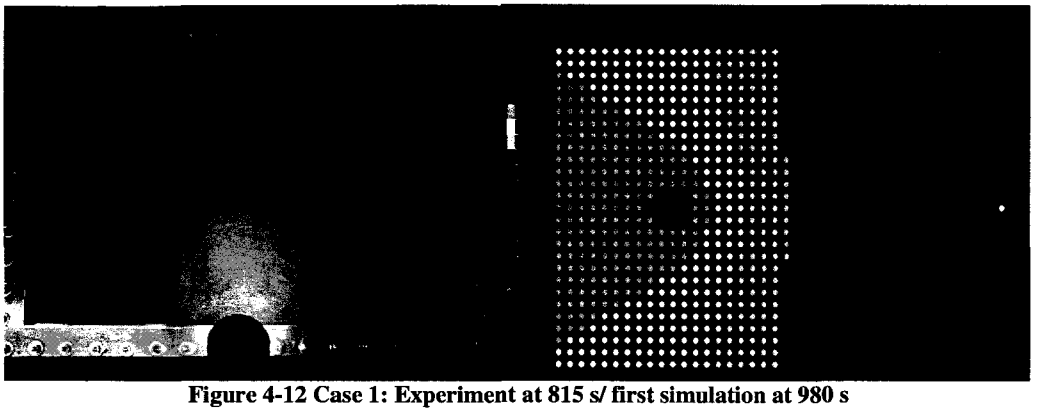

Figure 4-12 Case 1: Experiment at 815 s/ first simulation at 980 s

As expected, images from the experiment generally reflect well the predicted flow characteristics stated above. A relatively symmetric circular flow front progresses until it reaches the west wall at 110 seconds, as shown in Figure 4-6. The flow along the wall speeds up because one of the directions towards which the fluid can go has been eliminated as reflected by the pressure distribution shown in color. From this point, a visible edge effect occurs where the flow accelerates considerably along both north and south walls towards the east. Figure 4-10 shows the edge effect clearly, as the experimental flow front along the wall overtakes the central flow front. Resin continues to move faster along the walls moving ahead of the central flow front, and eventually the mould is filled at around 800 seconds. However, fill time for the simulation was nearly 165 seconds longer than the experiment. The edge effect explains this result since the flow accelerated considerably along the wall. In Figure 4-11, the flow front along the edges clearly reaches the further end of the wall before the central part of the flow front. Fill time was significantly reduced during the experiment because of this. The following figures illustrate a second simulation with edge effect implemented through an increase of permeability along the north and south walls. The permeability value assigned to the

segments located along the edge – indicated by red lines – of the mould was increased to $3.6\times10^{-10}\,m^2$. Going back to the Hagen-Poiseuille relation, permeability for the channel flow can be described by $K = h^2/12$ which means that having a permeability of $3.6\times10^{-10}\,m^2$ is equivalent to having a flow channel of 0.067 *mm*.

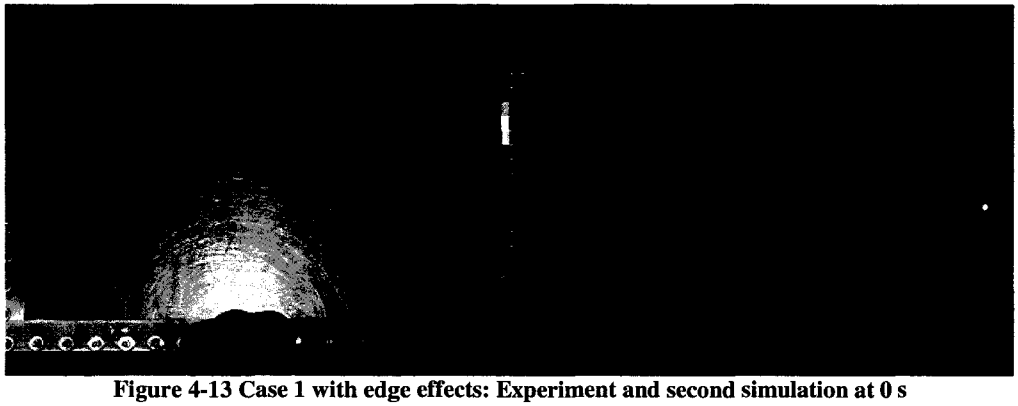

Figure 4-13 Case 1 with edge effects: Experiment and second simulation at 0 s

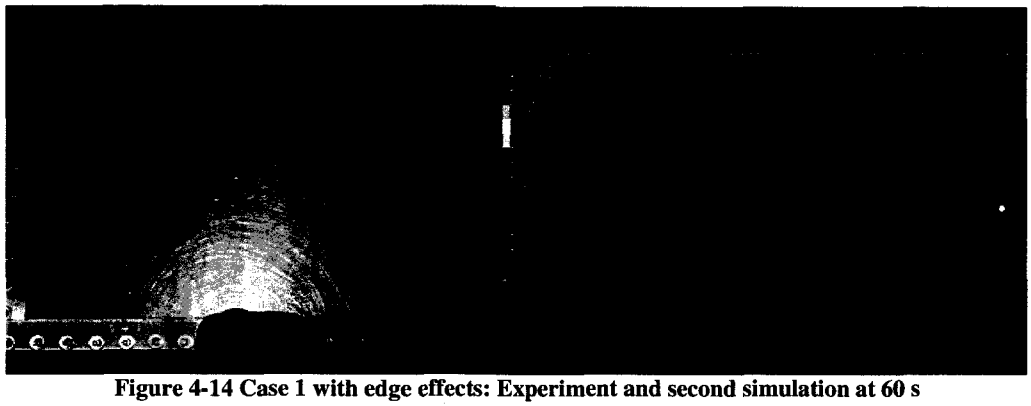

Figure 4-14 Case 1 with edge effects: Experiment and second simulation at 60 s

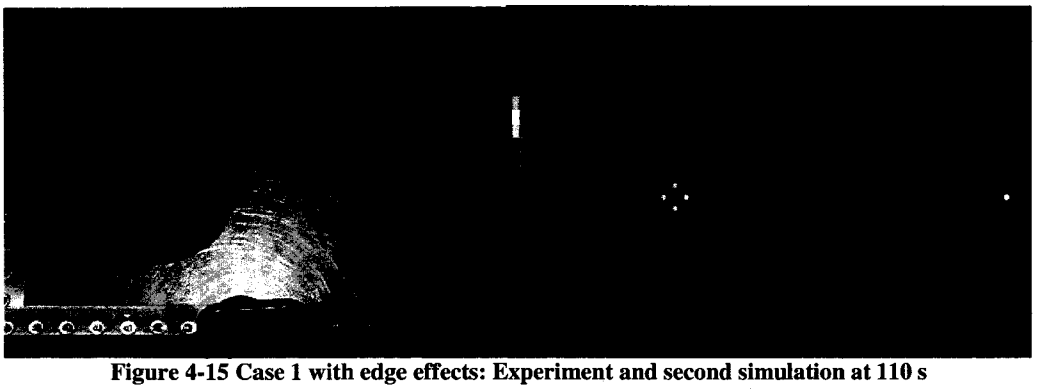

Figure 4-15 Case 1 with edge effects: Experiment and second simulation at 110 s

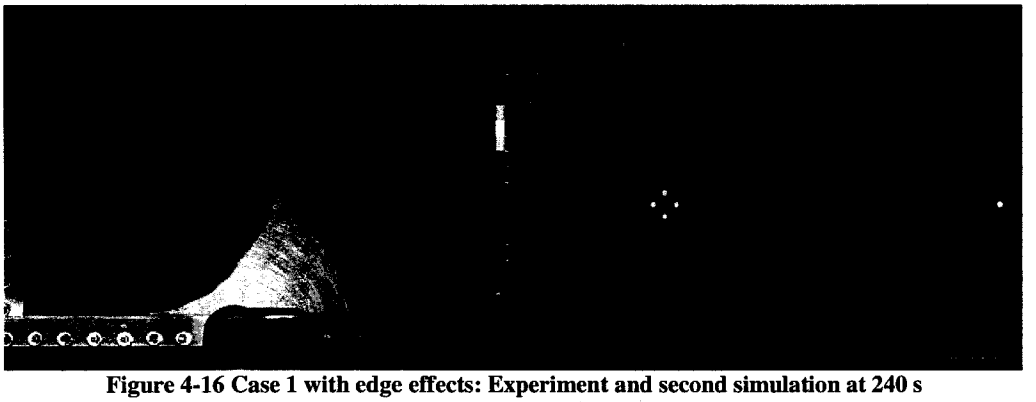

Figure 4-16 Case 1 with edge effects: Experiment and second simulation at 240 s

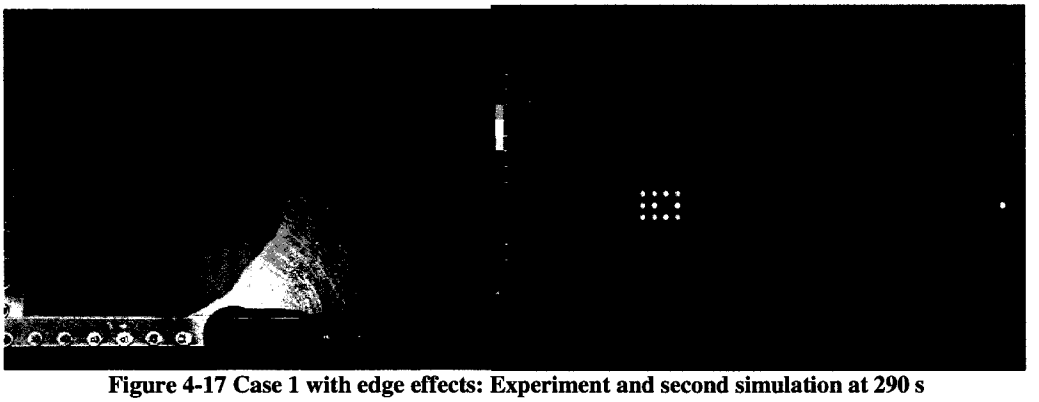

Figure 4-17 Case 1 with edge effects: Experiment and second simulation at 290 s

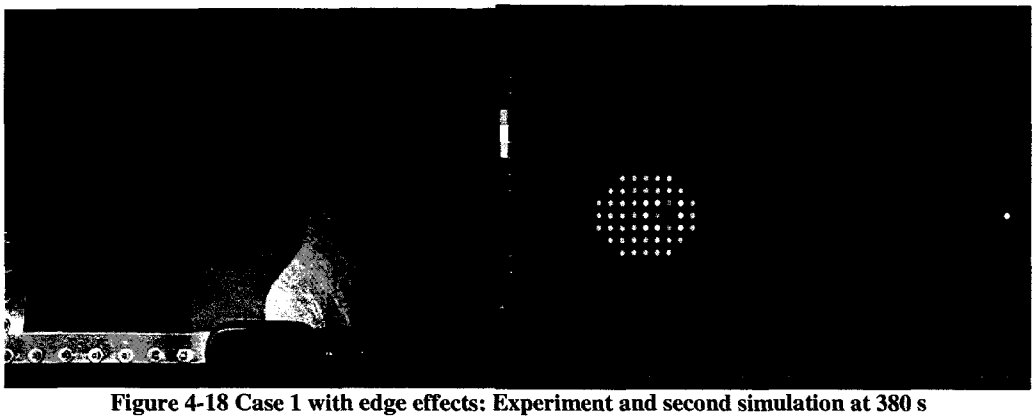

Figure 4-18 Case 1 with edge effects: Experiment and second simulation at 380 s

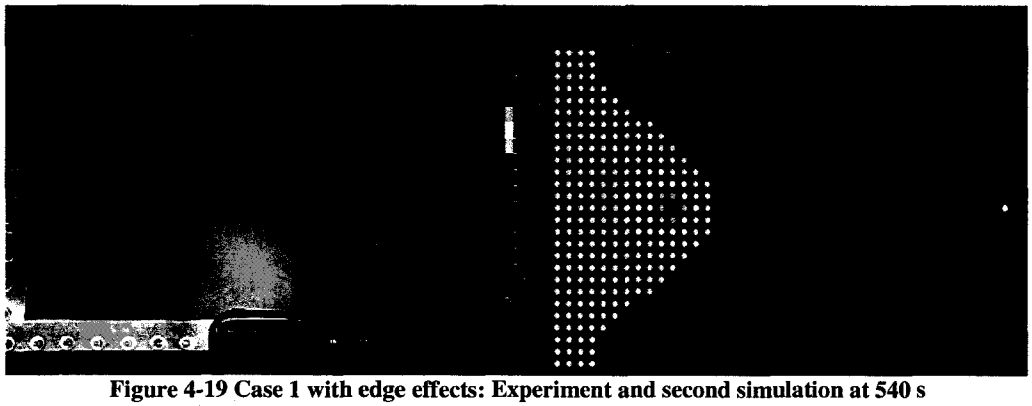

Figure 4-19 Case 1 with edge effects: Experiment and second simulation at 540 s

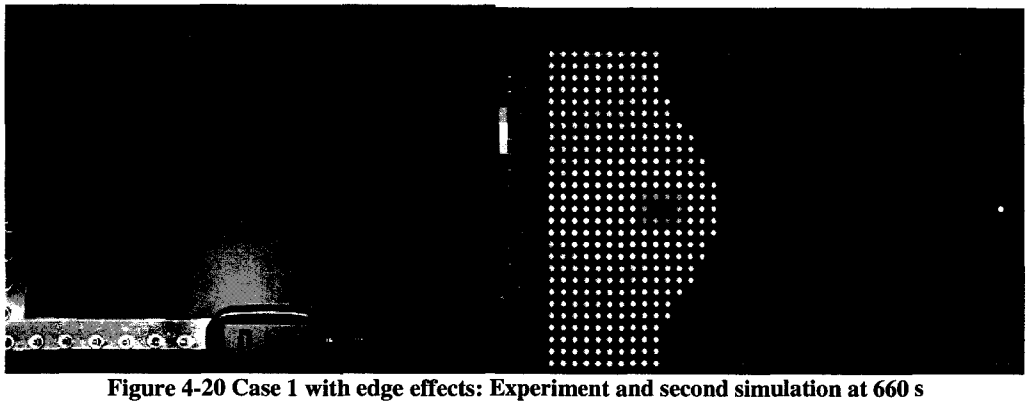

Figure 4-20 Case 1 with edge effects: Experiment and second simulation at 660 s

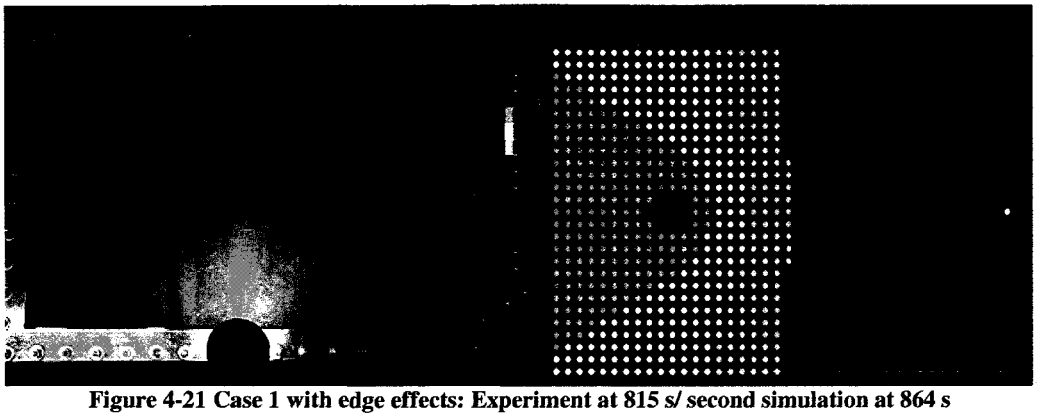

Figure 4-21 Case 1 with edge effects: Experiment at 815 s/ second simulation at 864 s

With edge effects implemented, the simulated flow resembles the experimental flow more closely. Especially in Figure 4-19 and Figure 4-20, the edge effects can be seen very clearly as the flow accelerates quicker around the walls. The fill time has decreased significantly as well; the time it took for the mould to be filled was about 2 minutes shorter than it was for the simulation without the edge effects. This can be explained by referring back to Equation (2.46), where the fill time t decreases as the permeability K increases.

4.1.2 Case 2: 2 layers of random mat with a single inlet at port 8

The setup for this case is identical to case 1, with the exception that only 2 layers of Reinforcement 1 were used instead of 4. This reduces the fibre volume fraction from 29% to 15%. It was verified that this lower fibre volume fraction was still sufficient to prevent displacement of the preform inside the cavity – a phenomenon commonly known as 'fibre washing'. Having less reinforcement layers leads to an increase in flow speed as the porosity and permeability increases. Ultimately, the flow front progression should be

similar to that seen with case 1 but faster. After a few simulation trials, the permeability of the fabric chosen for the first simulation in this case was $1.5\times10^{-10}\,m^2$. The first simulation did not feature different permeability values at the edges.

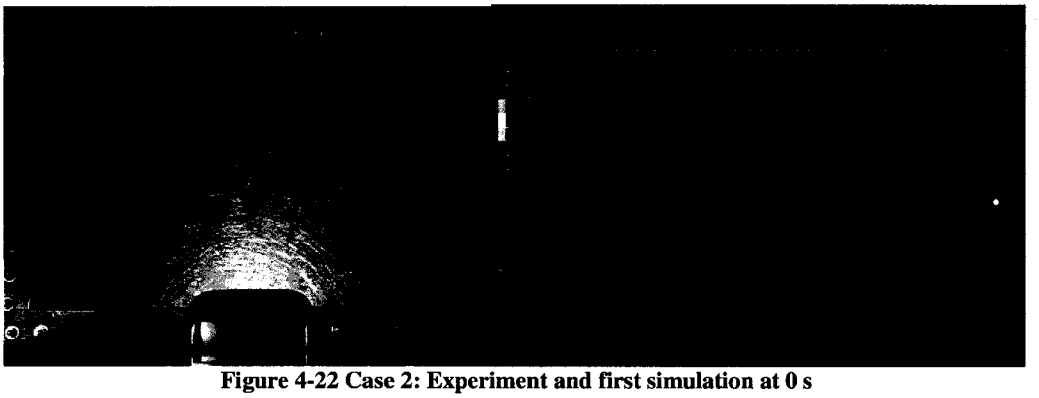

Figure 4-22 Case 2: Experiment and first simulation at 0 s

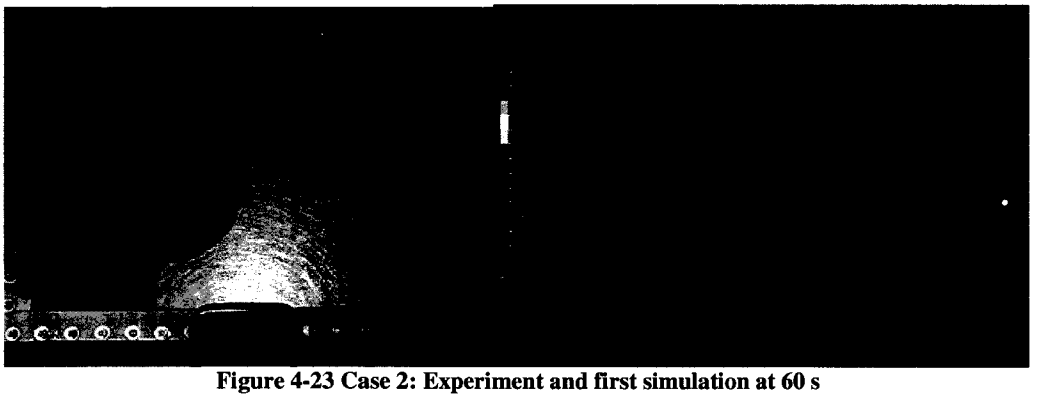

Figure 4-23 Case 2: Experiment and first simulation at 60 s

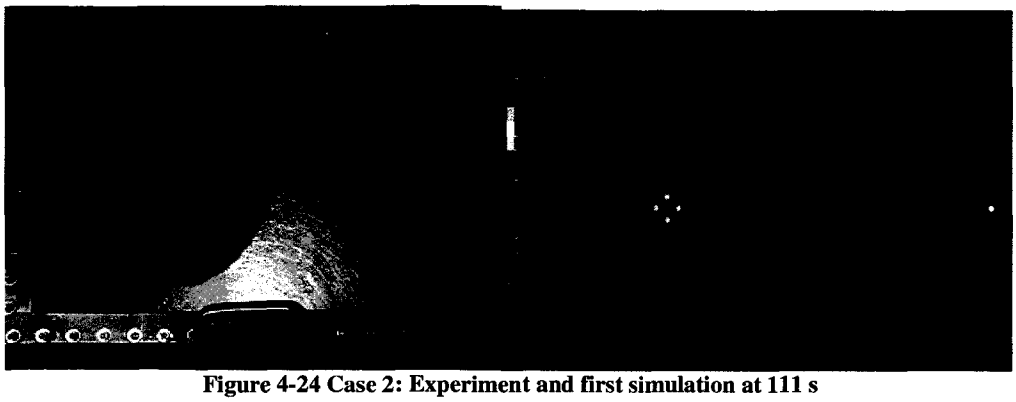

Figure 4-24 Case 2: Experiment and first simulation at 111 s

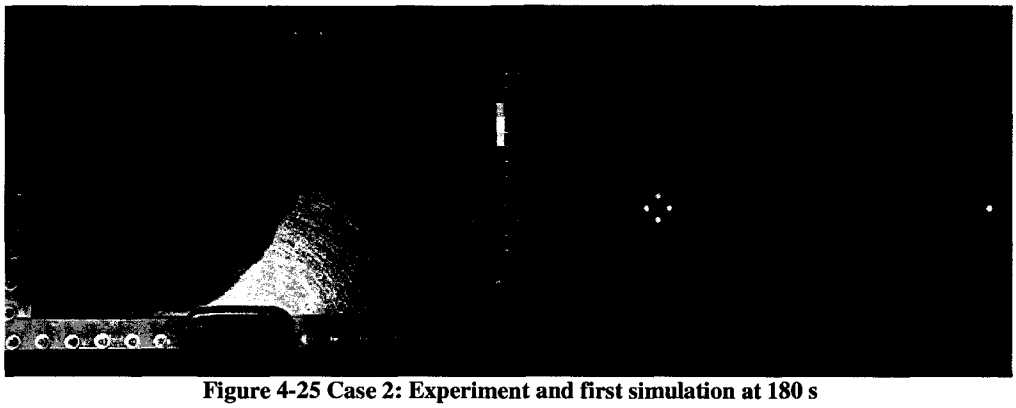

Figure 4-25 Case 2: Experiment and first simulation at 180 s

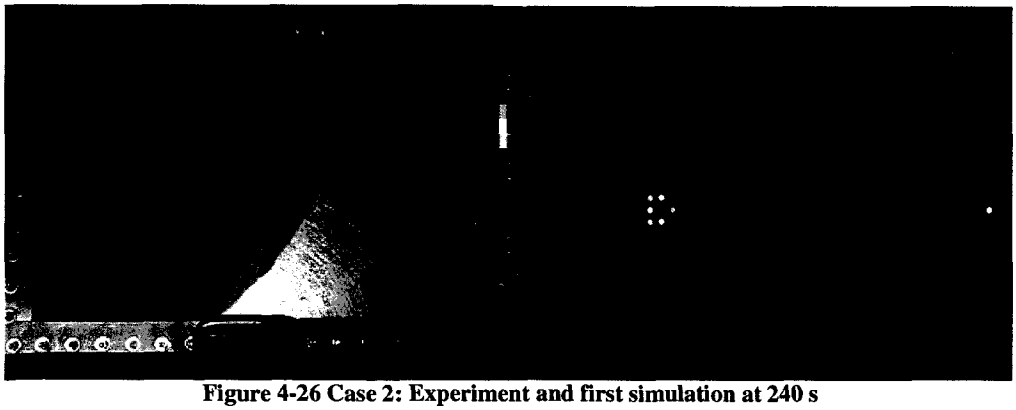

Figure 4-26 Case 2: Experiment and first simulation at 240 s

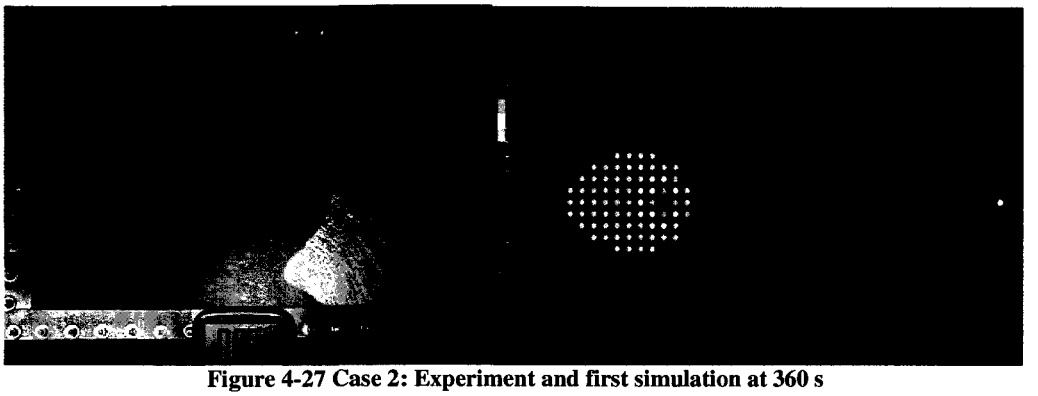

Figure 4-27 Case 2: Experiment and first simulation at 360 s

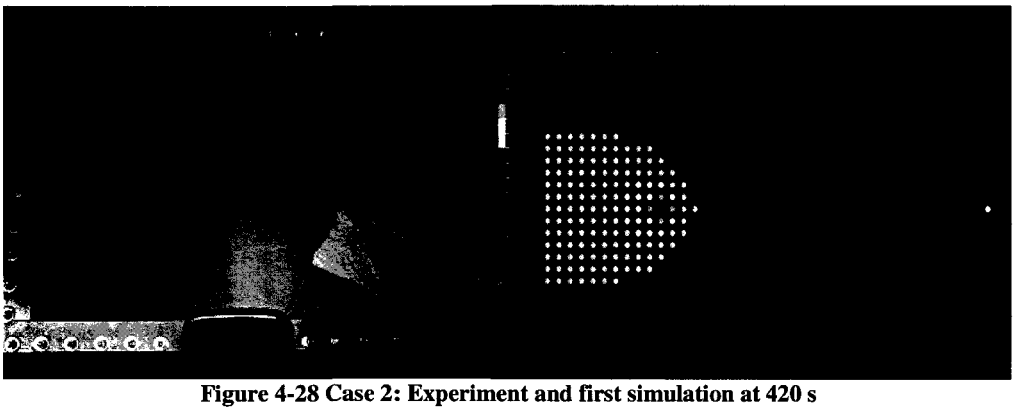

Figure 4-28 Case 2: Experiment and first simulation at 420 s

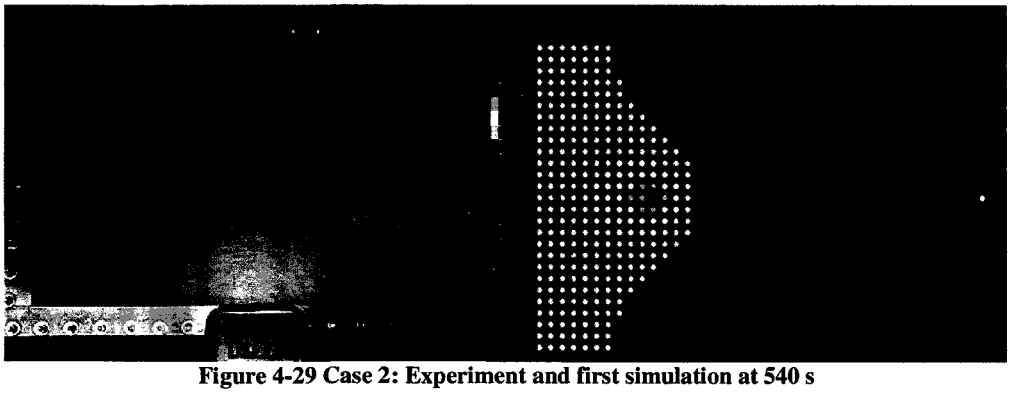

Figure 4-29 Case 2: Experiment and first simulation at 540 s

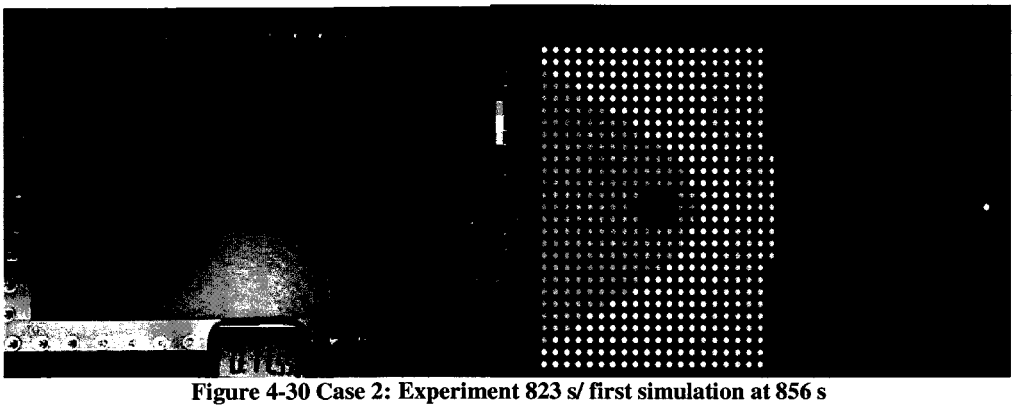

Figure 4-30 Case 2: Experiment 823 s/ first simulation at 856 s

As expected, the flow moved quicker than it did for the 4 layer case – finishing the filling process at 715 seconds, more than a minute sooner than the previous case. However, some clear trails of edge effect were found in this case; these are particularly visible in Figure 4-27 to Figure 4-29. Also, air bubbles were seen within the cavity during the experiment, which are indicative of leakage of air within the cavity. Beyond obvious problems of quality in an eventual composite, air leakage has many adverse effects on these experiments. First it reduces the pressure gradient applied on the resin, and then leaked air also sometimes helps the resin to travel faster, by pushing the resin during its travel within the cavity. A new simulation with edge effect implemented improved the results. In this case, the permeability along the walls was increased to $7.0\times10^{-10}\ m^2$ as indicated by red lines. This value of permeability along the edge was equivalent to having a 0.09 *mm* wide flow channel along the edges.

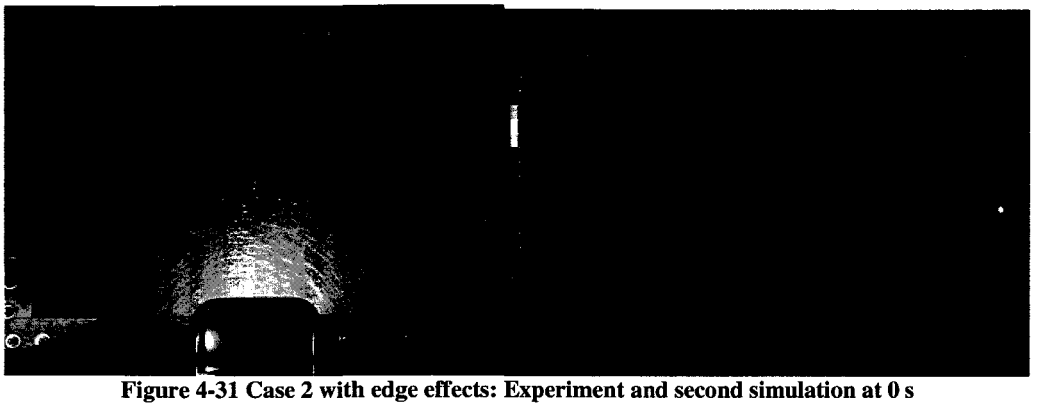

Figure 4-31 Case 2 with edge effects: Experiment and second simulation at 0 s

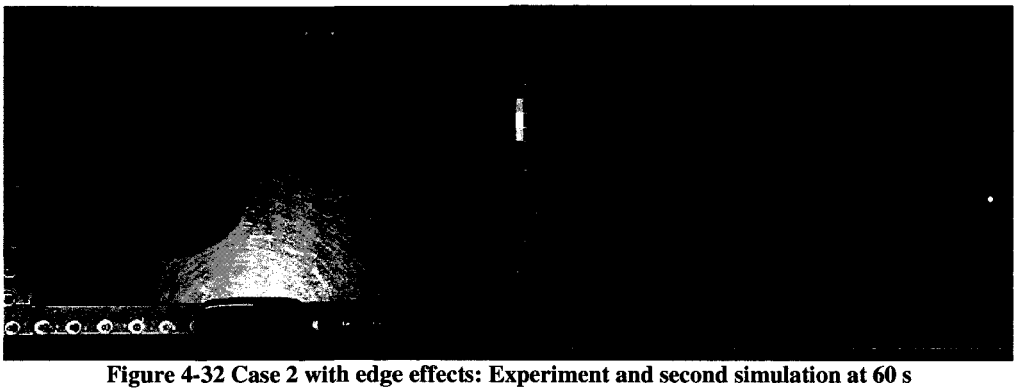

Figure 4-32 Case 2 with edge effects: Experiment and second simulation at 60 s

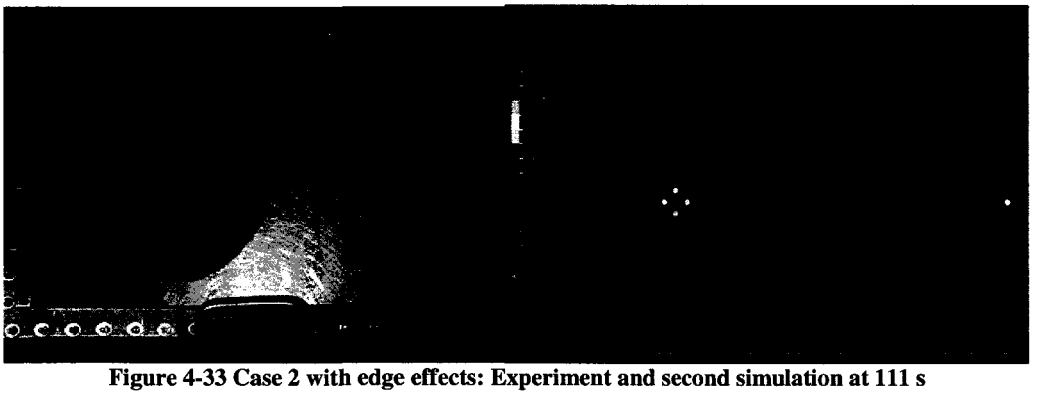

Figure 4-33 Case 2 with edge effects: Experiment and second simulation at 111 s

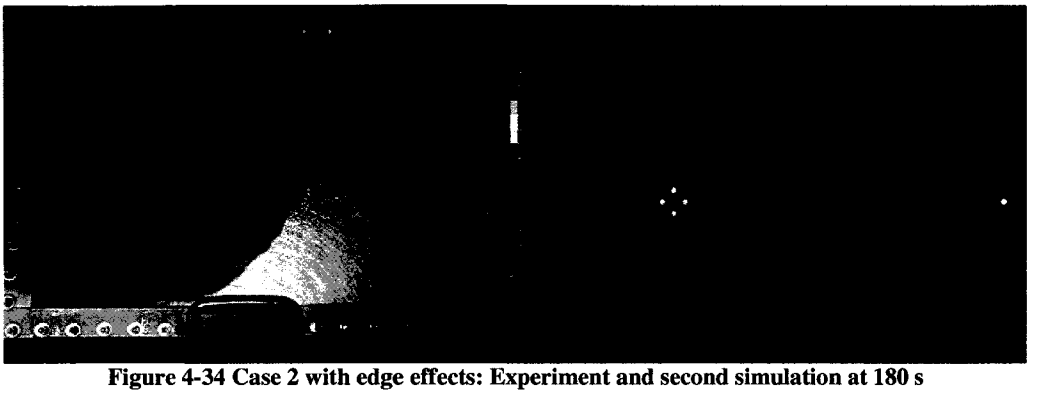

Figure 4-34 Case 2 with edge effects: Experiment and second simulation at 180 s

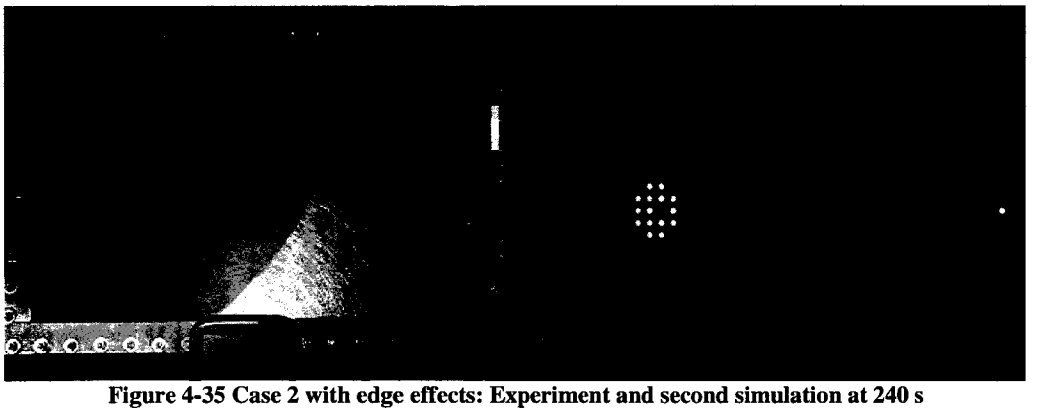

Figure 4-35 Case 2 with edge effects: Experiment and second simulation at 240 s

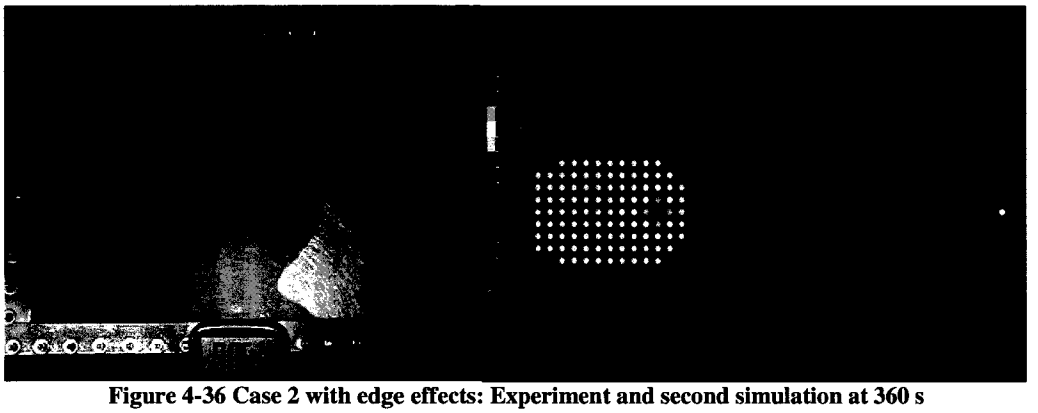

Figure 4-36 Case 2 with edge effects: Experiment and second simulation at 360 s

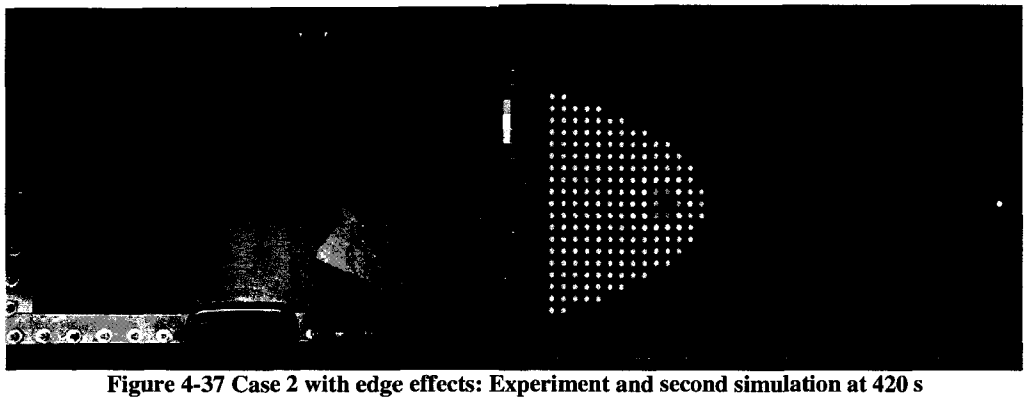

Figure 4-37 Case 2 with edge effects: Experiment and second simulation at 420 s

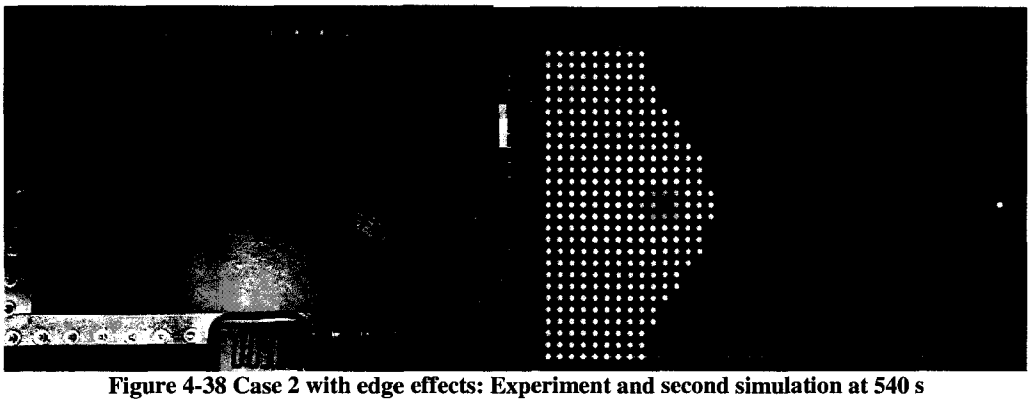

Figure 4-38 Case 2 with edge effects: Experiment and second simulation at 540 s

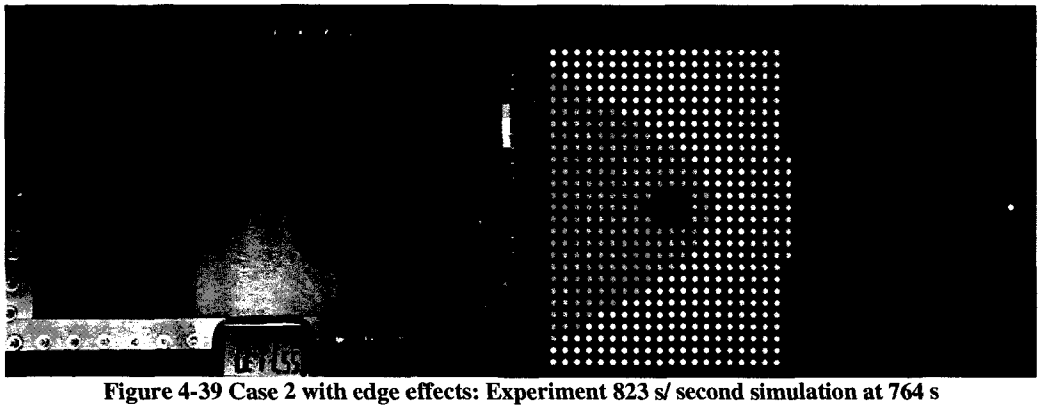

Figure 4-39 Case 2 with edge effects: Experiment 823 s/ second simulation at 764 s

Results of the second simulation were more accurate after the implementation of edge effects. However, the overall flow patterns seen in the experiment and second simulation still showed discrepancies between them, especially in Figure 4-37 and Figure 4-38. As mentioned before, possible leakage of air bubbles could have resulted in such accelerated flows around the walls. By further increasing the permeability value along the wall beyond $7.0\times10^{-10}\,m^2$, the edge effects could have been simulated better especially on the north and south walls. Thus, a third simulation with adjusted permeability along the wall was done in order to further improve the simulation. Permeability along the north and south walls were increased to $2.0\times10^{-9}\,m^2$ and the permeability along the east wall were slightly increased to $1.0\times10^{-9}\,m^2$. The values were chosen carefully after a few trials and errors. These values represented a flow channel gap of 0.15 *mm* and 0.11 *mm*, respectively.

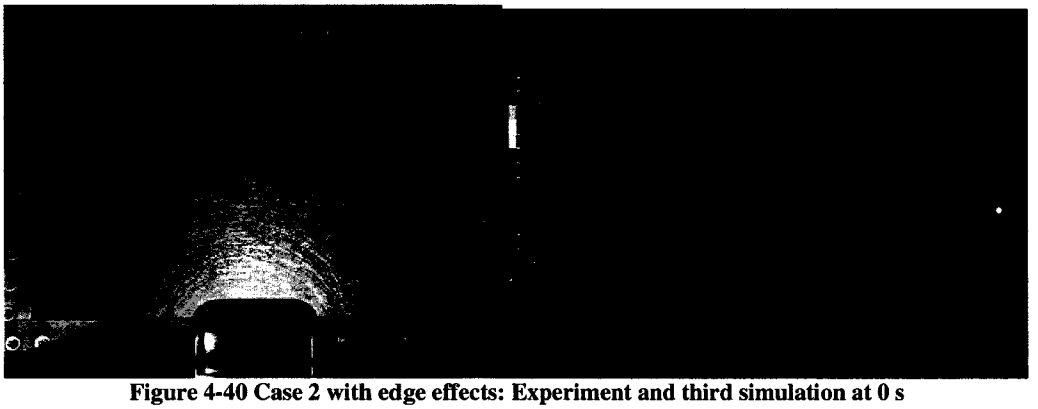

Figure 4-40 Case 2 with edge effects: Experiment and third simulation at 0 s

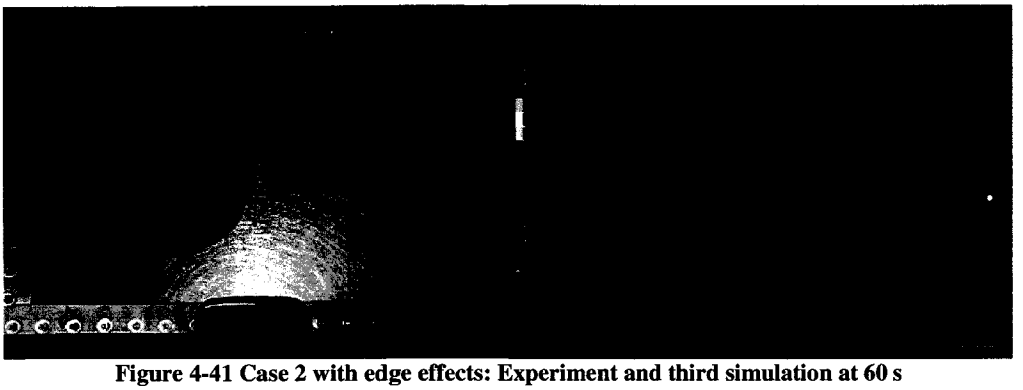

Figure 4-41 Case 2 with edge effects: Experiment and third simulation at 60 s

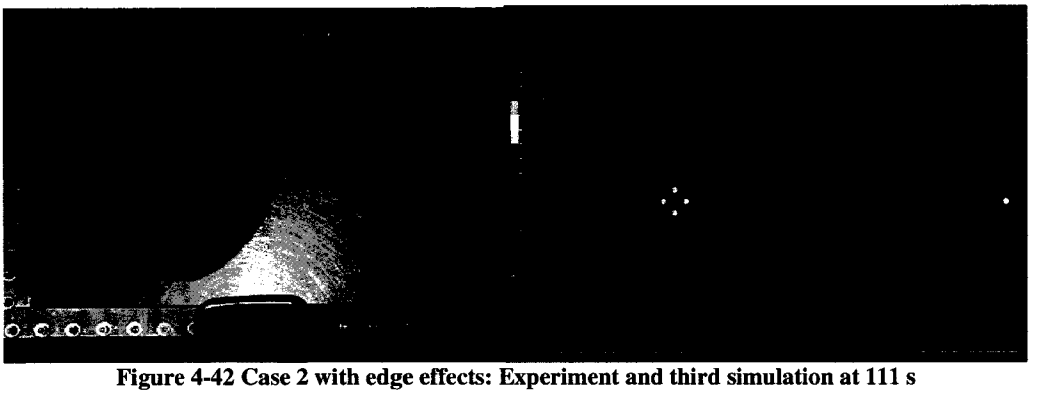

Figure 4-42 Case 2 with edge effects: Experiment and third simulation at 111 s

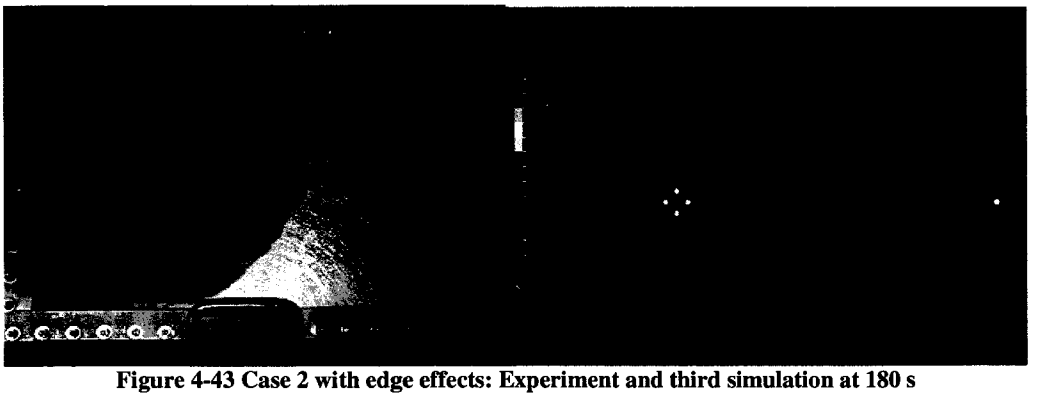

Figure 4-43 Case 2 with edge effects: Experiment and third simulation at 180 s

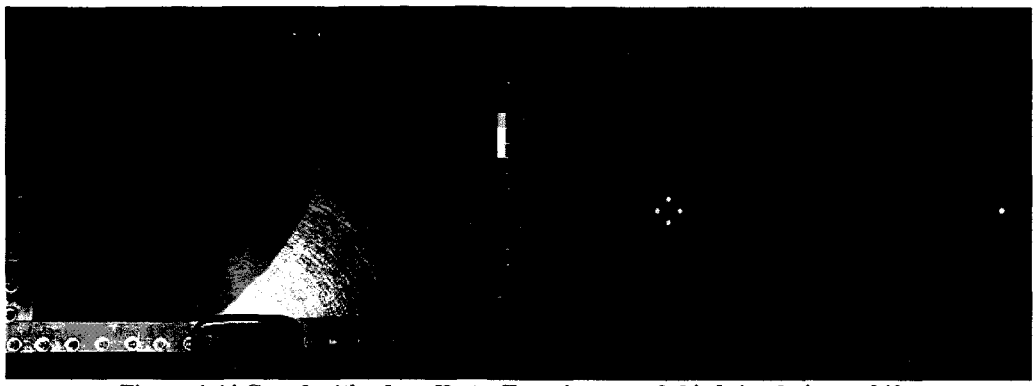

Figure 4-44 Case 2 with edge effects: Experiment and third simulation at 240 s

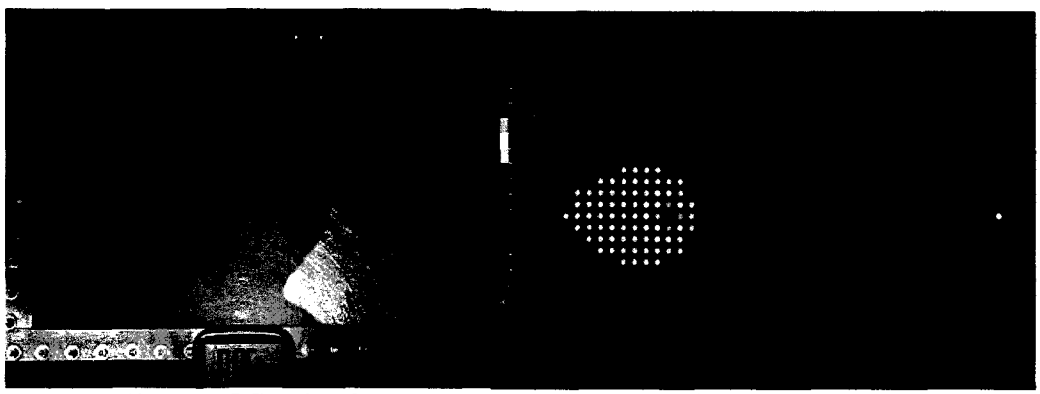

Figure 4-45 Case 2 with edge effects: Experiment and third simulation at 360 s

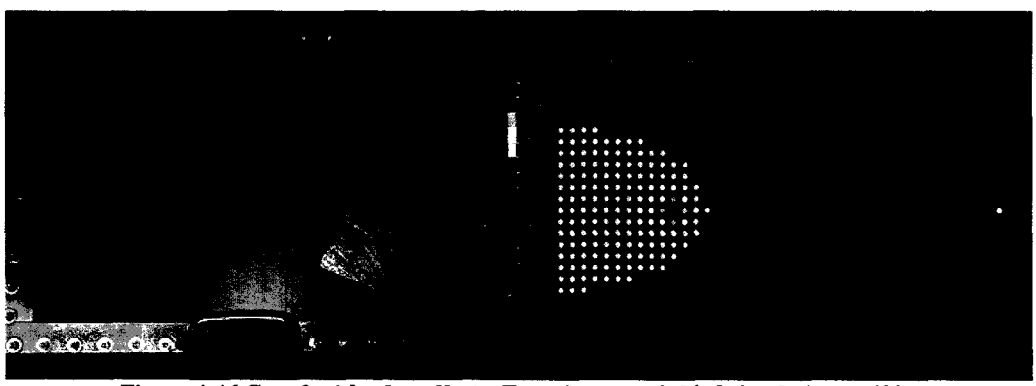

Figure 4-46 Case 2 with edge effects: Experiment and third simulation at 420 s

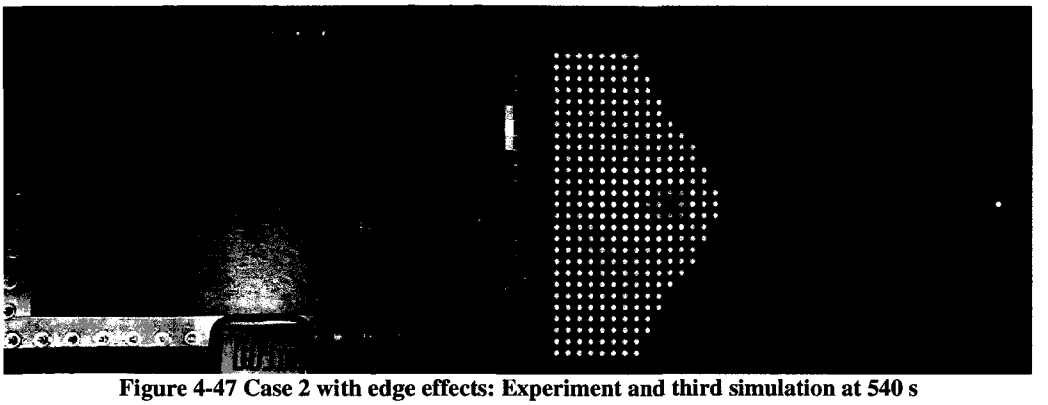

Figure 4-47 Case 2 with edge effects: Experiment and third simulation at 540 s

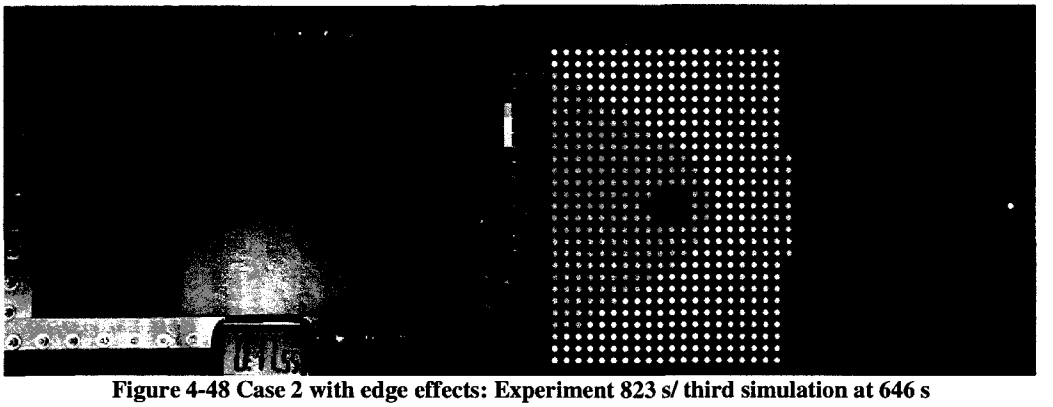

Figure 4-48 Case 2 with edge effects: Experiment 823 s/ third simulation at 646 s

Due to the adjustments, the edge effects on north and south walls were more closely simulated as seen in Figure 4-45. The excessive edge effect shown on east wall was not simulated very well, since the flow seemed to rush around the corners of the cavity for the experiment. Overall, the third simulation showed much better results.

4.1.3 Case 3: 4 layers of random mats with vent at port 10

In cases 1 and 2, the vacuum vent was located near the edge of the east wall at port 11. Due to such configuration, there were no concerns regarding the resin travelling

over the vacuum port which could lead to the filling of the resin trap. In case 3, some resin was bound to enter the vacuum port as the vent was located in port 10 which was away from the east wall. The inlet port was located at port 13 which was the south-west corner.

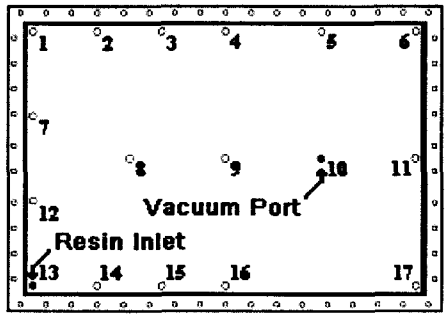

Figure 4-49 Case 3 configuration

The saturated region should start out as quarter circle shaped but as the flow front reaches the north wall this will change. If an edge effect is present, it should alter the shape of flow front running east to an 'S' shape. When the front reaches the vacuum port located at port 10, the shape should once again be altered as the flow front running over the vacuum port should slow down dramatically due to local sink, creating a 'V'- shaped flow. The permeability value set for first simulation after a few trials was $4.0\times10^{-10}\,m^2$.

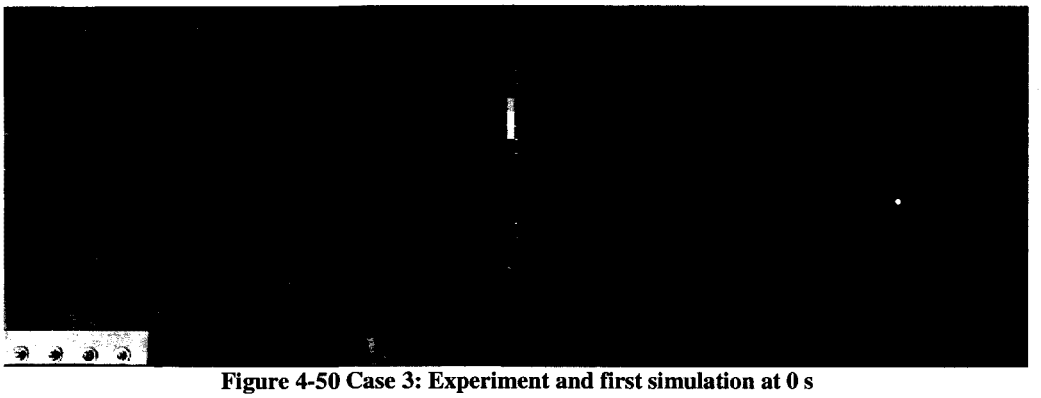

Figure 4-50 Case 3: Experiment and first simulation at 0 s

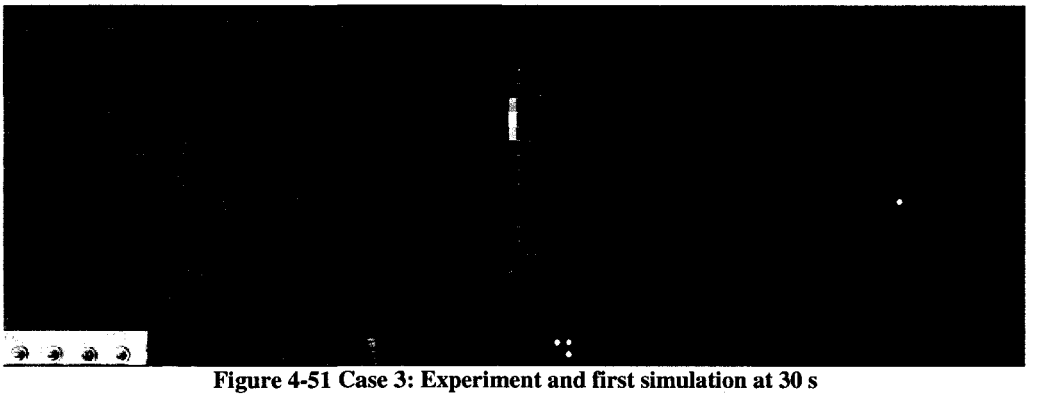

Figure 4-51 Case 3: Experiment and first simulation at 30 s

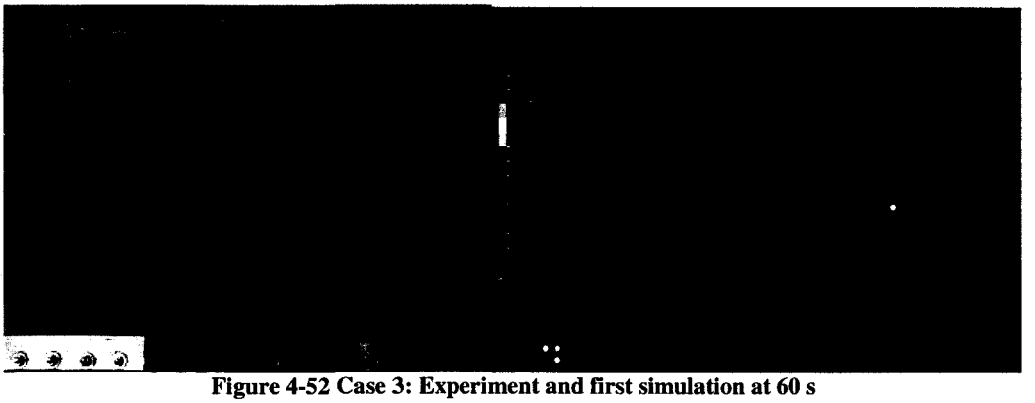

Figure 4-52 Case 3: Experiment and first simulation at 60 s

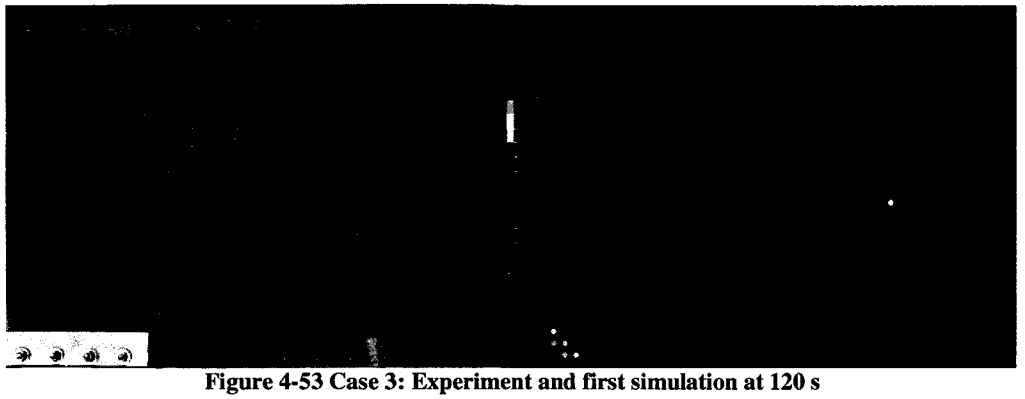

Figure 4-53 Case 3: Experiment and first simulation at 120 s

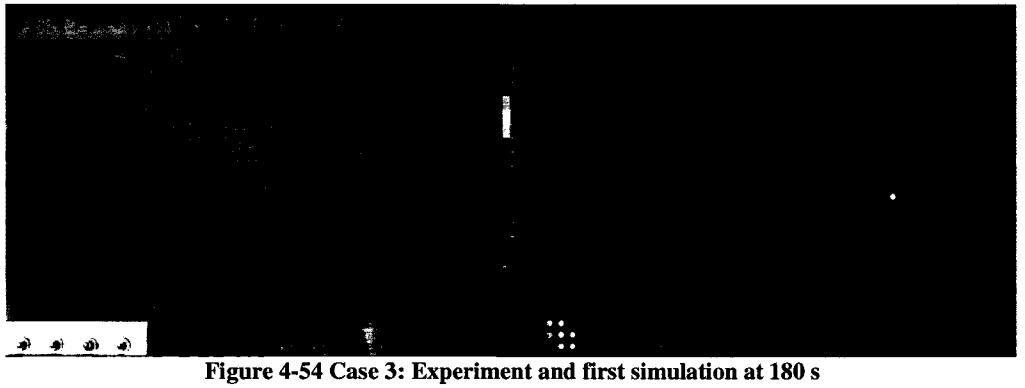

Figure 4-54 Case 3: Experiment and first simulation at 180 s

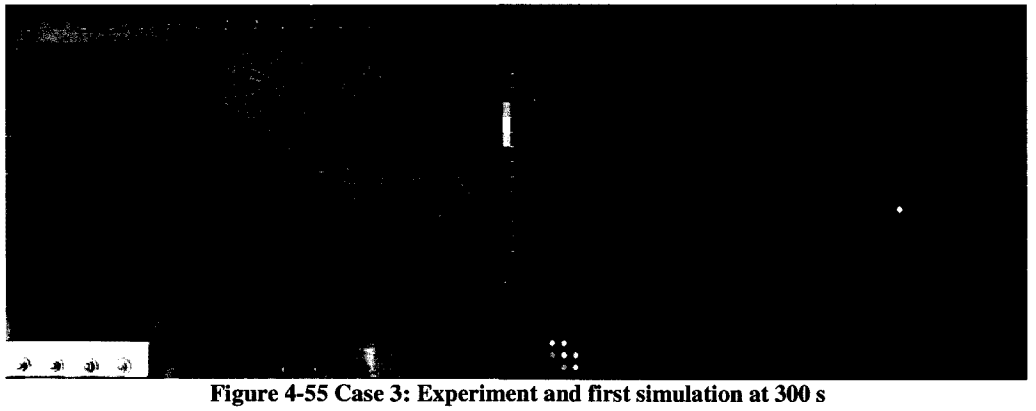

Figure 4-55 Case 3: Experiment and first simulation at 300 s

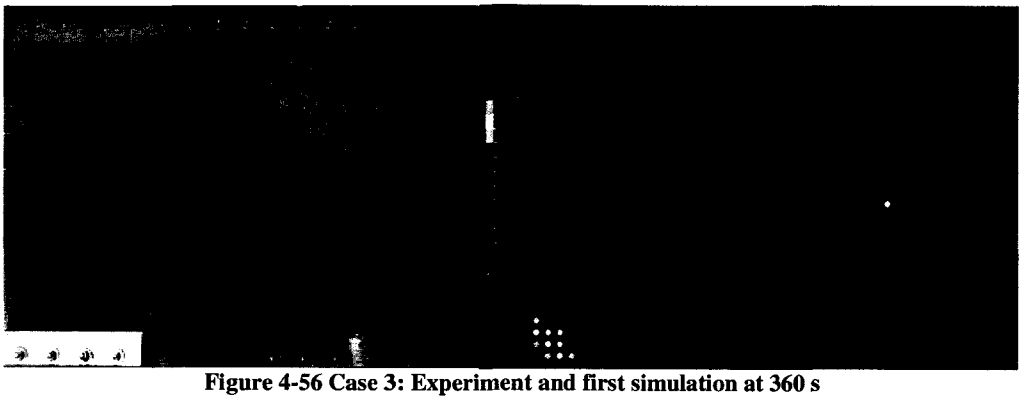

Figure 4-56 Case 3: Experiment and first simulation at 360 s

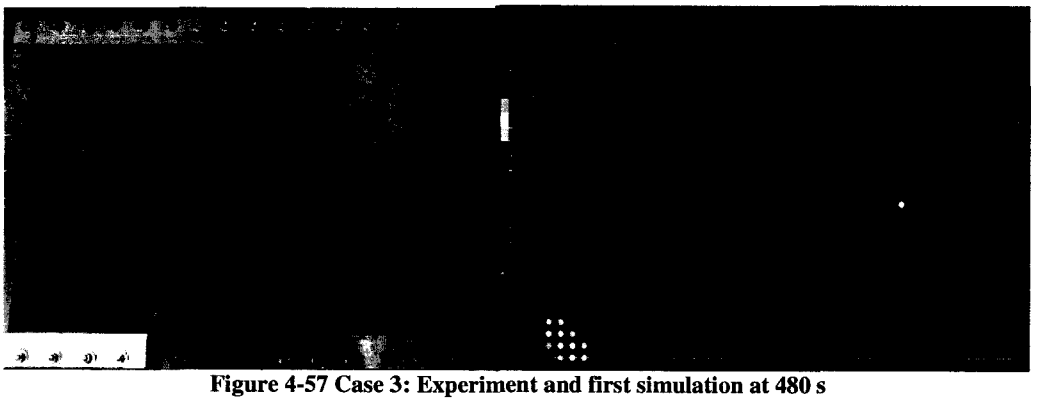

Figure 4-57 Case 3: Experiment and first simulation at 480 s

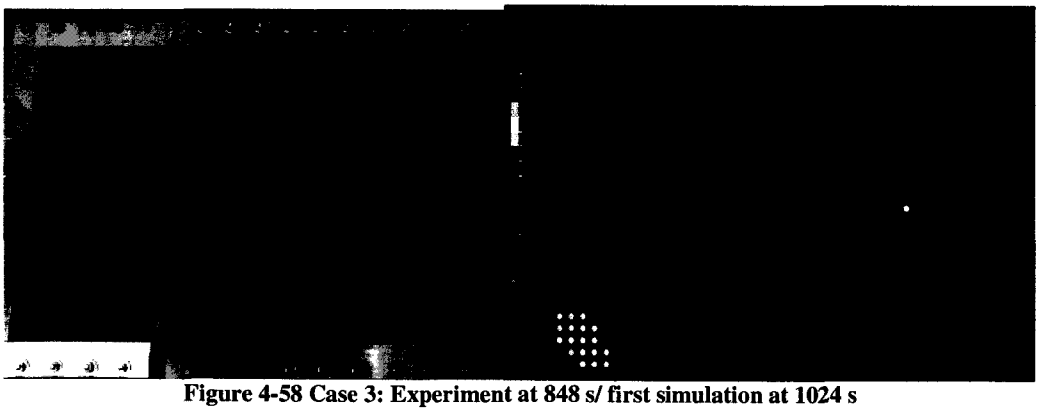

Figure 4-58 Case 3: Experiment at 848 s/ first simulation at 1024 s

As seen from Figure 4-52 through Figure 4-57, edge effect played a major role in the outcome of the experimental flow front progression. The flow has considerably accelerated along all four walls, although in the centre of the mould the experiment and simulation were relatively close. Ultimately, filling experiment completed considerably quicker than the simulation. As seen in Figure 4-58, the behaviour of flow around the vent was quite well simulated as regions north-east to the vent showed a field of low resin pressure. In order to improve the solution, a second simulation was done with the implementation of edge effects. The permeability values along the north and south walls were increased to $2.1\times10^{-9}\,m^2$, and the east and west walls were increased to $7.7\times10^{-10}\,m^2$. The two increased permeability values are equivalent to having flow channels of 0.16 *mm* and 0.10 *mm*, respectively.

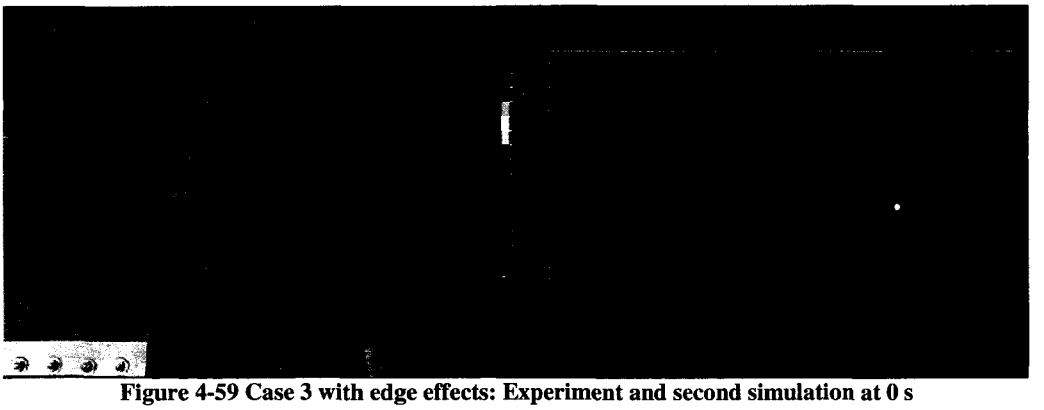

Figure 4-59 Case 3 with edge effects: Experiment and second simulation at 0 s

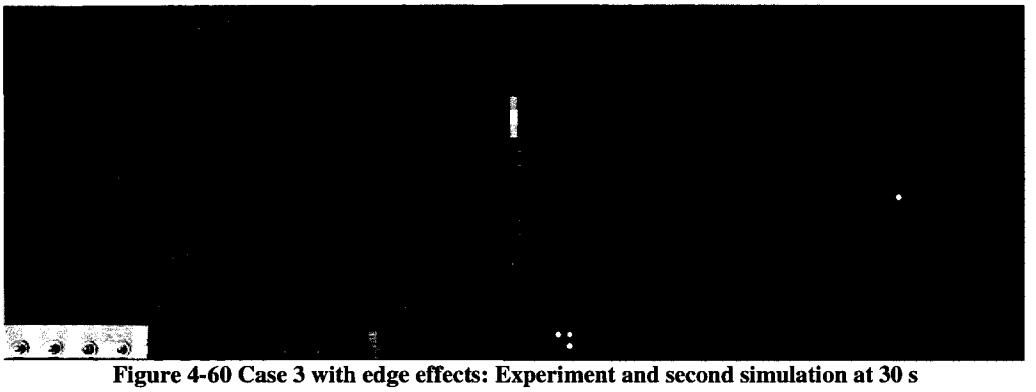

Figure 4-60 Case 3 with edge effects: Experiment and second simulation at 30 s

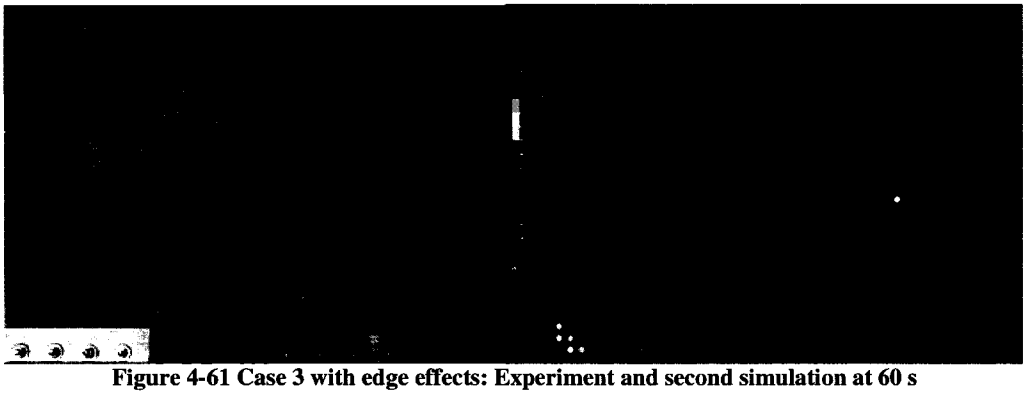

Figure 4-61 Case 3 with edge effects: Experiment and second simulation at 60 s

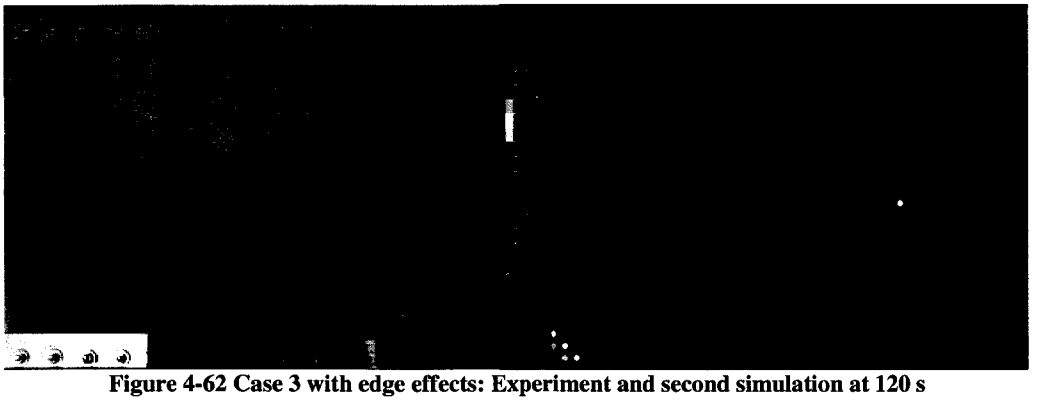

Figure 4-62 Case 3 with edge effects: Experiment and second simulation at 120 s

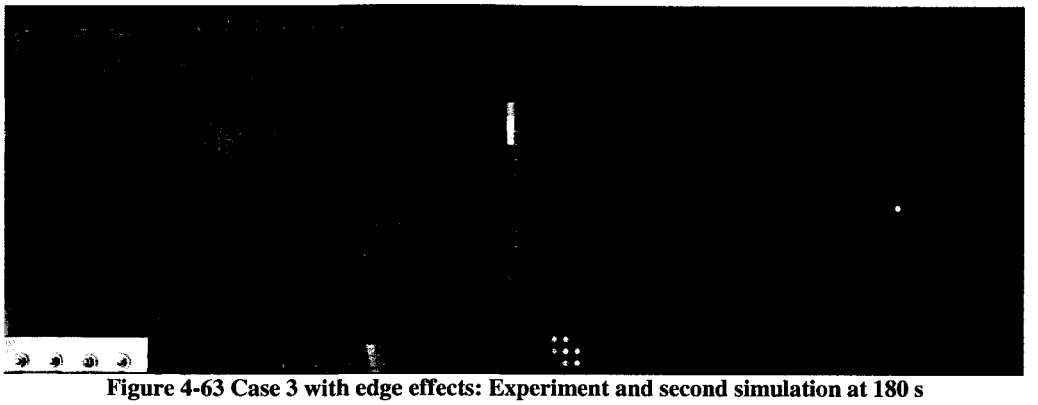

Figure 4-63 Case 3 with edge effects: Experiment and second simulation at 180 s

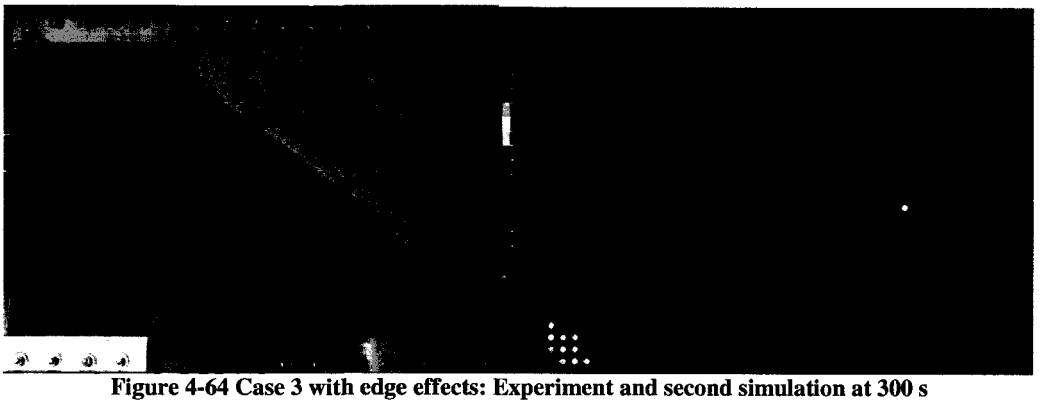

Figure 4-64 Case 3 with edge effects: Experiment and second simulation at 300 s

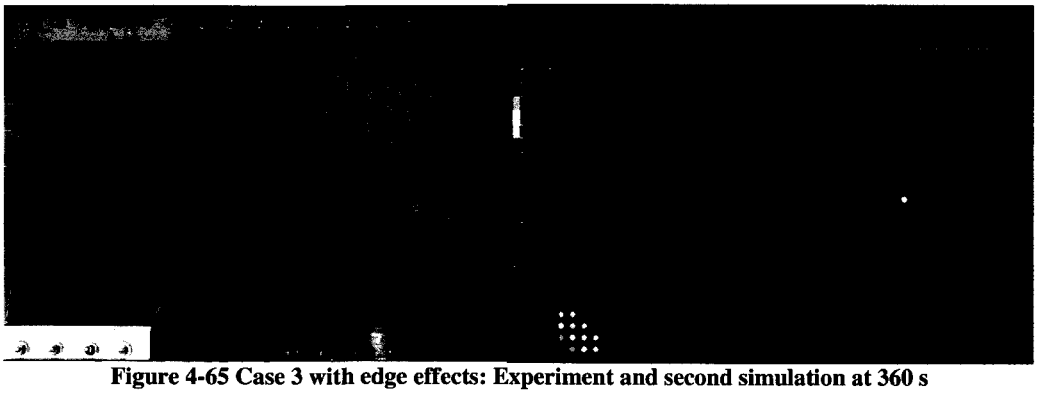

Figure 4-65 Case 3 with edge effects: Experiment and second simulation at 360 s

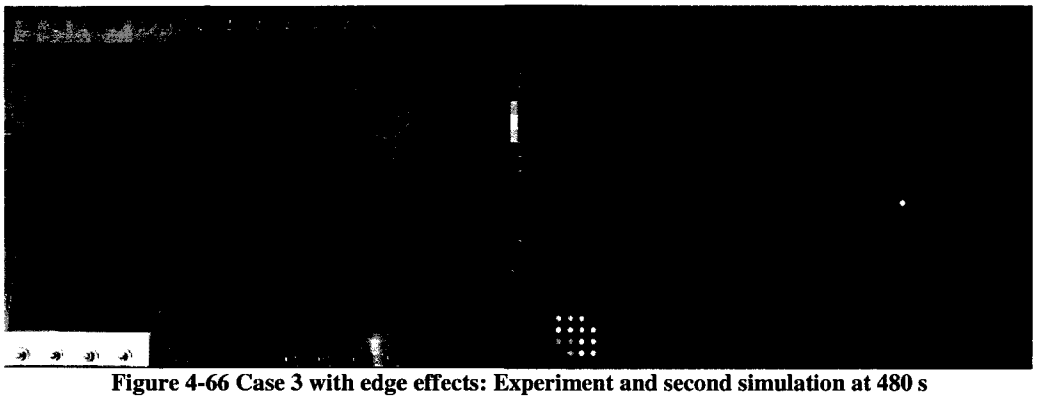

Figure 4-66 Case 3 with edge effects: Experiment and second simulation at 480 s

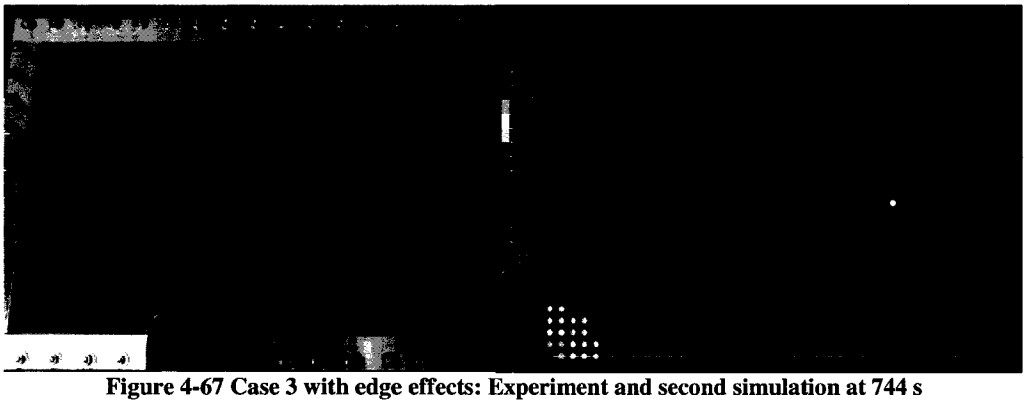

Figure 4-67 Case 3 with edge effects: Experiment and second simulation at 744 s

The second simulation showed much improved accuracy in fill time as well as flow front shape. A particularly strong edge effect was shown at the east wall, as seen in Figure 4-65 and Figure 4-66. This could have been more closely simulated had the permeability was increased beyond $7.7\times10^{-10}\,m^2$. To validate this, a third test was done with adjusted permeability values along the east wall. The values were increased to $1.8\times10^{-9}\,m^2$ which is equivalent to having a flow channel of 0.15 *mm*.

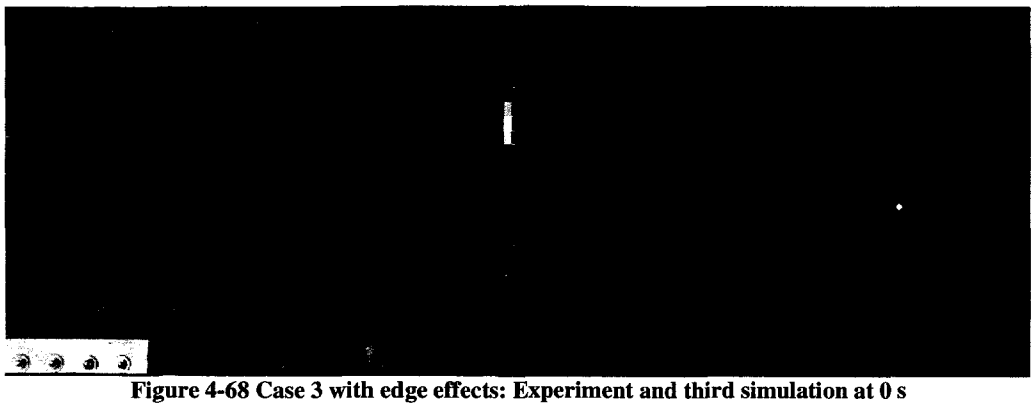

Figure 4-68 Case 3 with edge effects: Experiment and third simulation at 0 s

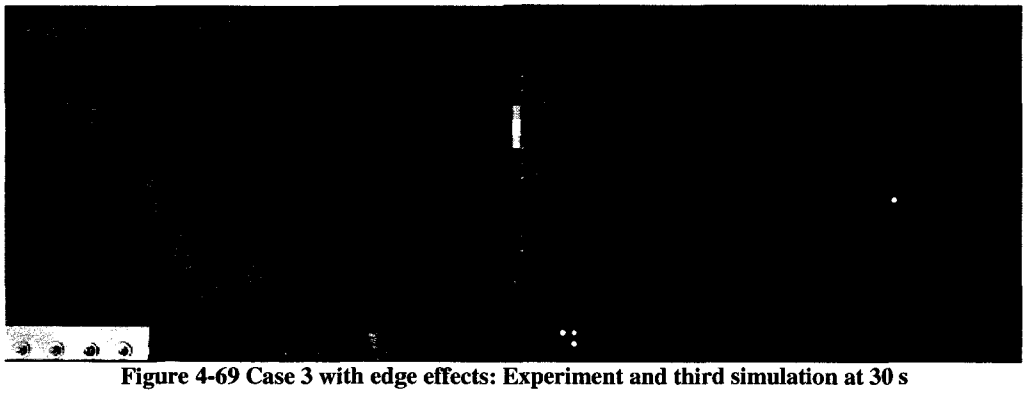

Figure 4-69 Case 3 with edge effects: Experiment and third simulation at 30 s

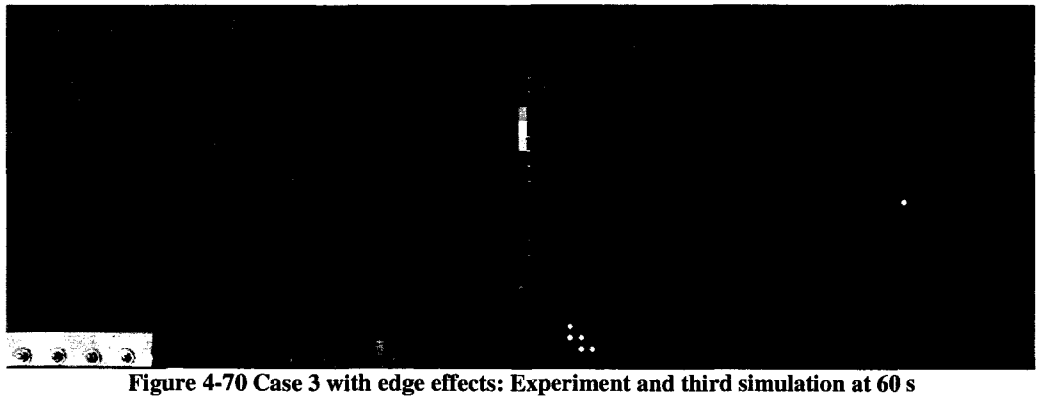

Figure 4-70 Case 3 with edge effects: Experiment and third simulation at 60 s

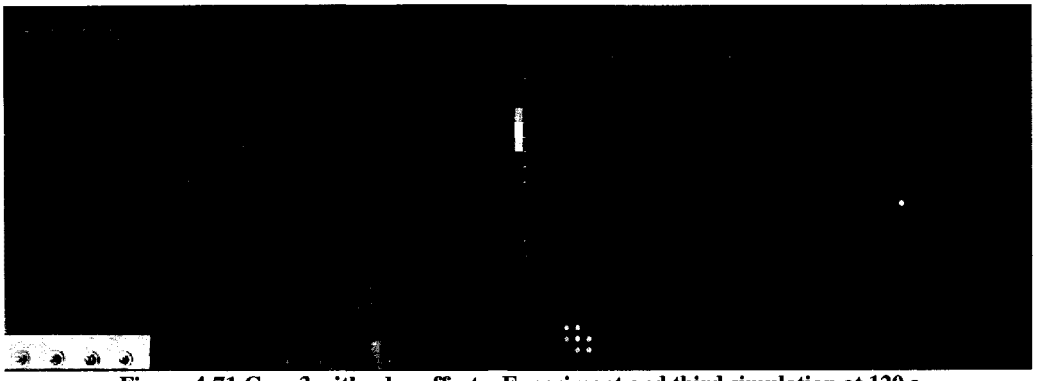

Figure 4-71 Case 3 with edge effects: Experiment and third simulation at 120 s

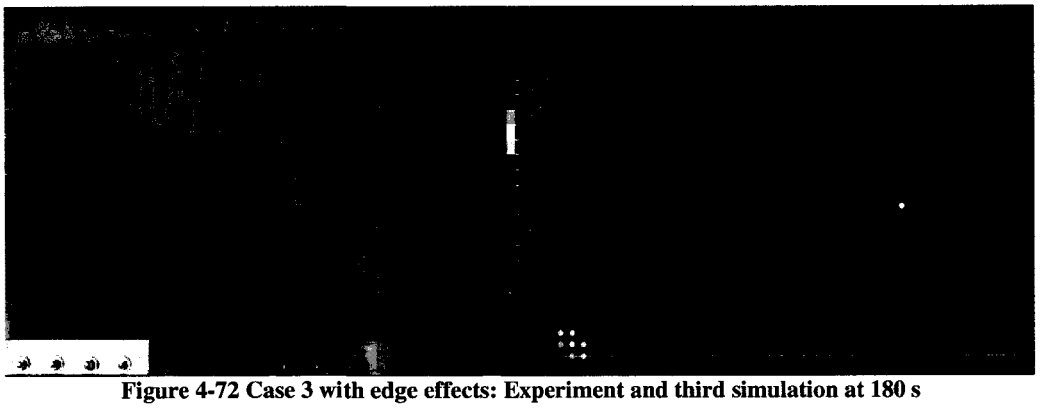

Figure 4-72 Case 3 with edge effects: Experiment and third simulation at 180 s

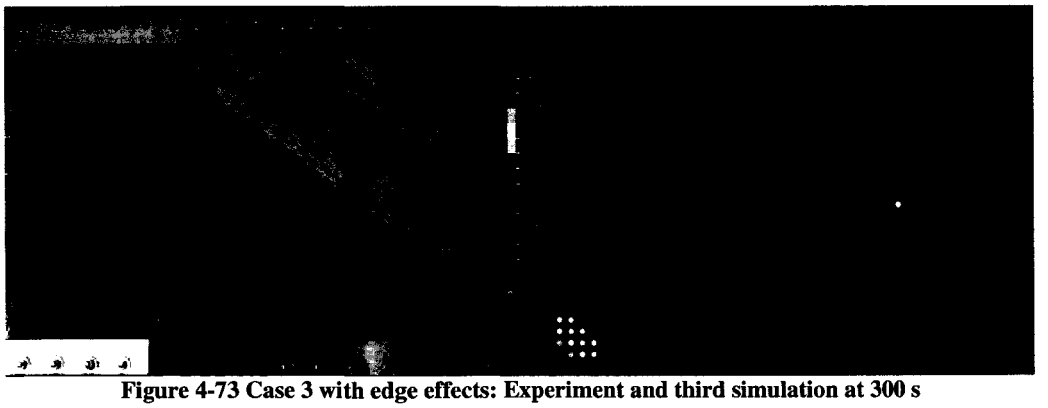

Figure 4-73 Case 3 with edge effects: Experiment and third simulation at 300 s

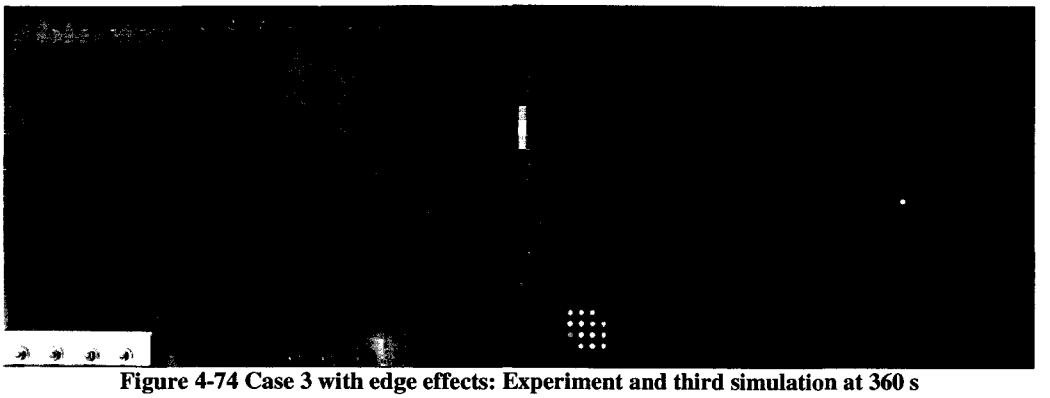

Figure 4-74 Case 3 with edge effects: Experiment and third simulation at 360 s

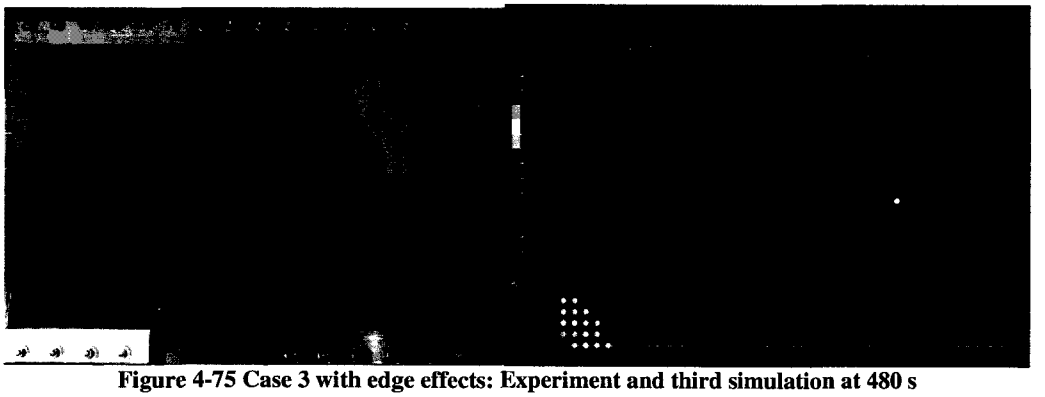

Figure 4-75 Case 3 with edge effects: Experiment and third simulation at 480 s

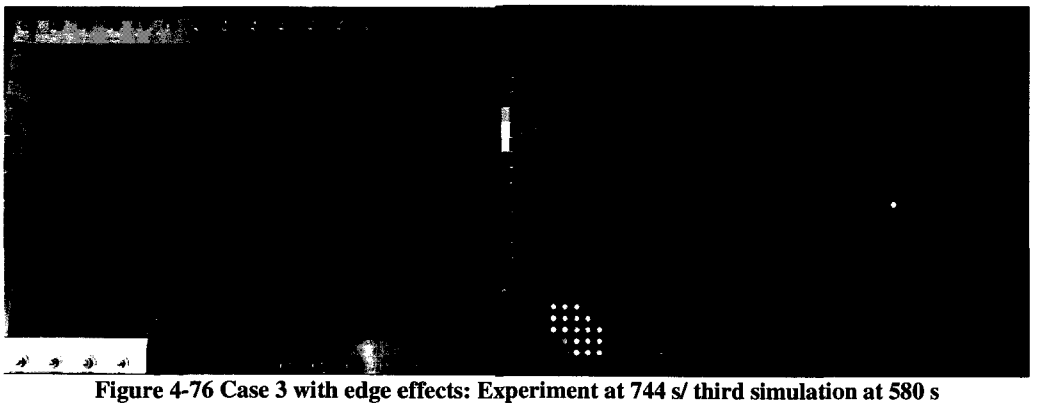

Figure 4-76 Case 3 with edge effects: Experiment at 744 s/ third simulation at 580 s

Due to the adjustment made on east wall's permeability, the results were improved greatly as shown in Figure 4-93. The overall flow pattern of curvature around the edges were also improved and closely simulated. Only downfall to this approach is the significant decrease in fill time during simulation whereas the experiment tends to lag during the last stage of infusion process.

4.1.4 Case 4: 4 layers of random mat with double inlet at ports 13, 16

In practical applications, RTM infusion processes usually involves multiple inlet ports. Multiple inlet ports enable optimization of the fill time as the resin travels more effectively to the unsaturated regions than it would from a single inlet. Thus, it is important to know how the flow front progresses when multiple inlet ports are used instead of one inlet port, and to have the capability of simulating this.

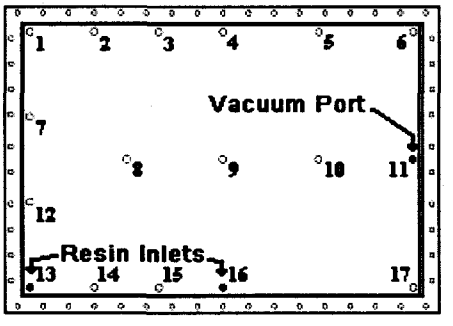

Figure 4-77 Case 4 configuration

With two inlets at ports 13 and 16, the fill time is expected to be much less than seen in cases featuring a single inlet. Port 16 should lead to a half-circle shaped flow front

whereas port 13 should create a quarter circle shaped flow front – eventually these would merge and progress further together. The permeability value used in the first simulation devoid of edge effects was $5.0\times10^{-10}\ m^2$.

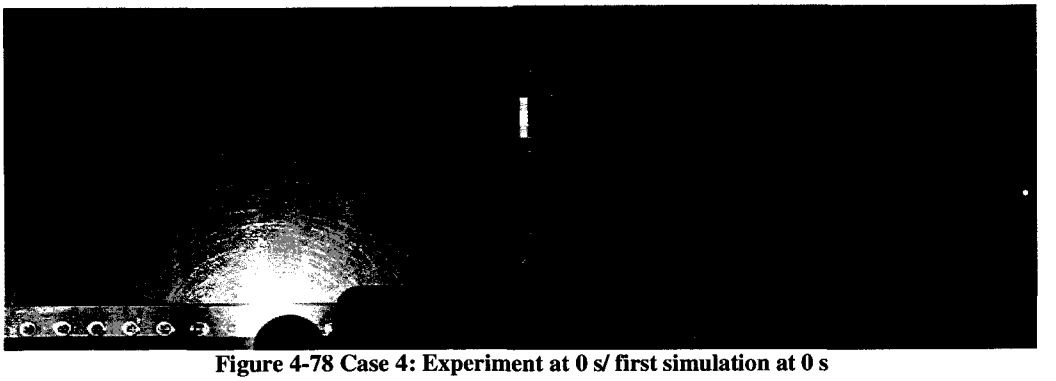

Figure 4-78 Case 4: Experiment at 0 s/ first simulation at 0 s

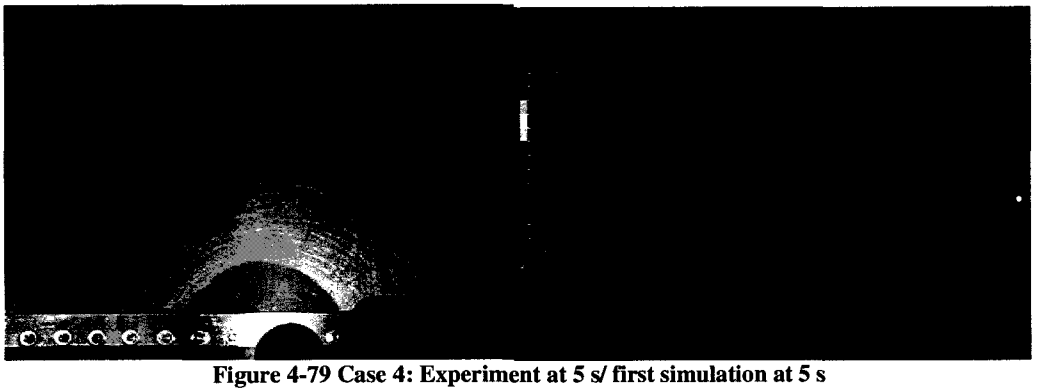

Figure 4-79 Case 4: Experiment at 5 s/ first simulation at 5 s

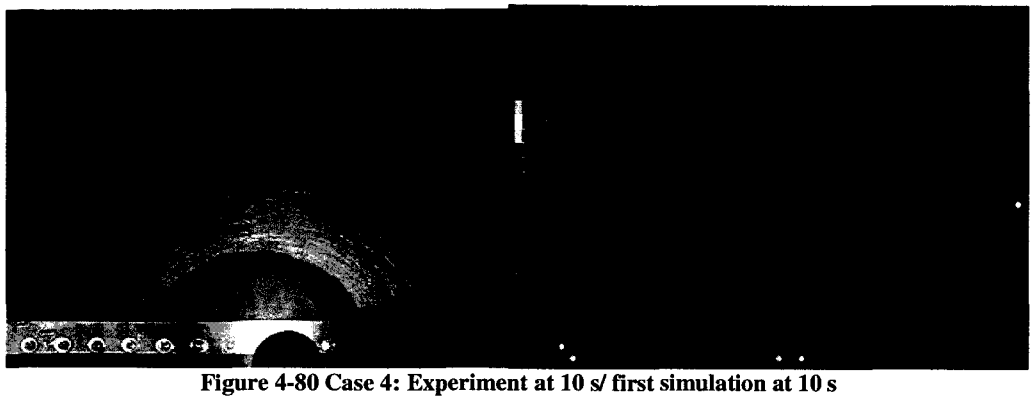

Figure 4-80 Case 4: Experiment at 10 s/ first simulation at 10 s

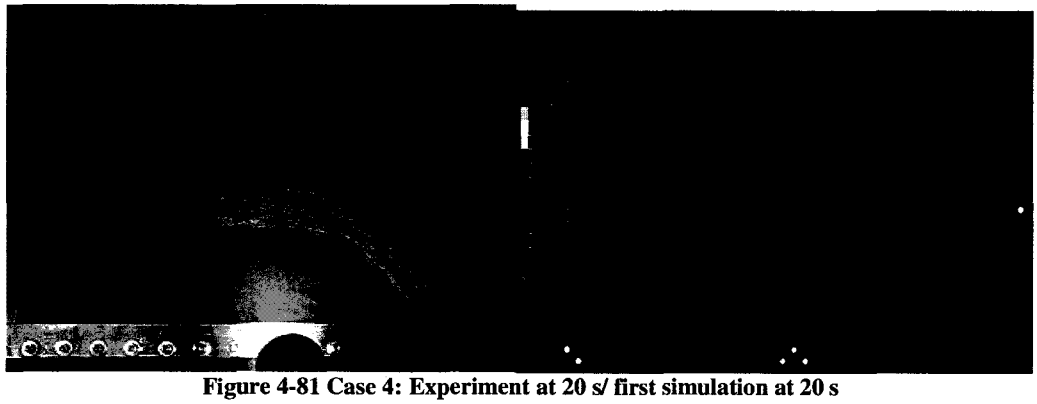

Figure 4-81 Case 4: Experiment at 20 s/ first simulation at 20 s

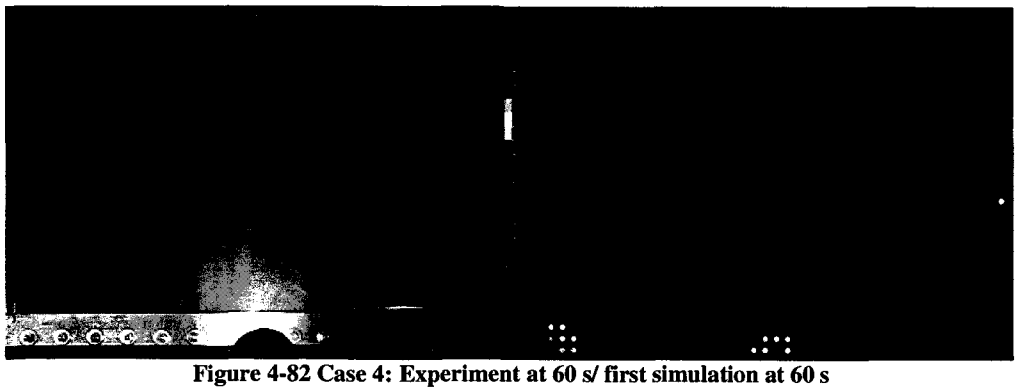

Figure 4-82 Case 4: Experiment at 60 s/ first simulation at 60 s

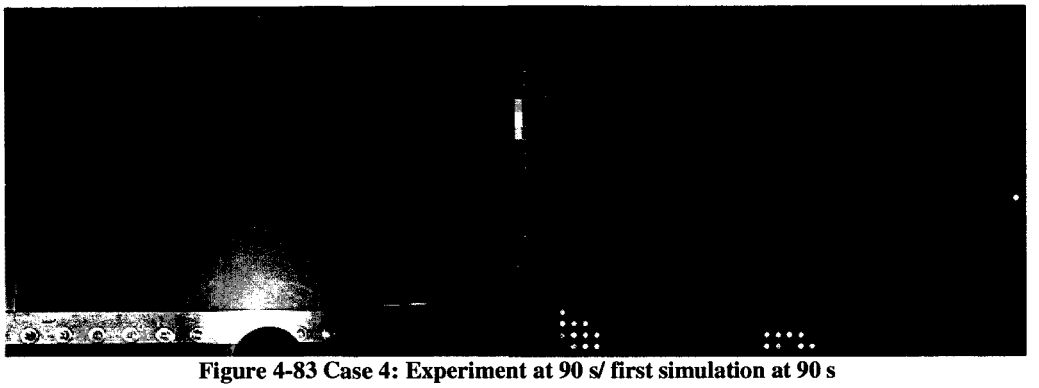

Figure 4-83 Case 4: Experiment at 90 s/ first simulation at 90 s

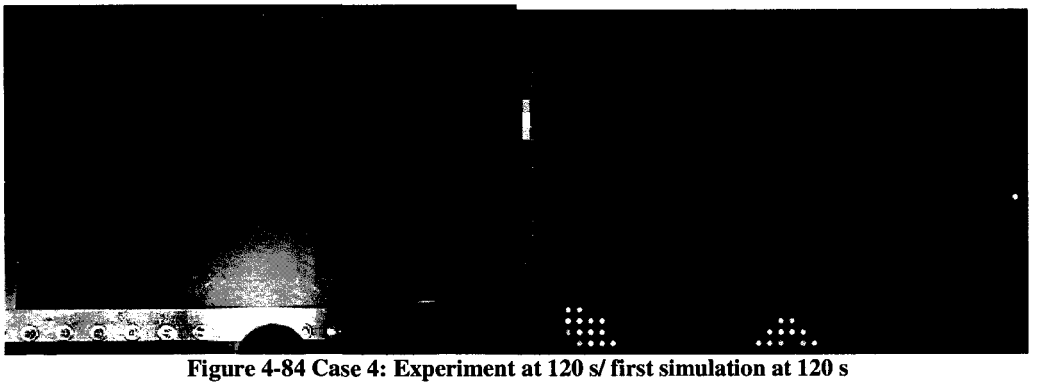

Figure 4-84 Case 4: Experiment at 120 s/ first simulation at 120 s

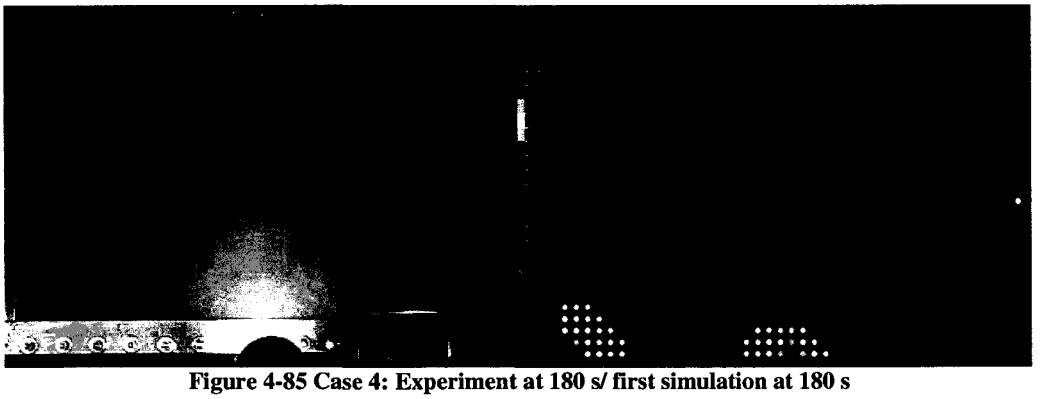

Figure 4-85 Case 4: Experiment at 180 s/ first simulation at 180 s

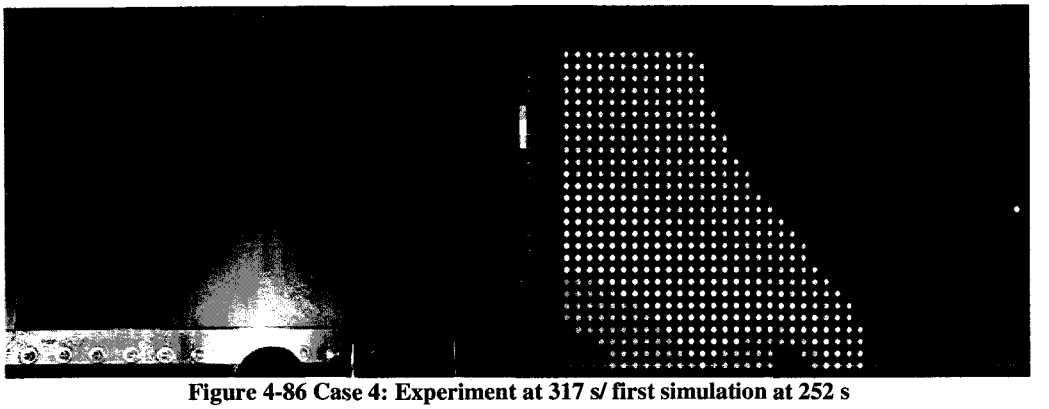

Figure 4-86 Case 4: Experiment at 317 s/ first simulation at 252 s

As expected, the flow front started out as a quarter circle at port 13 and a half circle at port 16 then they eventually joined together to form a bigger flow front. Some edge effects were seen in Figure 4-82 and Figure 4-83, as these show the accelerated flow particularly along the west and north walls. Thus, a second simulation was done with the permeability increased to $1.1\times10^{-9}\ m^2$ which is equivalent to having a flow channel of $0.115\ mm$ along the edges.

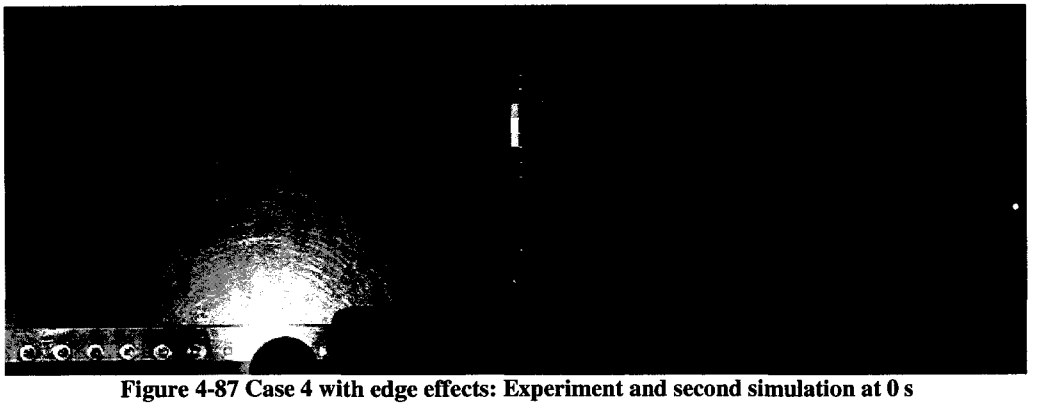

Figure 4-87 Case 4 with edge effects: Experiment and second simulation at 0 s

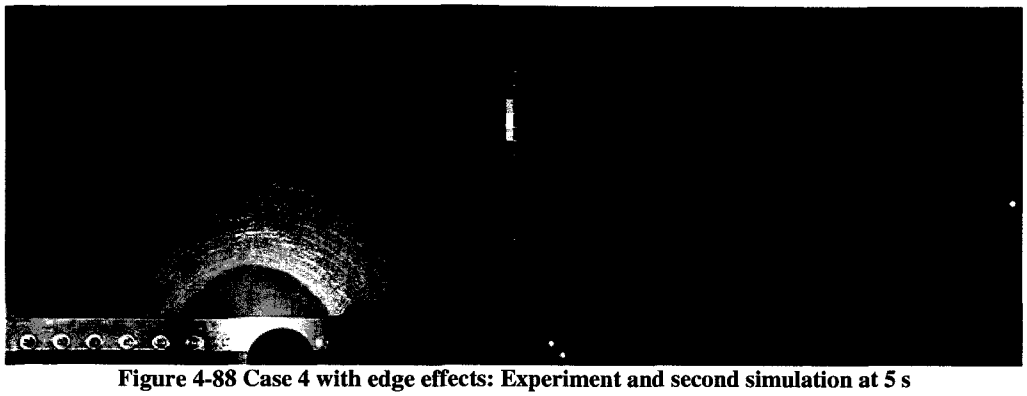

Figure 4-88 Case 4 with edge effects: Experiment and second simulation at 5 s

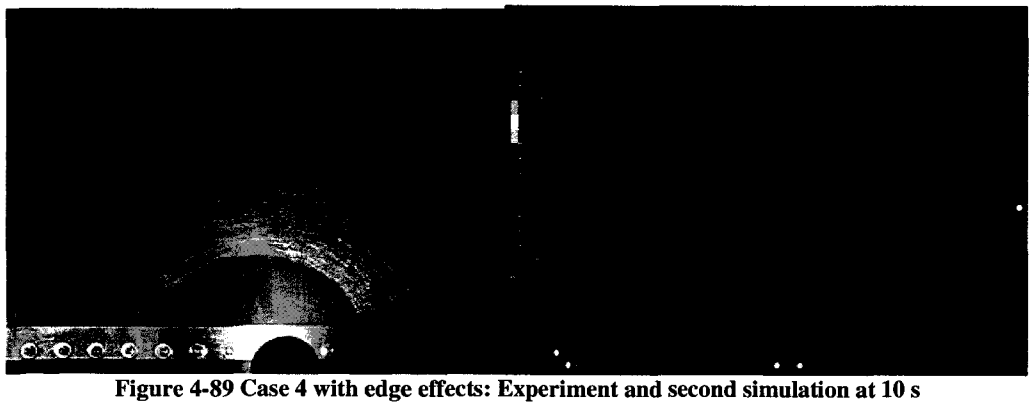

Figure 4-89 Case 4 with edge effects: Experiment and second simulation at 10 s

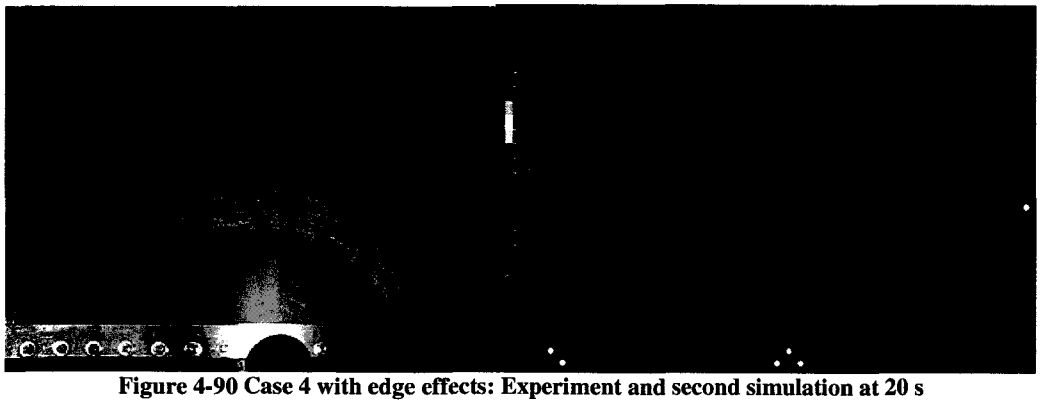

Figure 4-90 Case 4 with edge effects: Experiment and second simulation at 20 s

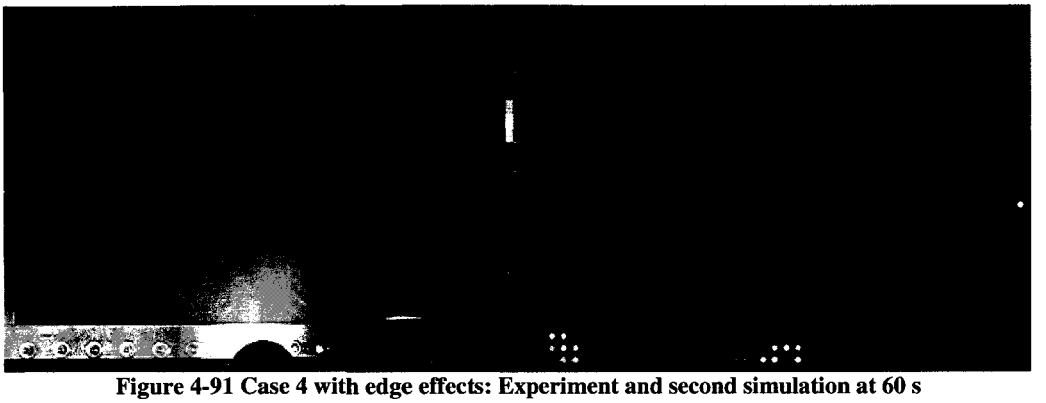

Figure 4-91 Case 4 with edge effects: Experiment and second simulation at 60 s

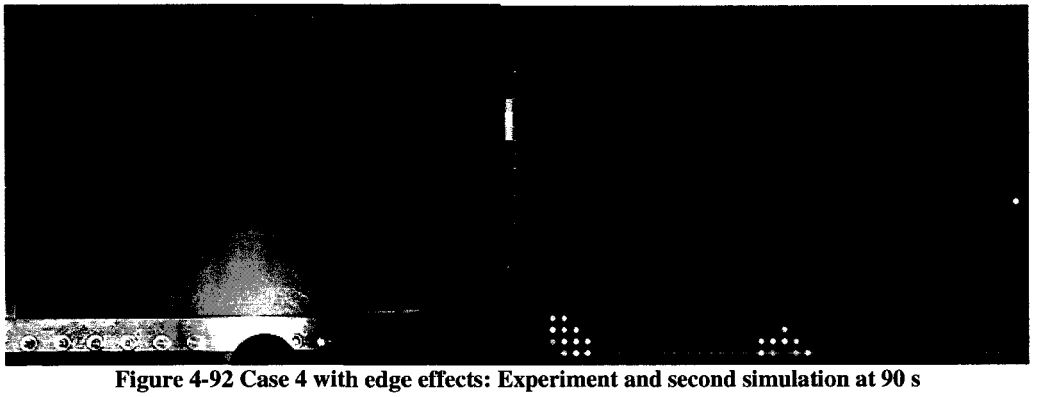

Figure 4-92 Case 4 with edge effects: Experiment and second simulation at 90 s

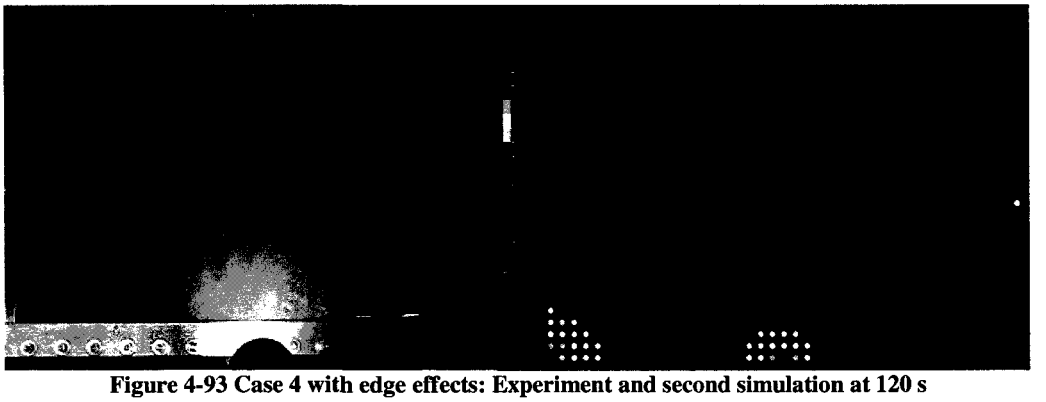

Figure 4-93 Case 4 with edge effects: Experiment and second simulation at 120 s

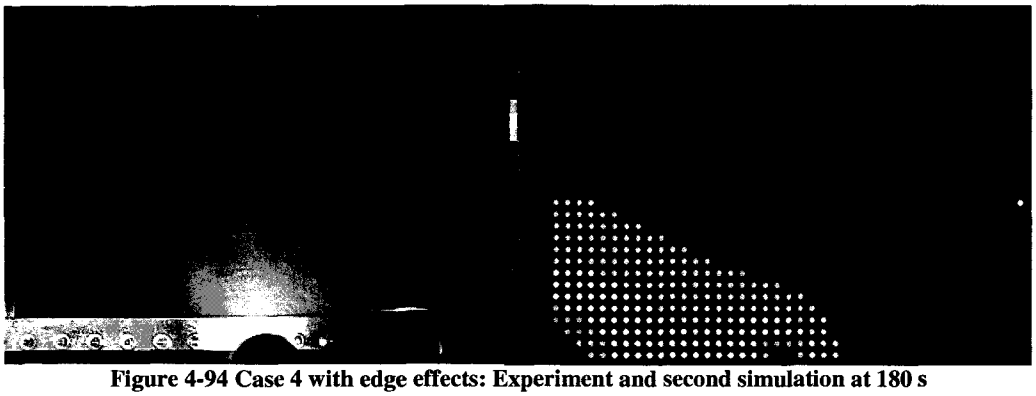

Figure 4-94 Case 4 with edge effects: Experiment and second simulation at 180 s

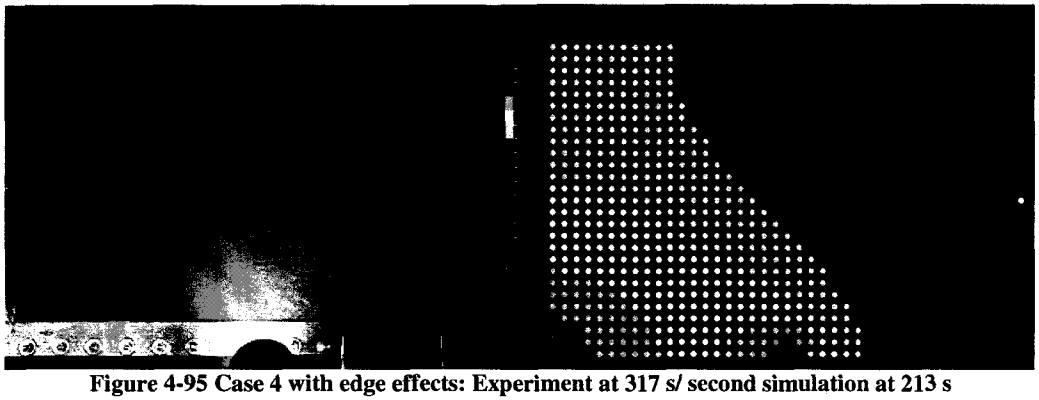

Figure 4-95 Case 4 with edge effects: Experiment at 317 s/ second simulation at 213 s

The overall experimental and simulated flow patterns were very similar after the adjustments. By knowing the permeability value of the fabric as well as acceptable values around the walls for edge effect, a very accurate simulation can be obtained.

4.1.5 Case 5: 4 layers of random mat with asymmetric obstacles

One of the best features of RTM is the capability of impregnating complex mould shapes. Thus, it is essential to test the case of a mould with irregular domain shape which

consists of many edges and corners to ensure that the progress of resin in the cavity can be simulated.

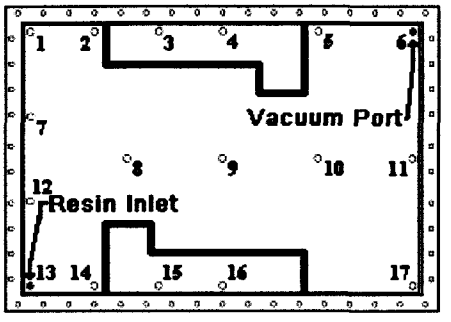

Figure 4-96 Case 5 configuration

The mirrored 'L' inserts on the north and south walls – indicated by thick black lines – represent the inserted solids within the cavity. The removable walls were cut out from strips of flexible sealing tape which are impermeable. The walls were laid and sealed tightly with silicone adhesive. The resin was drawn in from port 13 and vacuumed out from port 6. This insured the impregnation of the entire cavity before resin reached the vacuum port. The permeability value used for this particular case was $5.5\times10^{-10}\,m^2$.

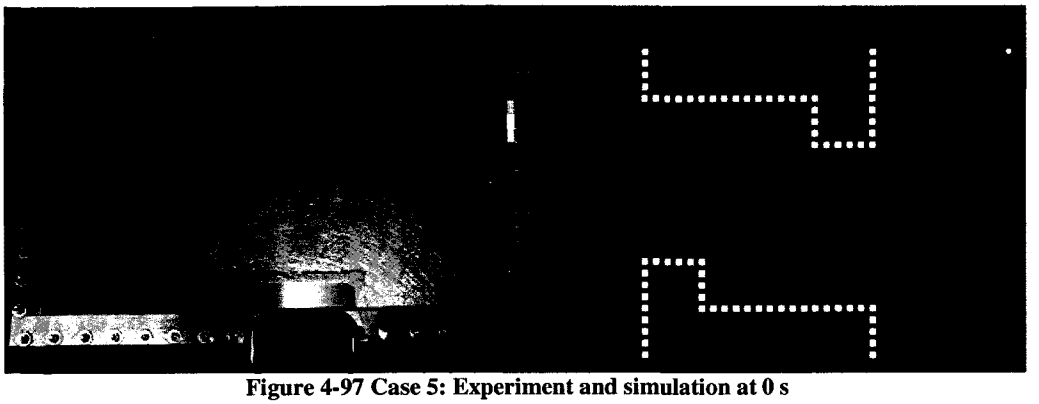

Figure 4-97 Case 5: Experiment and simulation at 0 s

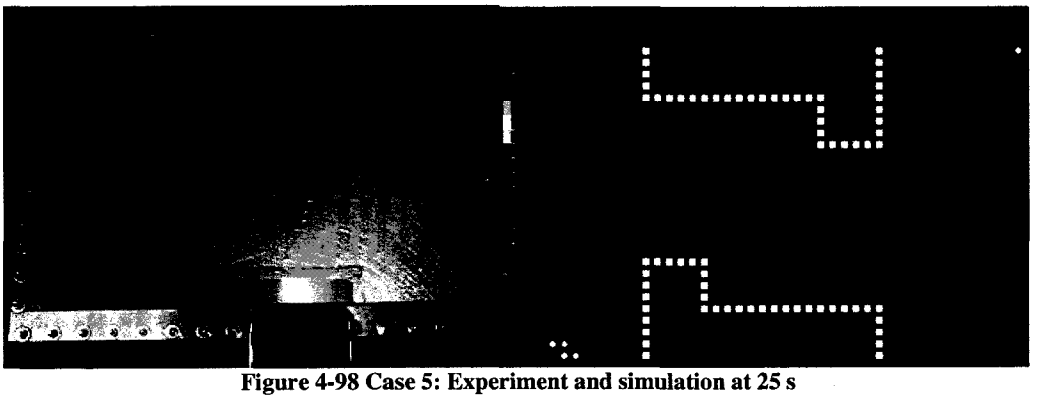

Figure 4-98 Case 5: Experiment and simulation at 25 s

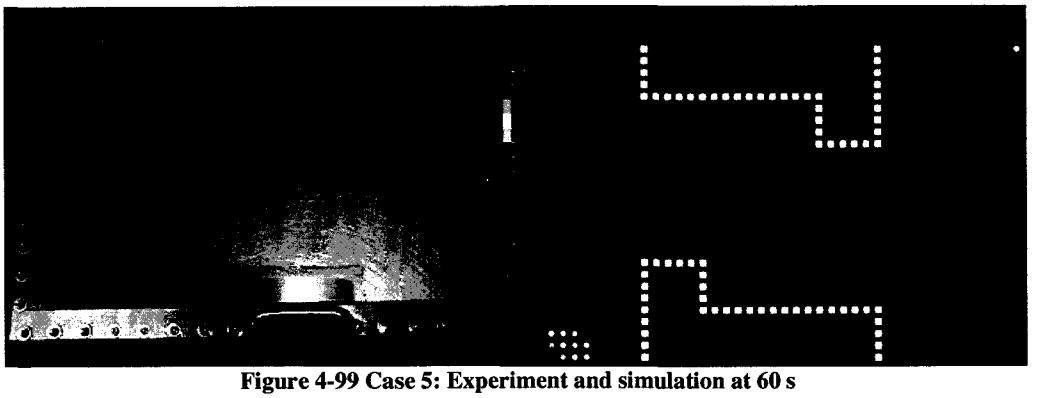

Figure 4-99 Case 5: Experiment and simulation at 60 s

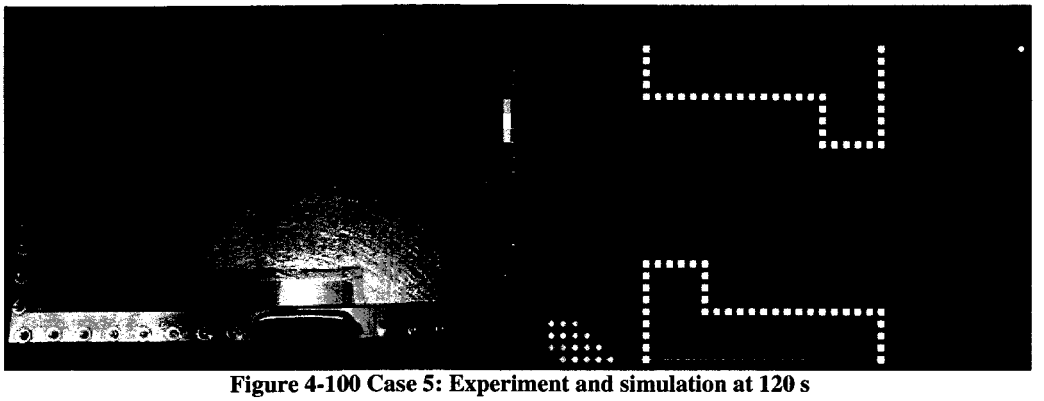

Figure 4-100 Case 5: Experiment and simulation at 120 s

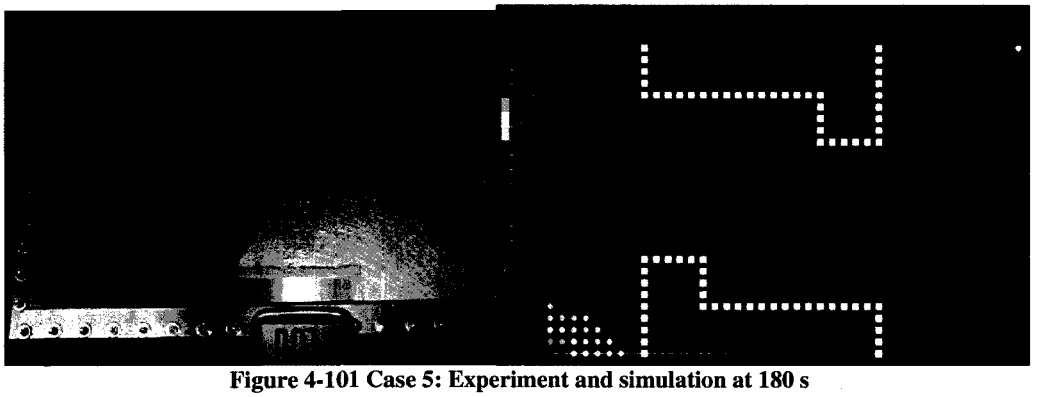

Figure 4-101 Case 5: Experiment and simulation at 180 s

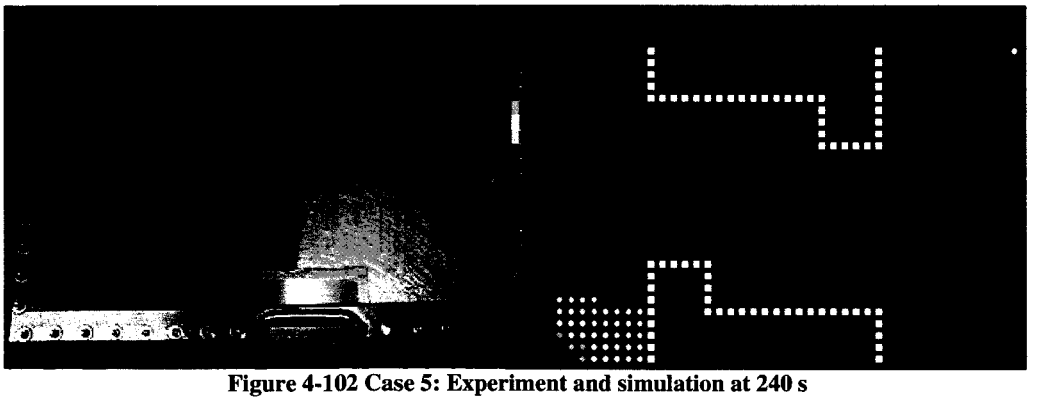

Figure 4-102 Case 5: Experiment and simulation at 240 s

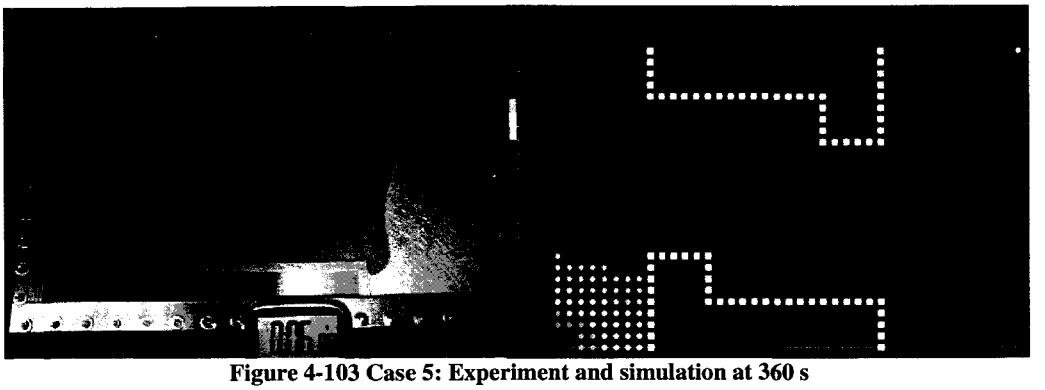

Figure 4-103 Case 5: Experiment and simulation at 360 s

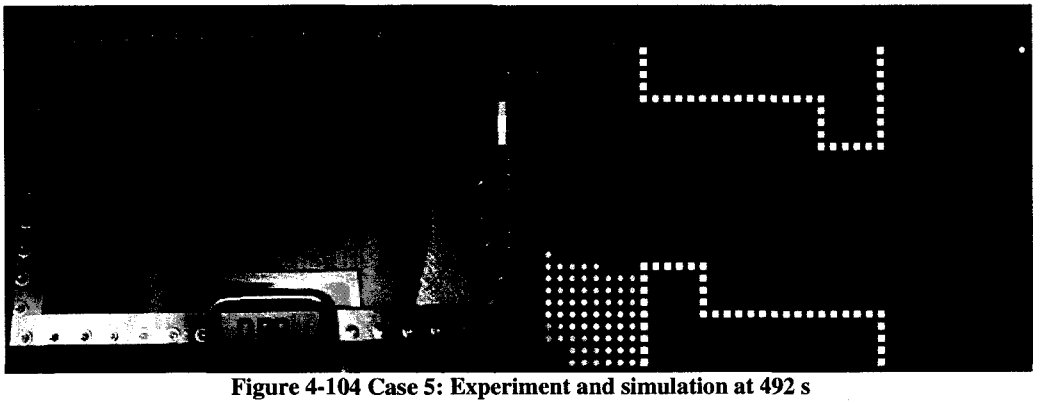

Figure 4-104 Case 5: Experiment and simulation at 492 s

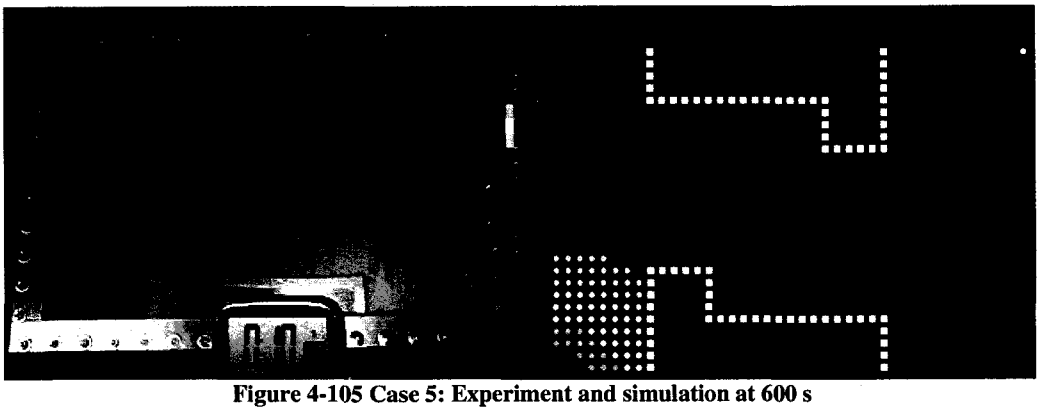

Figure 4-105 Case 5: Experiment and simulation at 600 s

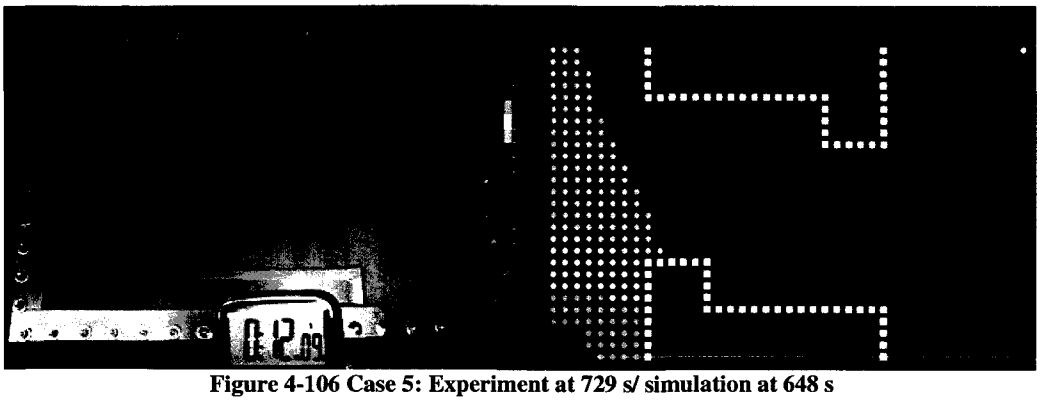

Figure 4-106 Case 5: Experiment at 729 s/ simulation at 648 s

As seen in Figure 4-99, some edge effect has allowed the flow to progress faster up the west cavity wall. However, no visible edge effect was observed after that, and especially not along the polymer walls. The fluid reached every corner of the cavity before it arrived at the vacuum port for both the experiment and simulation, as seen in Figure 4-105. A second simulation was not done in this particular case since the experiment and simulation matched well apart from the visible edge effect on west wall.

4.1.6 Case 6: 4 layers of random mat with cut-out section in 2 central layers

This unique case deals with 2 regularly cut rectangular layers and 2 layers with a cut-out rectangular section in the middle so that they resemble a 'C' shape. In composite manufacturing, it is rare to have a uniform permeability in all zones. This test dealt with varying permeability during infusion process which is very common in many industrial applications. As for the simulation, different permeability values were entered in the cut out domain. The 2 cut-out layers are inserted in between the 2 regular layers.

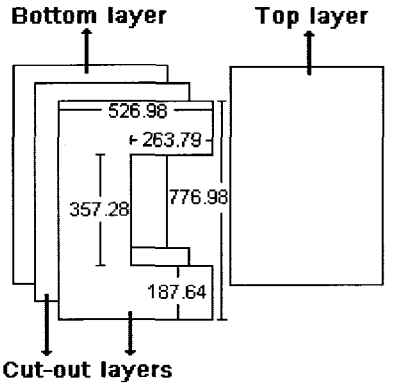

Figure 4-107 Cut-out layer dimensions (*mm*)

The section with only 2 layers would have a higher permeability compared to the rest of the preform, as the fluid would only be required to flow through 2 layers of fabric instead of 4.

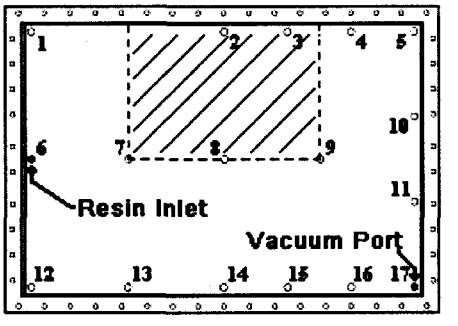

Figure 4-108 Case 6 configuration

The resin was injected from port 6 and it was vacuumed from port 17. The shaded part of Figure 4-108 represents the cut-out section where only 2 layers were present. First

simulation was done with no edge effects implemented. The permeability value used for this run was $4.0\times10^{-10}\,m^2$ for the 4 layer section, and $1.2\times10^{-9}\,m^2$ for the 2 layer section.

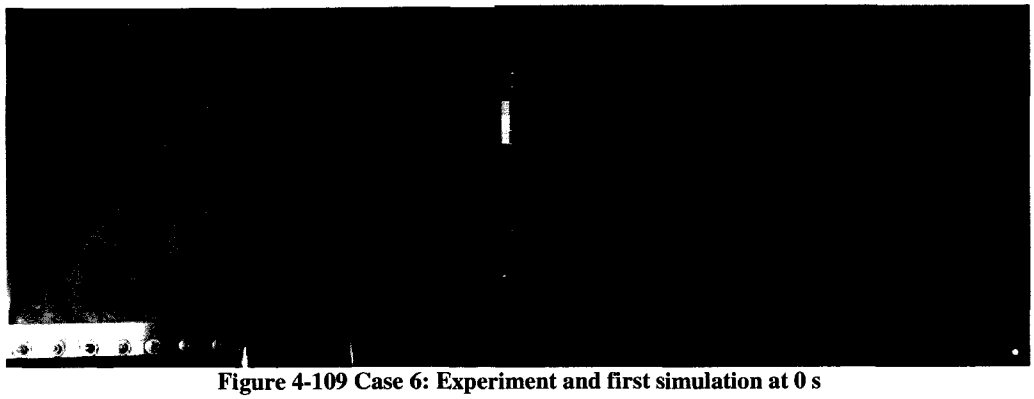

Figure 4-109 Case 6: Experiment and first simulation at 0 s

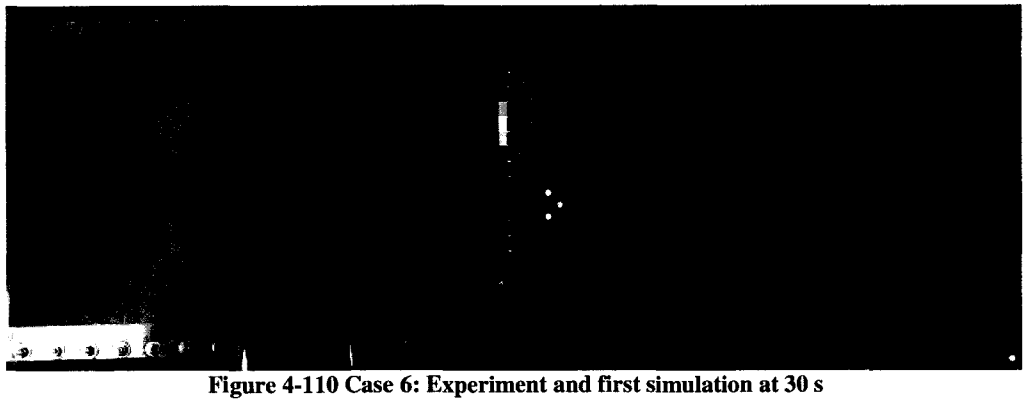

Figure 4-110 Case 6: Experiment and first simulation at 30 s

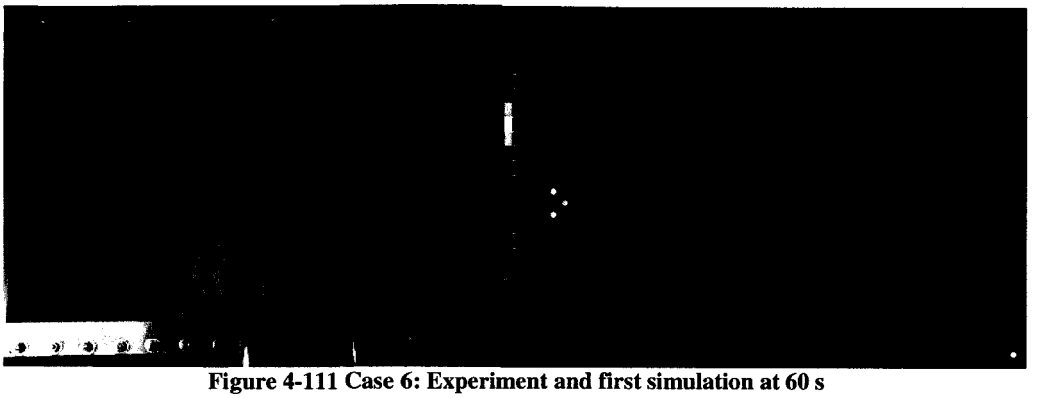

Figure 4-111 Case 6: Experiment and first simulation at 60 s

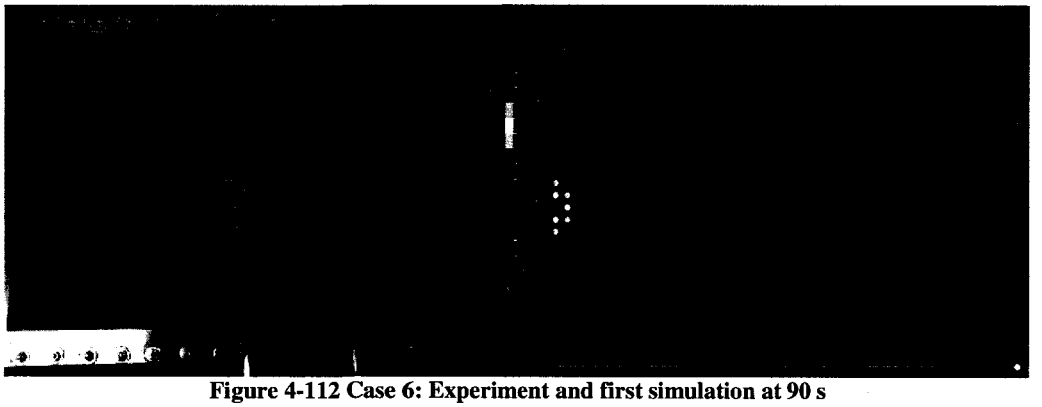

Figure 4-112 Case 6: Experiment and first simulation at 90 s

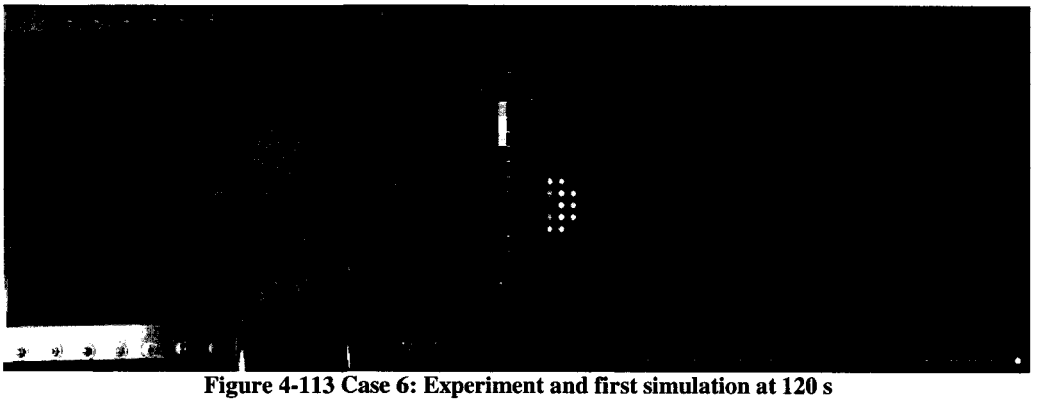

Figure 4-113 Case 6: Experiment and first simulation at 120 s

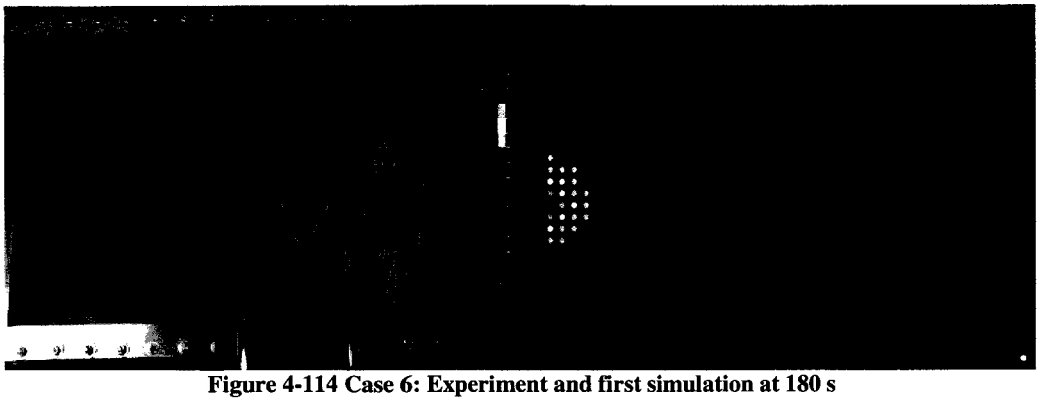

Figure 4-114 Case 6: Experiment and first simulation at 180 s

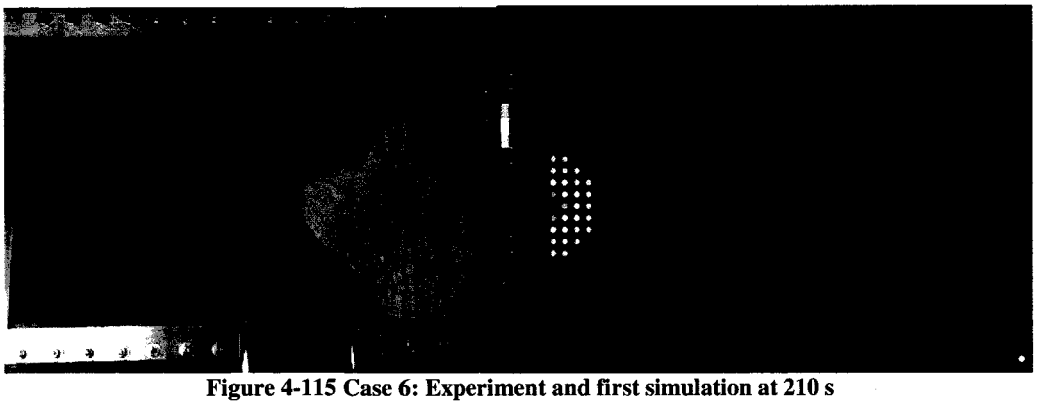

Figure 4-115 Case 6: Experiment and first simulation at 210 s

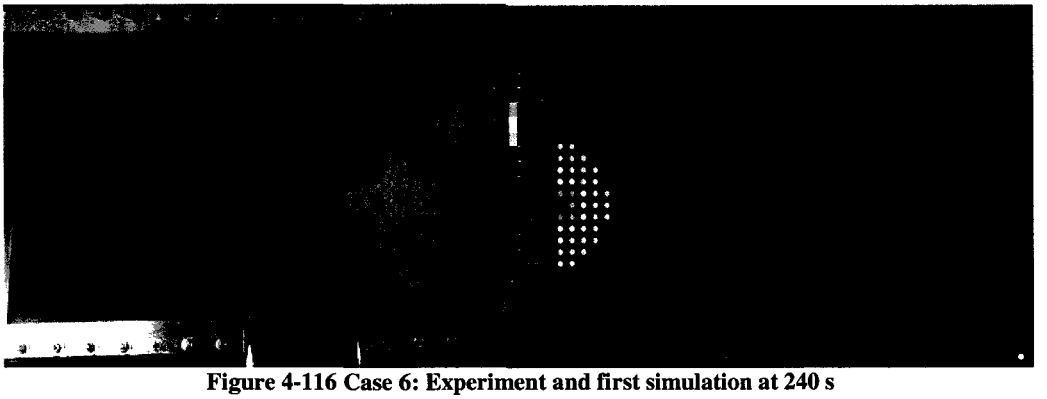

Figure 4-116 Case 6: Experiment and first simulation at 240 s

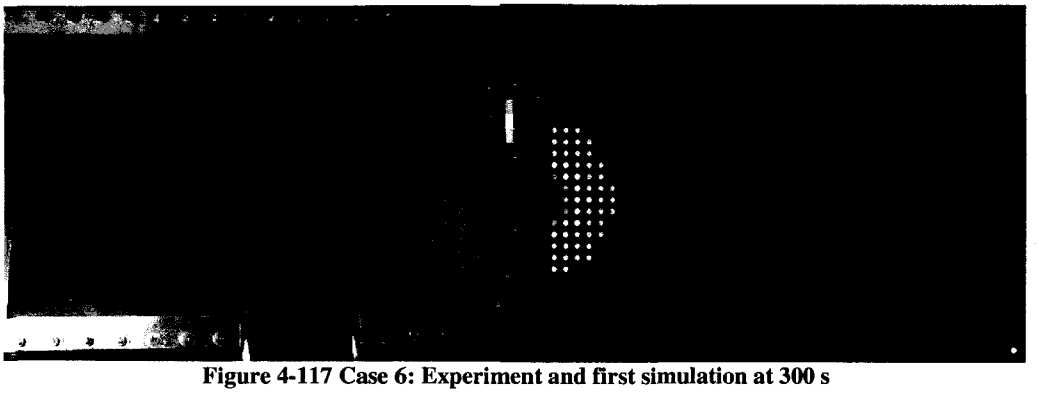

Figure 4-117 Case 6: Experiment and first simulation at 300 s

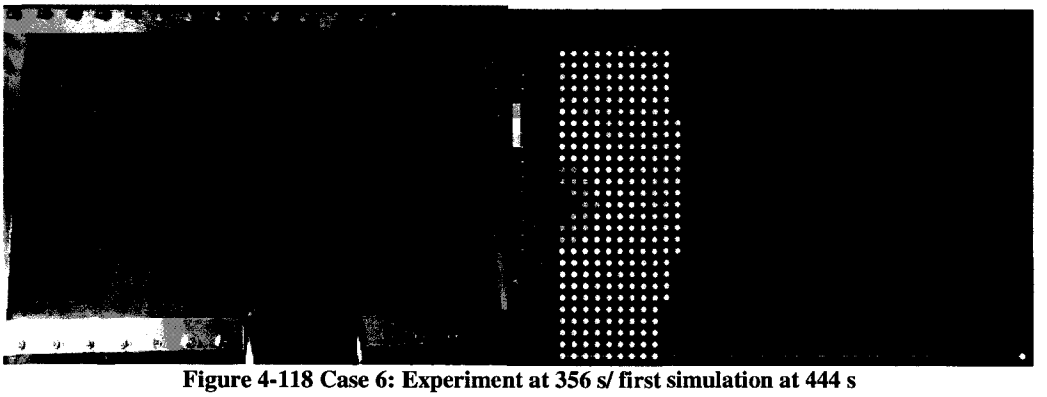

Figure 4-118 Case 6: Experiment at 356 s/ first simulation at 444 s

Once again the edge effect affected the experimental results. In this case, edge effects occur almost immediately from the onset of infusion as the flow along all four walls was accelerated significantly. This is particularly visible through Figure 4-112 to Figure 4-115. To improve the result, the edge effect was implemented within the simulation and ran again. The permeability was increased to $2.1\times10^{-9}\,m^2$ on all four walls which is equivalent to having a flow channel of 0.16 *mm*.

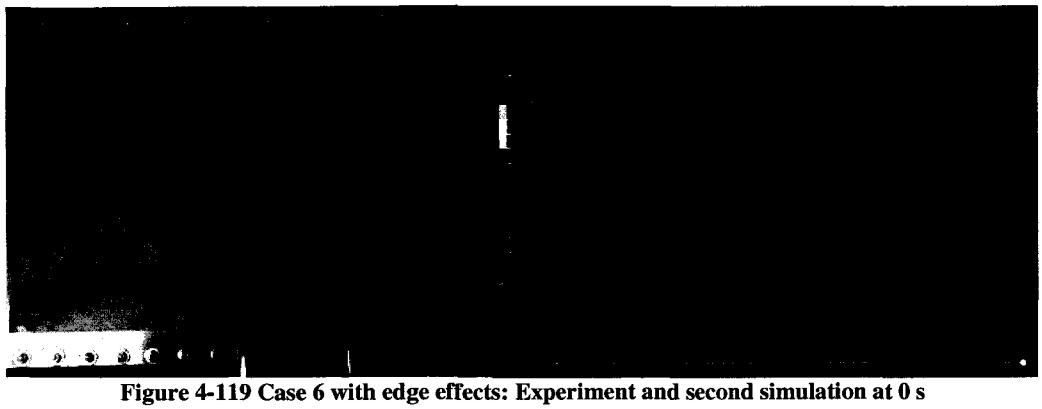

Figure 4-119 Case 6 with edge effects: Experiment and second simulation at 0 s

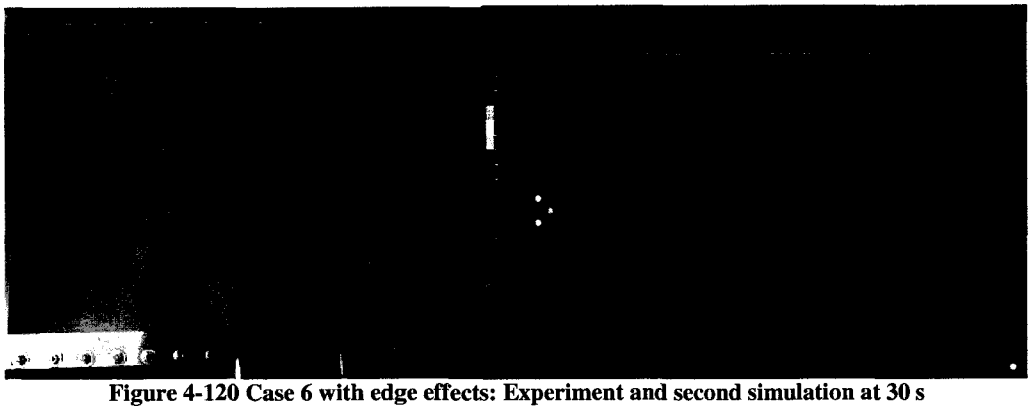

Figure 4-120 Case 6 with edge effects: Experiment and second simulation at 30 s

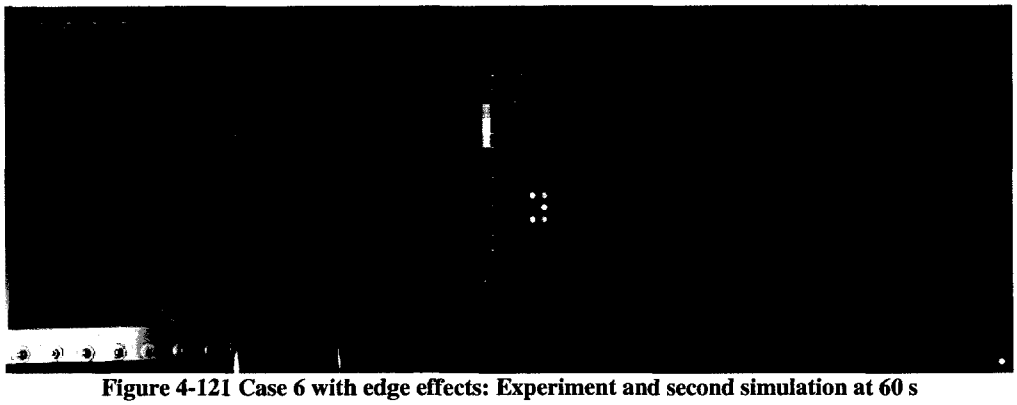

Figure 4-121 Case 6 with edge effects: Experiment and second simulation at 60 s

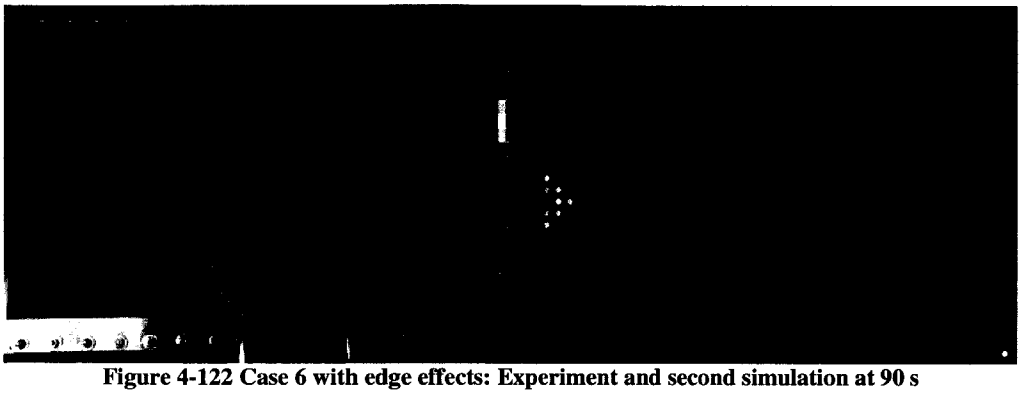

Figure 4-122 Case 6 with edge effects: Experiment and second simulation at 90 s

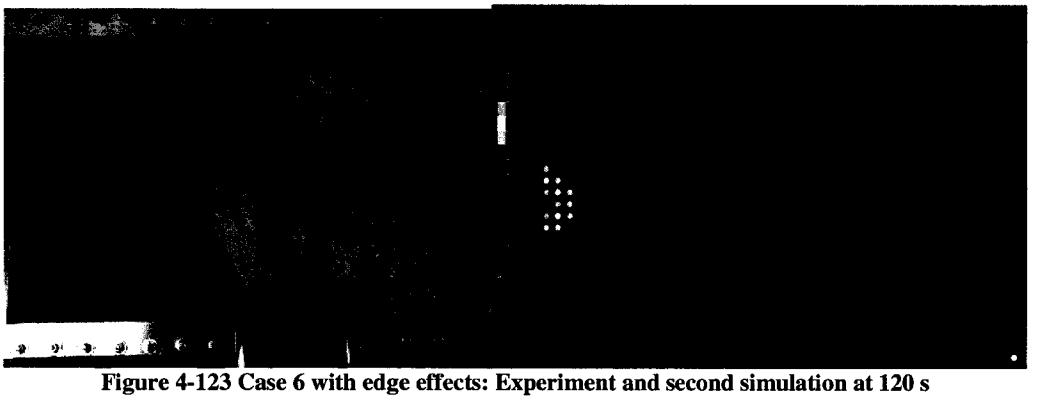

Figure 4-123 Case 6 with edge effects: Experiment and second simulation at 120 s

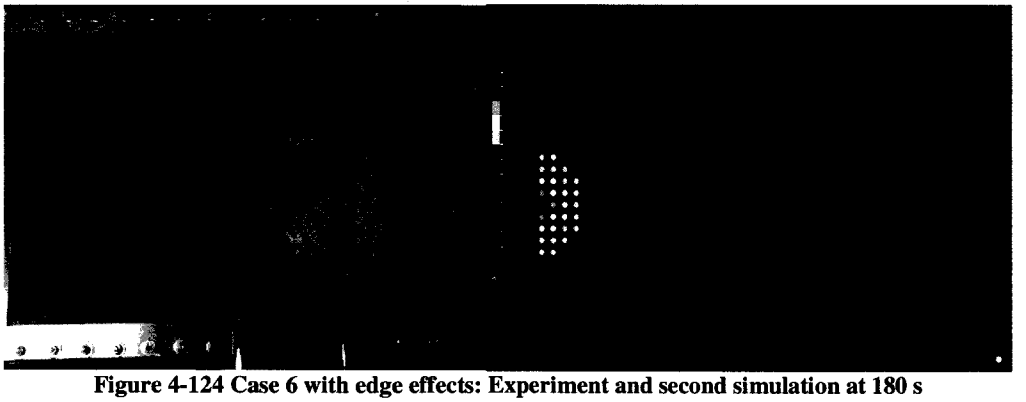

Figure 4-124 Case 6 with edge effects: Experiment and second simulation at 180 s

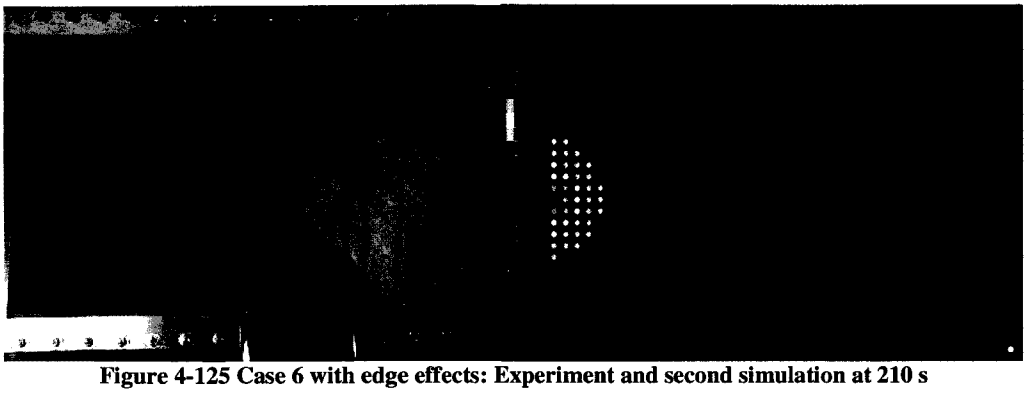

Figure 4-125 Case 6 with edge effects: Experiment and second simulation at 210 s

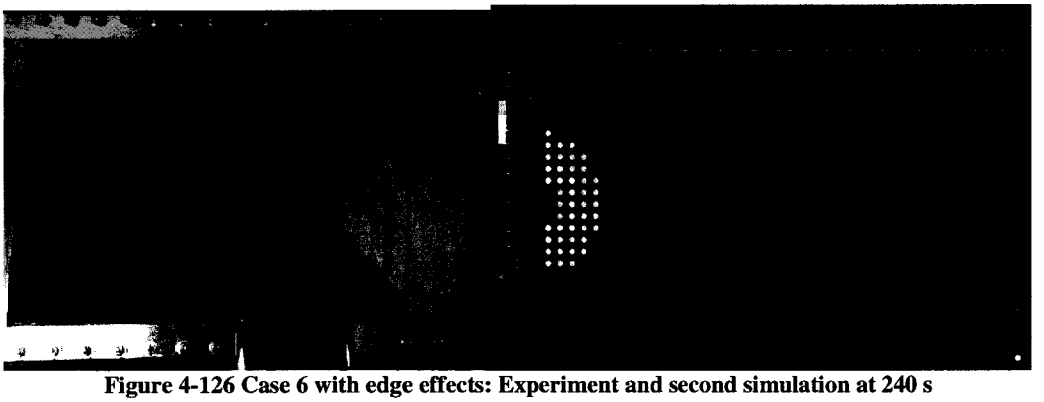

Figure 4-126 Case 6 with edge effects: Experiment and second simulation at 240 s

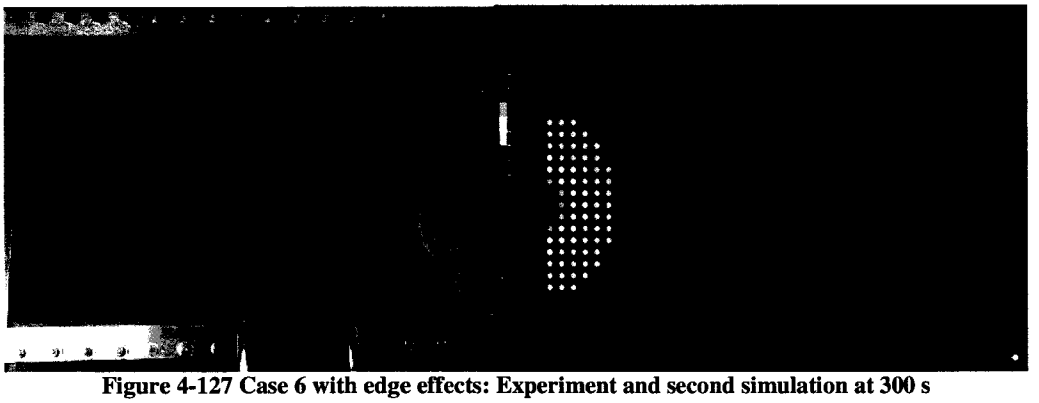

Figure 4-127 Case 6 with edge effects: Experiment and second simulation at 300 s

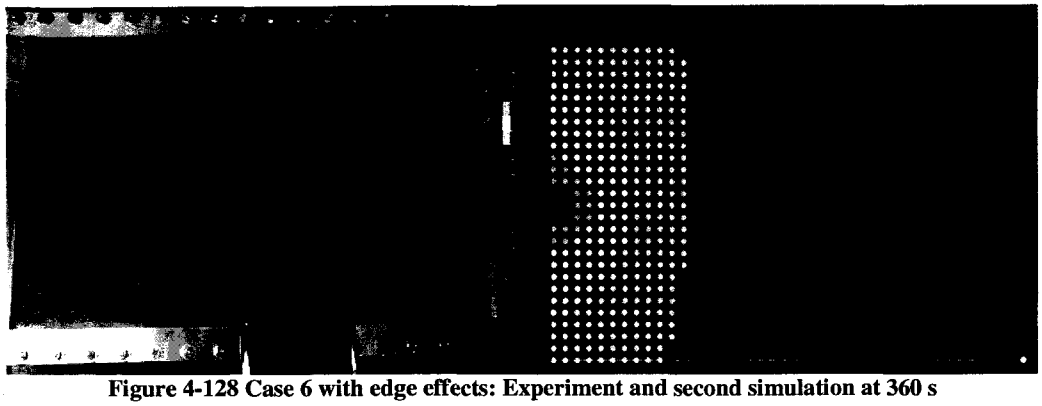

Figure 4-128 Case 6 with edge effects: Experiment and second simulation at 360 s

The overall simulated flow patterns have improved to resemble the experimental results better. However, the curvature of the flow in the central region could not be duplicated, as the discrepancy can be seen almost immediately from Figure 4-122 to Figure 4-127. This can be explained by the edge effect at the edge of the 4-to-2 layer change.

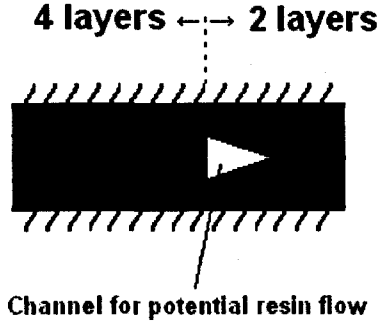

Figure 4-129 Channel created at the transition of layers

As shown in Figure 4-129, a gap is created at the transition between 4 layers and 2 layers due to the nature of the fabric. Such gap would act as a preferential flow path of resin.

Therefore a third test was done trying to simulate this effect. The permeability along the edges was increased to $1.9\times10^{-9}\ m^2$ which is equivalent to having a flow channel of 0.15 *mm*.

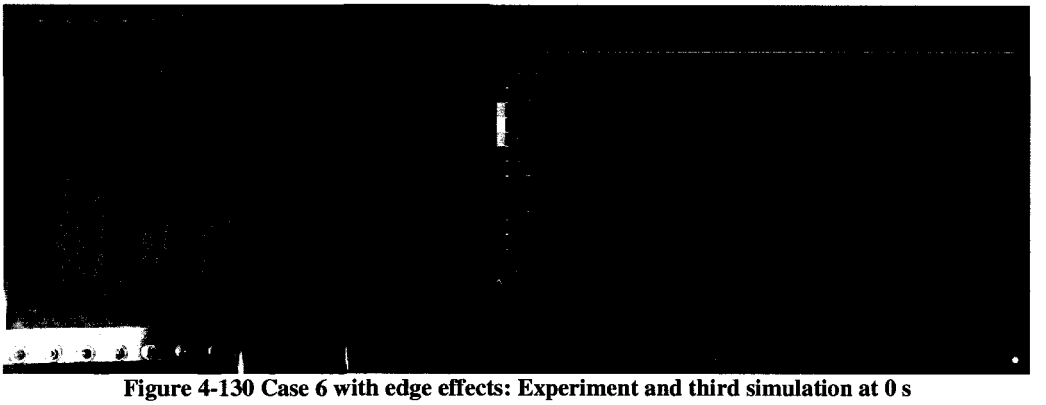

Figure 4-130 Case 6 with edge effects: Experiment and third simulation at 0 s

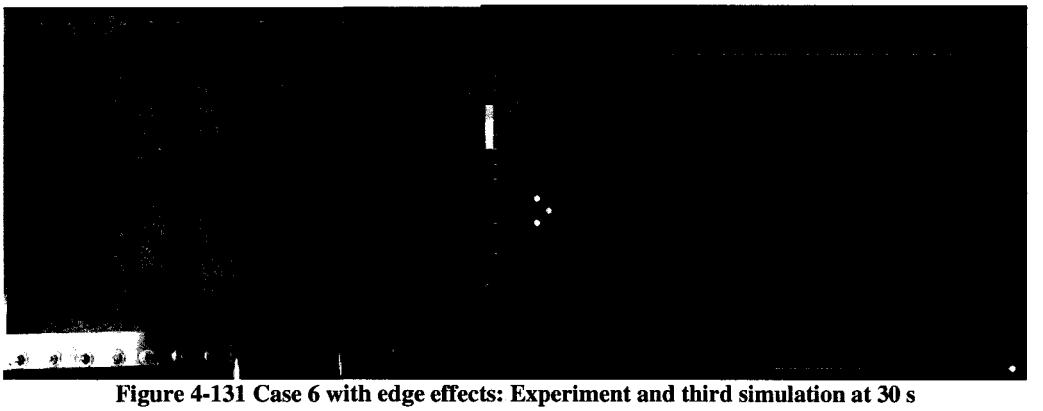

Figure 4-131 Case 6 with edge effects: Experiment and third simulation at 30 s

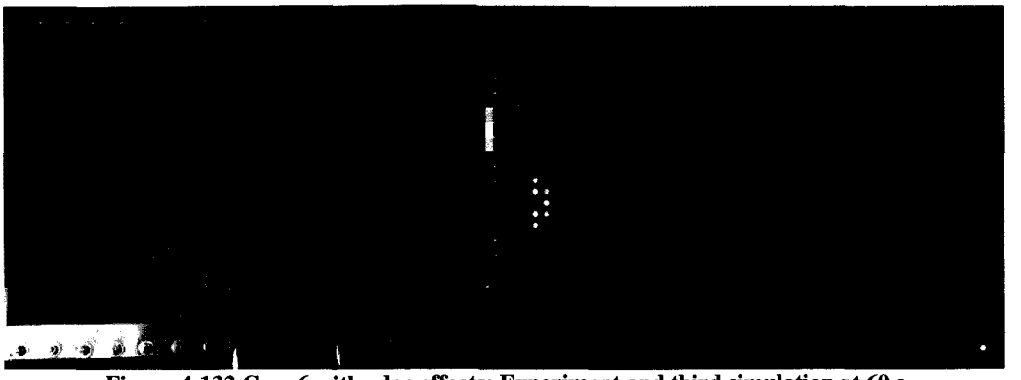

Figure 4-132 Case 6 with edge effects: Experiment and third simulation at 60 s

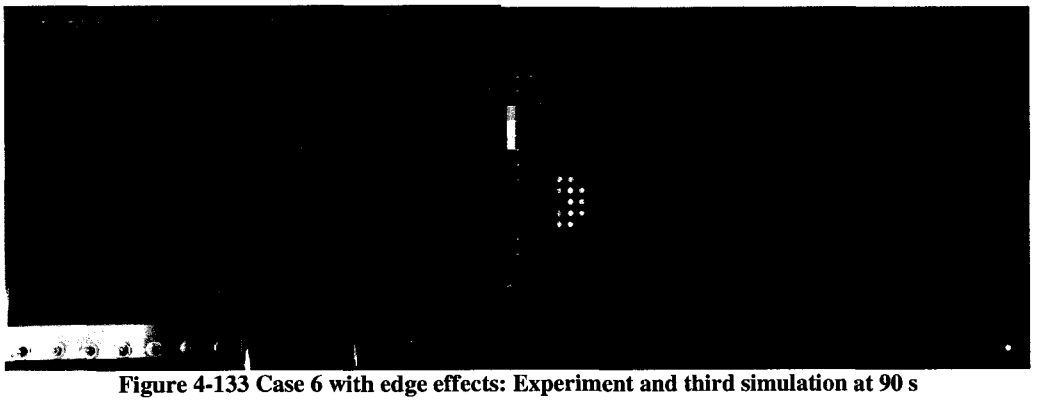

Figure 4-133 Case 6 with edge effects: Experiment and third simulation at 90 s

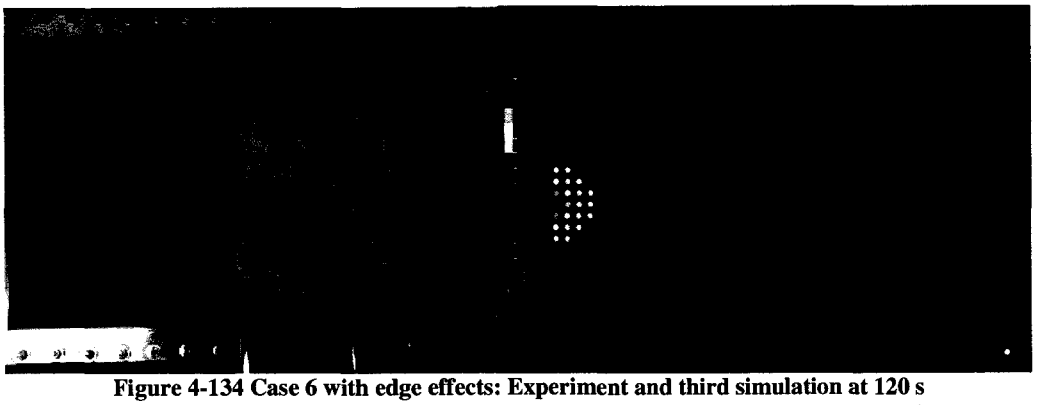

Figure 4-134 Case 6 with edge effects: Experiment and third simulation at 120 s

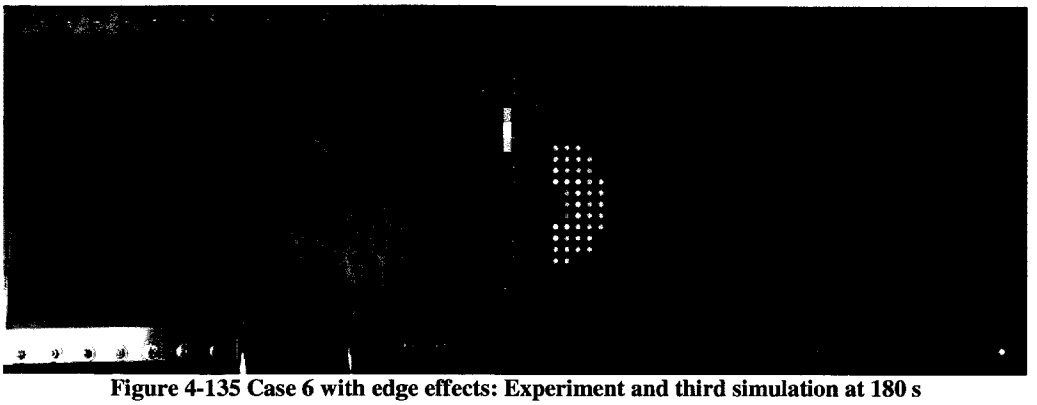

Figure 4-135 Case 6 with edge effects: Experiment and third simulation at 180 s

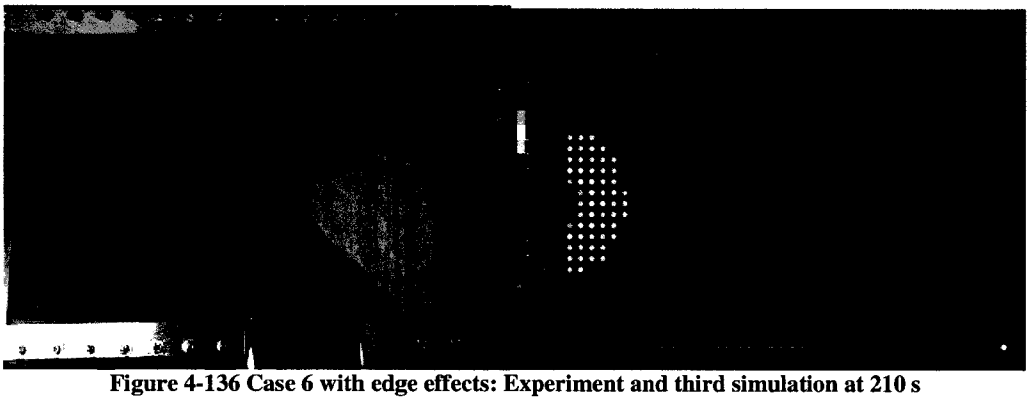

Figure 4-136 Case 6 with edge effects: Experiment and third simulation at 210 s

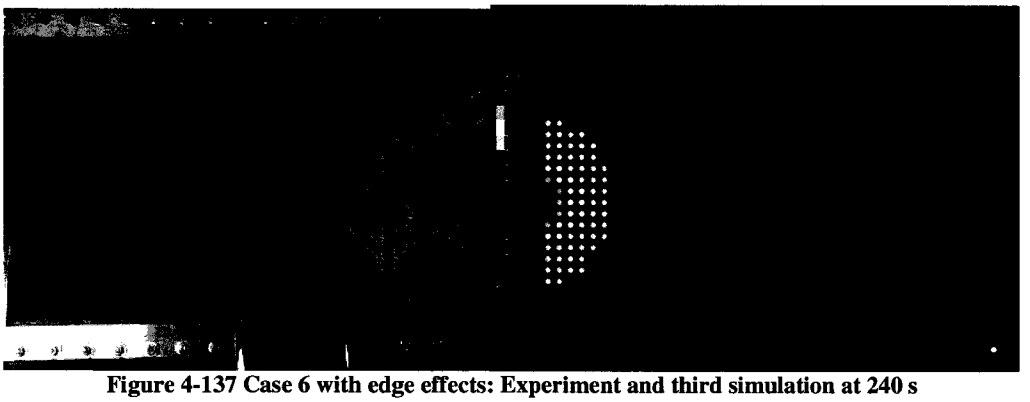

Figure 4-137 Case 6 with edge effects: Experiment and third simulation at 240 s

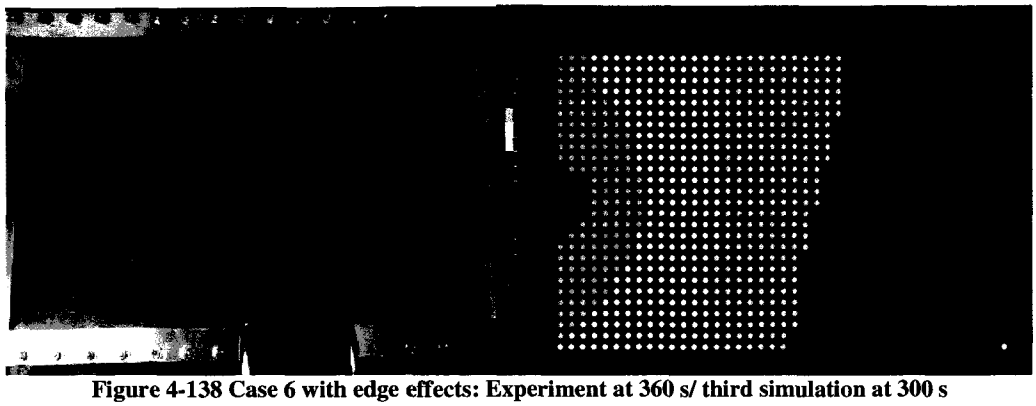

Figure 4-138 Case 6 with edge effects: Experiment at 360 s/ third simulation at 300 s

Due to the adjustments, the central flow was more closely simulated as the edge effect on the border of the 4-to-2 layers transition helped the flow to progress faster there than through other regions.

4.1.7 Case 7: 4 layers of unidirectional mat with a single inlet

Case 7 involves the use 2 layers of Reinforcement 2, which is TG18U50 woven glass fibre unidirectional mat supplied from JB Martin. It is important know how resin behaves on a unidirectional fabric since the permeability differs by a large factor within their orthogonal directions. Being able to simulate this situation is essential as such infusion process is very common in the industry. The experiment configuration was identical to that used in case 1. The permeability value along the length of the mould was set as $7.0\times10^{-12}\,m^2$ whereas the value along the width of the mould was set as $2.5\times10^{-12}\,m^2$. These values were determined by first measuring the length of major and minor axis of the elliptical saturated zone from the experiment and obtaining the

permeability ratio, then the ratio was used in Equation (2.47) to obtain the respective permeability values.

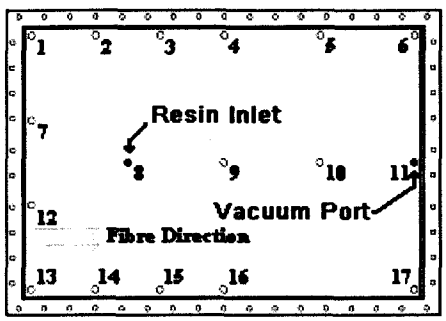

Figure 4-139 Case 7 configuration

The fibres were aligned along the length of the mould as shown in Figure 4-139; inner yarn channels cause the resin to travel faster along the length of the mould. This leads to the decrease in fill time compare to case 1. The flow front during infusion should feature an elliptical shape with its major axis being oriented along the length of the mould. Only one simulation was done for this particular case.

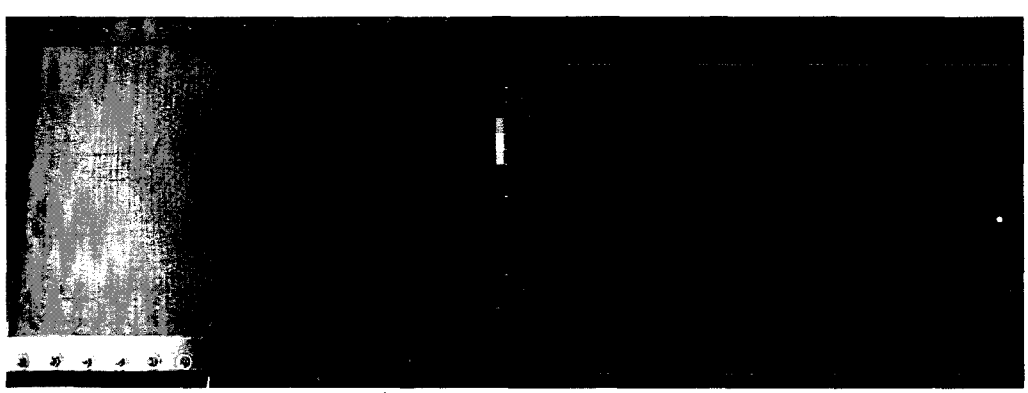

Figure 4-140 Case 7: Experiment and simulation at 0 s

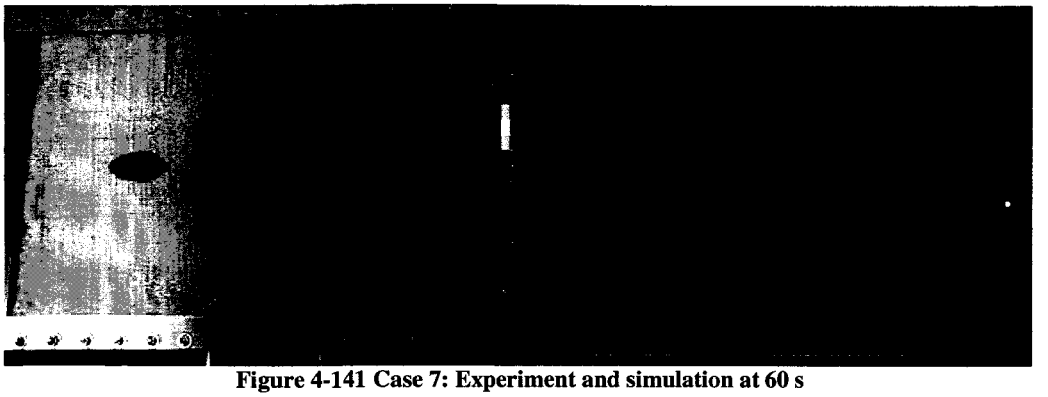

Figure 4-141 Case 7: Experiment and simulation at 60 s

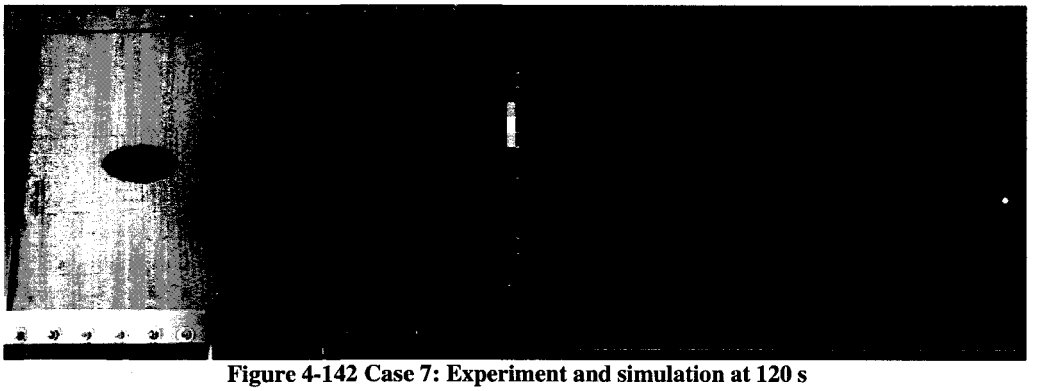

Figure 4-142 Case 7: Experiment and simulation at 120 s

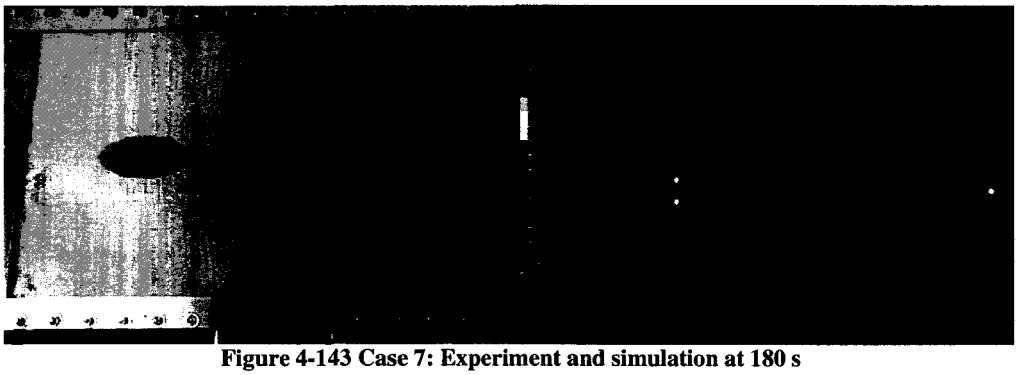

Figure 4-143 Case 7: Experiment and simulation at 180 s

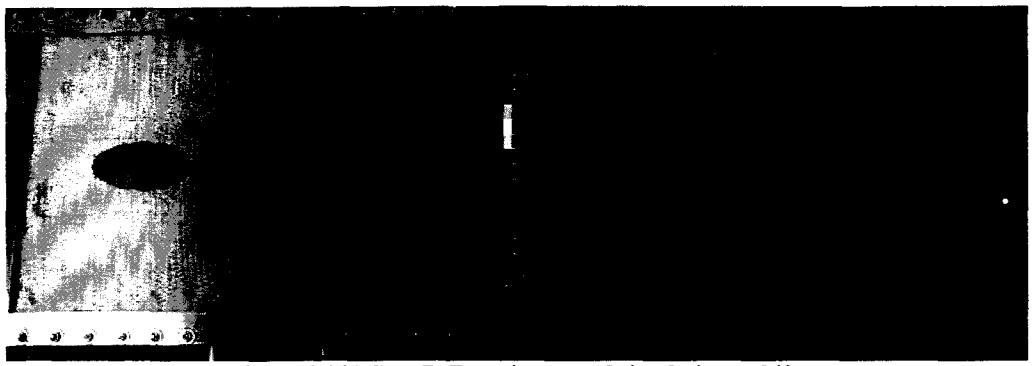

Figure 4-144 Case 7: Experiment and simulation at 240 s

Figure 4-145 Case 7: Experiment and simulation at 300 s

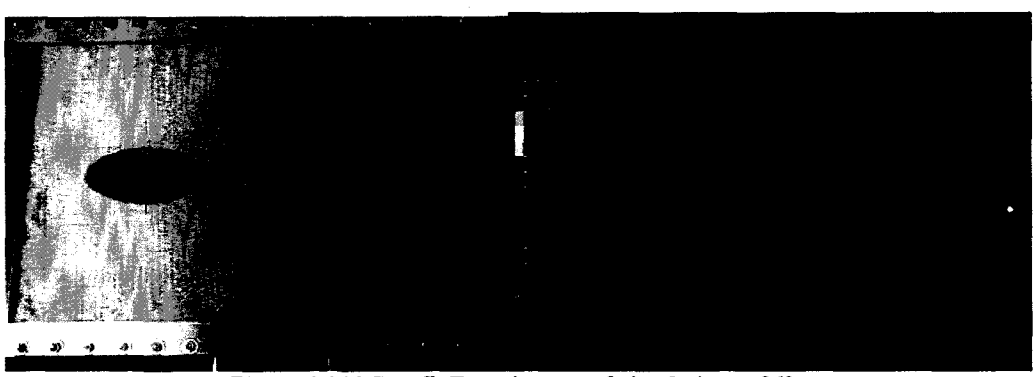

Figure 4-146 Case 7: Experiment and simulation at 360 s

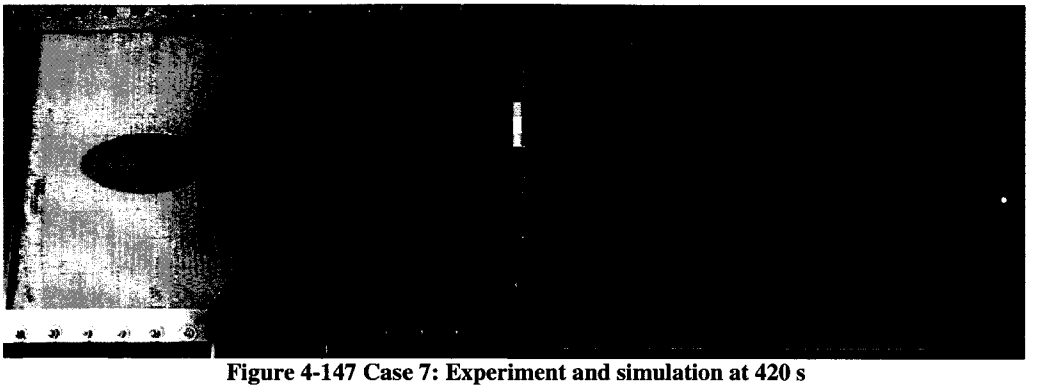

Figure 4-147 Case 7: Experiment and simulation at 420 s

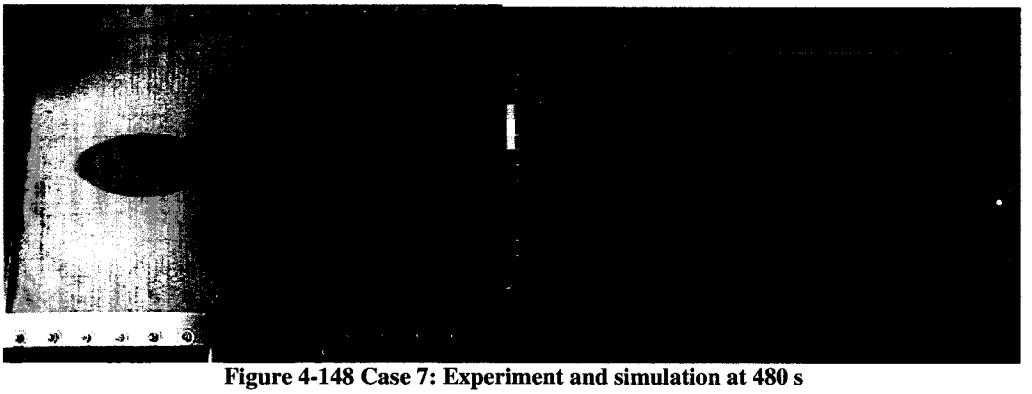

Figure 4-148 Case 7: Experiment and simulation at 480 s

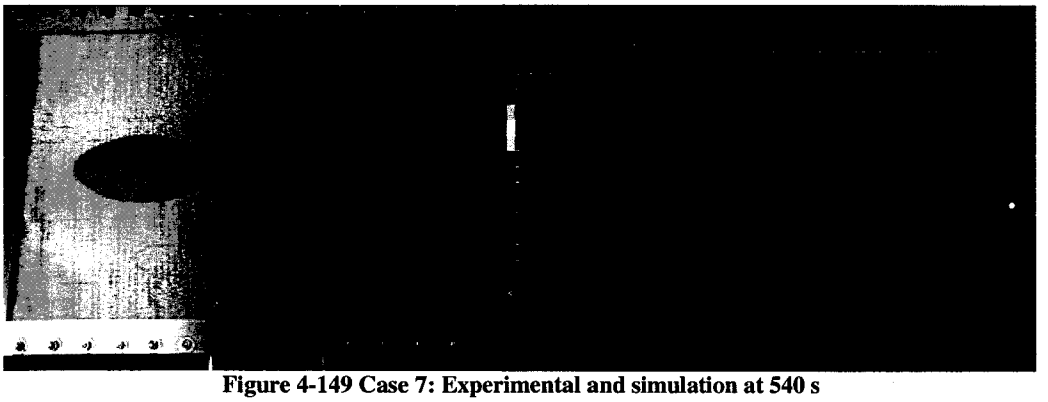

Figure 4-149 Case 7: Experimental and simulation at 540 s

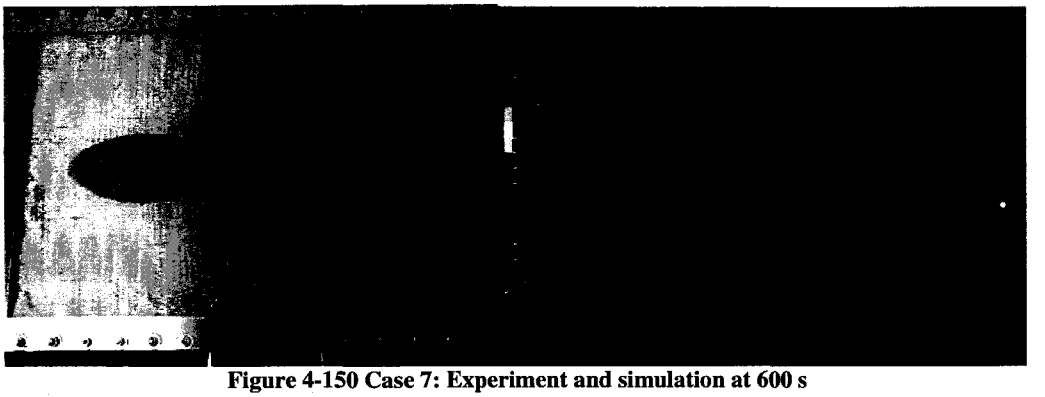

Figure 4-150 Case 7: Experiment and simulation at 600 s

Due to the fact that the permeability of the unidirectional fabric is much lower than that of Reinforcement 1, the velocity of the flow front was much slower than in experimental runs from the random mat cases. After 600 seconds, the movement of the flow front was hard to detect, and the recording capacity of the digital camera was exceeded after 900 seconds. The simulation showed very accurate results in terms of the fill time as well as the flow front shape up to this point. Although the experiment came to an end at 600 seconds, the simulation was continued until the mould was filled.

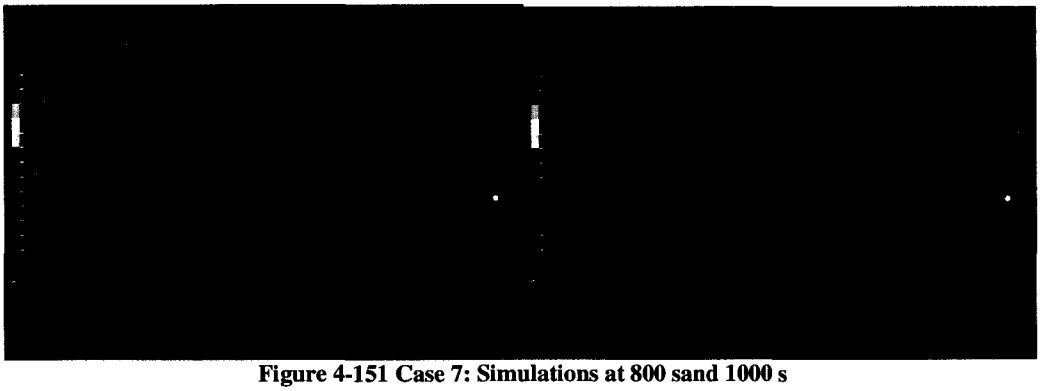

Figure 4-151 Case 7: Simulations at 800 sand 1000 s

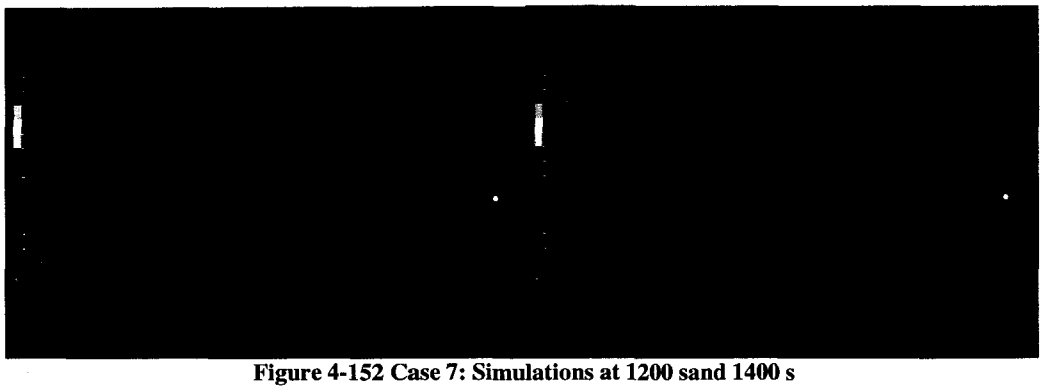

Figure 4-152 Case 7: Simulations at 1200 sand 1400 s

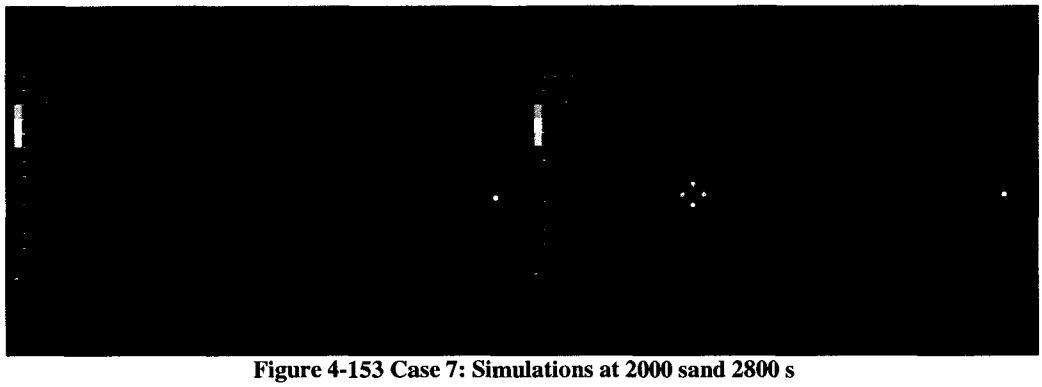

Figure 4-153 Case 7: Simulations at 2000 sand 2800 s

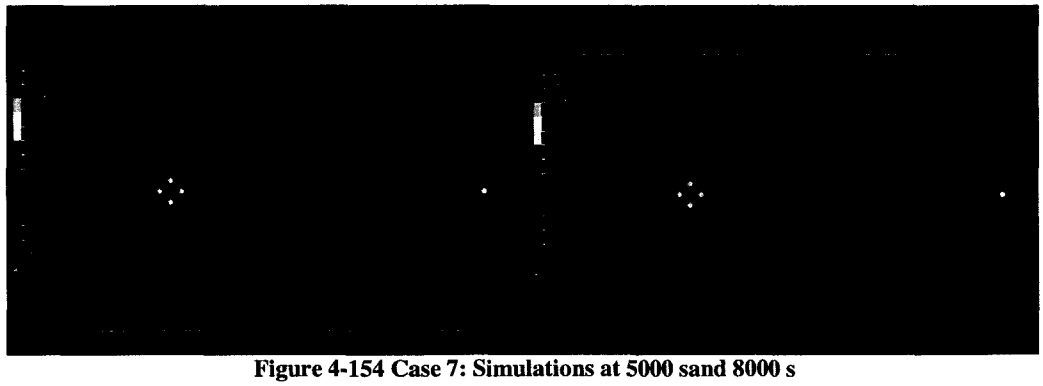

Figure 4-154 Case 7: Simulations at 5000 sand 8000 s

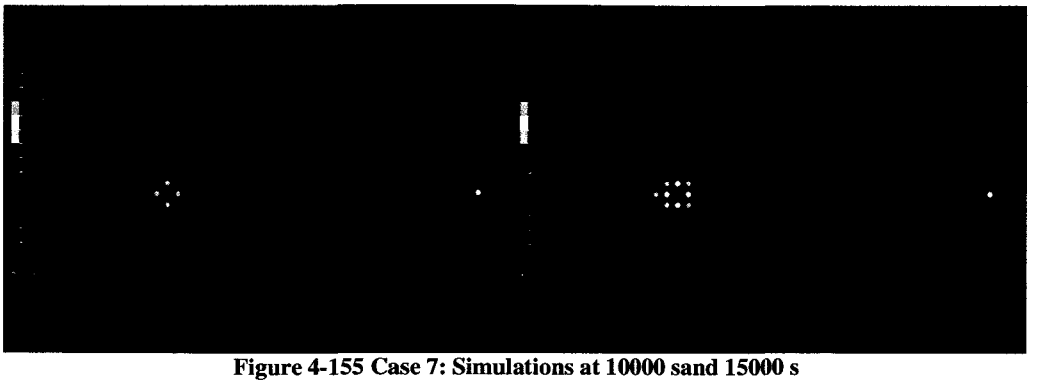

Figure 4-155 Case 7: Simulations at 10000 sand 15000 s

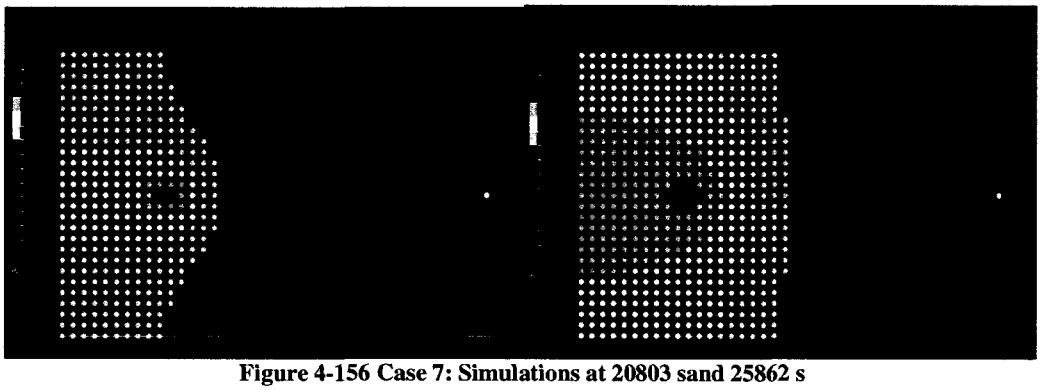

Figure 4-156 Case 7: Simulations at 20803 sand 25862 s

The total fill time required to infuse this particular fabric was near 26000 seconds - near 7.2 hours which is a very large amount of time. In a practical application, this is a highly undesirable situation. To avoid such a large amount of fill time, it is recommended to use multiple inlet ports during the infusion.

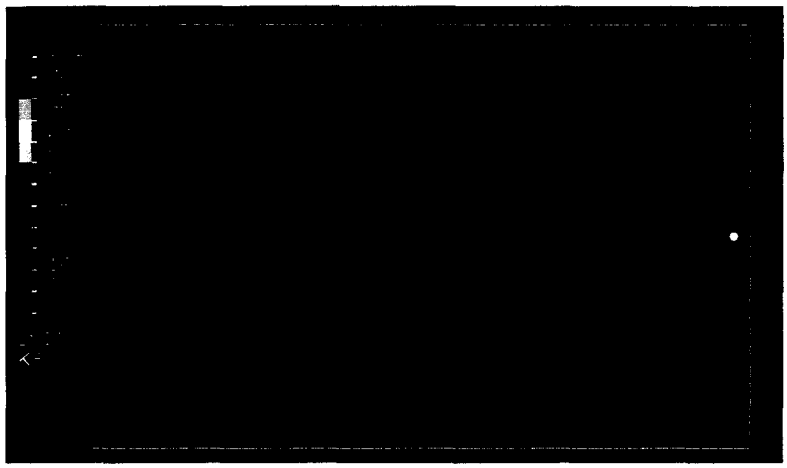

Figure 4-157 Use of multiple inlet ports to decrease the fill time

As seen in Figure 4-157, using 4 inlet ports located at key locations to distribute the resin evenly can help to decrease the fill time by a factor of 5.7.

The simulation capability was well validated by experimental runs. Flow front shapes obtained from simulations resembled those seen in actual experiments, and the overall pattern of the flow processes was well replicated. Furthermore, fill times in simulations were fairly close to the times obtained from the experimental runs. The edge effect phenomenon was also captured well within the software.

It should be clear that the above comment regarding fill times is made in a context of permeability data that was generated through a fitting procedure. There is no pretence that fill times were predicted as no permeability measurements were made. Beyond the increasing controversy over the value of such measurements, one of the main purposes of the software is to assist in locating ports and vents as opposed to predicting

fill times accurately. In situations where this is needed, as a result of variability over permeability measurement the safest practical option is to instrument the mould, monitor resin progress at specific locations in real time, and from these readings to determine the time that will be required to fill the mould in a specific instance.

As for edge effects, simulations replicated this effectively through a fitting procedure. Edge gap sizes never take a constant or well-defined values; needless to say that they are small, and effectively have more in common with a local reduction in porosity than with an actual gap. It is not practical, realistic or desirable to proceed to actual edge gap size measurement or estimation prior to simulations, and then to implement these values in simulations. A more realistic option consists in running simulations where different gap sizes are assumed, to assess their effect on the overall filling patterns, and to use the information in selecting robust locations for inlets and outlets – locations that ensure reliable filling of the cavity. The procedure performed in this thesis is similar to this. It is not worthwhile to use measured preform permeability values in simulations, due to the high variability and inaccuracy of these values. Thus, it is necessary to fit the permeability values of the simulation by measuring the flow front progression at the initial steps of the filling via sensors and scaling the permeability values appropriately.

As a final note, it should be noted that the work presented in this thesis constitutes a first step towards the development of a filling simulation software that will

be used for research purposes, where it is desirable to control the flow of data in its entirety, and to access to all the basic algorithms linked to the flow front progression.

4.2 VARTM Simulation in 1D

Upon validation of the iteration method introduced in section 2.12, the method was implemented in Visual C++ in order to create a 1D flow simulation of VARTM which includes flow front progression. The finite difference equations for obtaining the pressure field differed from those used for RTM due to the variable values of thickness, porosity and permeability. The relation was introduced as Equation (2.57). The equations were then solved using an explicit method described in section 2.12. In addition to the calculation shown in section 2.12, a time step was introduced in order to simulate 1D flow. At every time step, 60 iterations were done which was a sufficient number of iterations for the solution to converge. A 17-node 1D case was simulated using the same material parameters used in section 2.12, and the pressure versus distance curve was captured once a moving flow front filled an empty node. The time step used was 0.1 second. Figure 4-158 to Figure 4-163 show the iterative convergence of the resin pressure profile at a given time during the filling process. The curve fluctuates rapidly at the beginning as it converges towards the solution, but becomes steady near the end of the iteration. The purple diagonal line represents the analytical pressure field for the RTM case, and it is on display for comparison only.

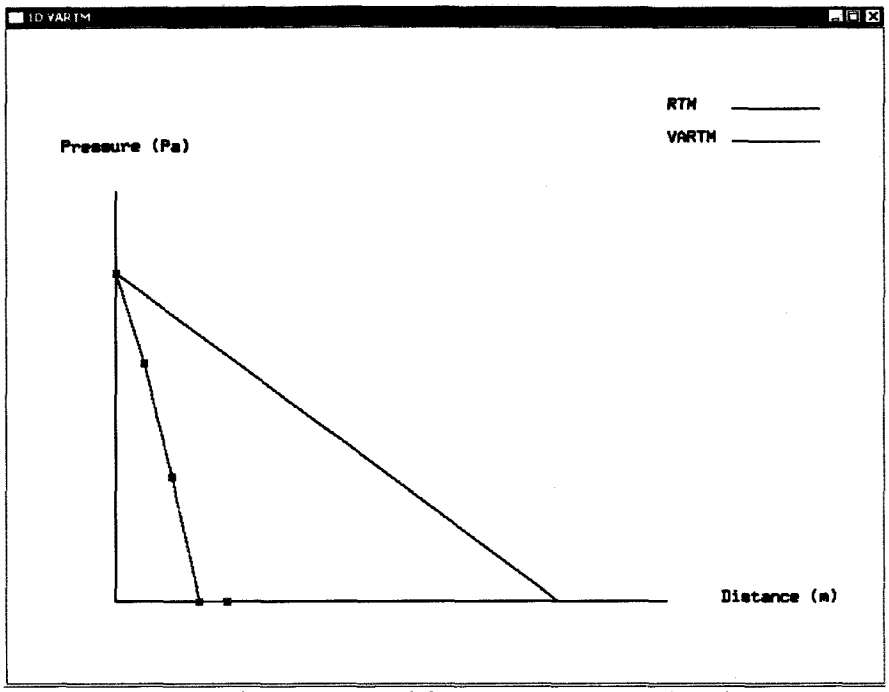

Figure 4-158 Convergence of the curve at time step 4, iteration 1

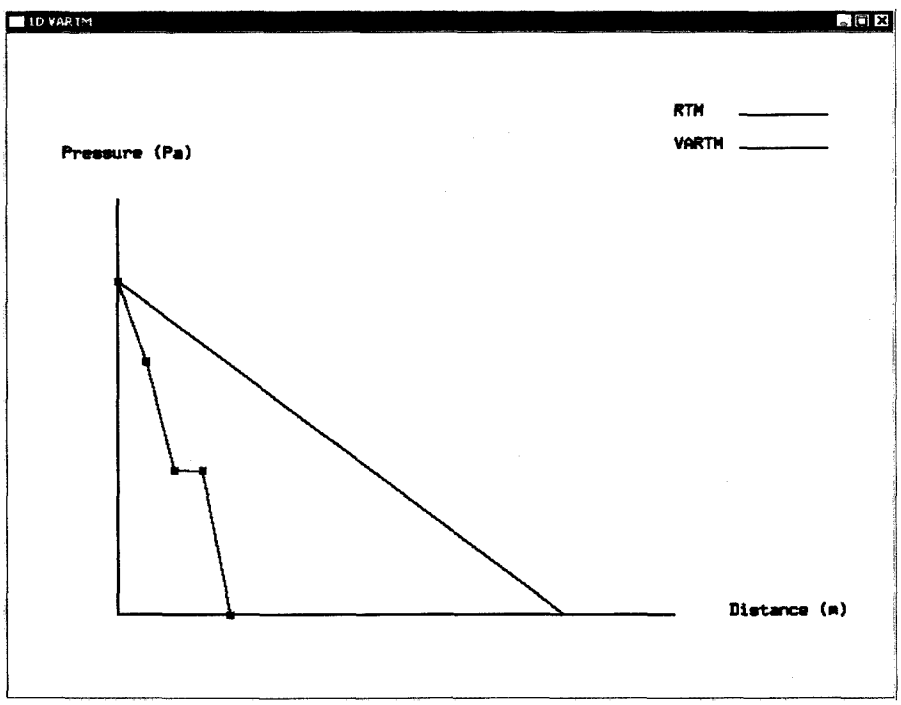

Figure 4-159 Convergence of the curve at time step 4, iteration 10

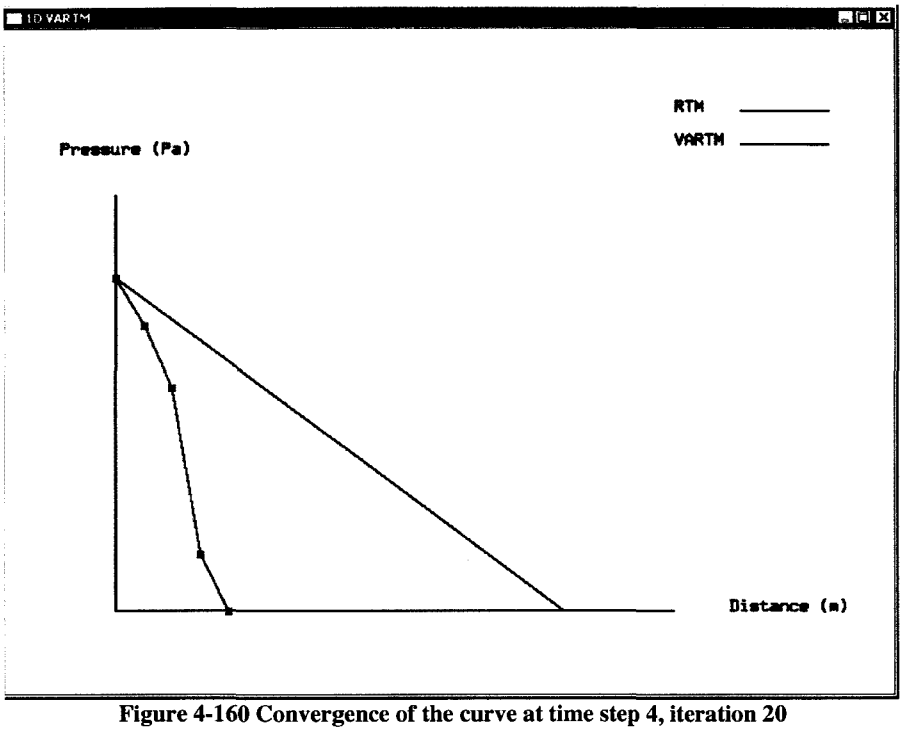

Figure 4-160 Convergence of the curve at time step 4, iteration 20

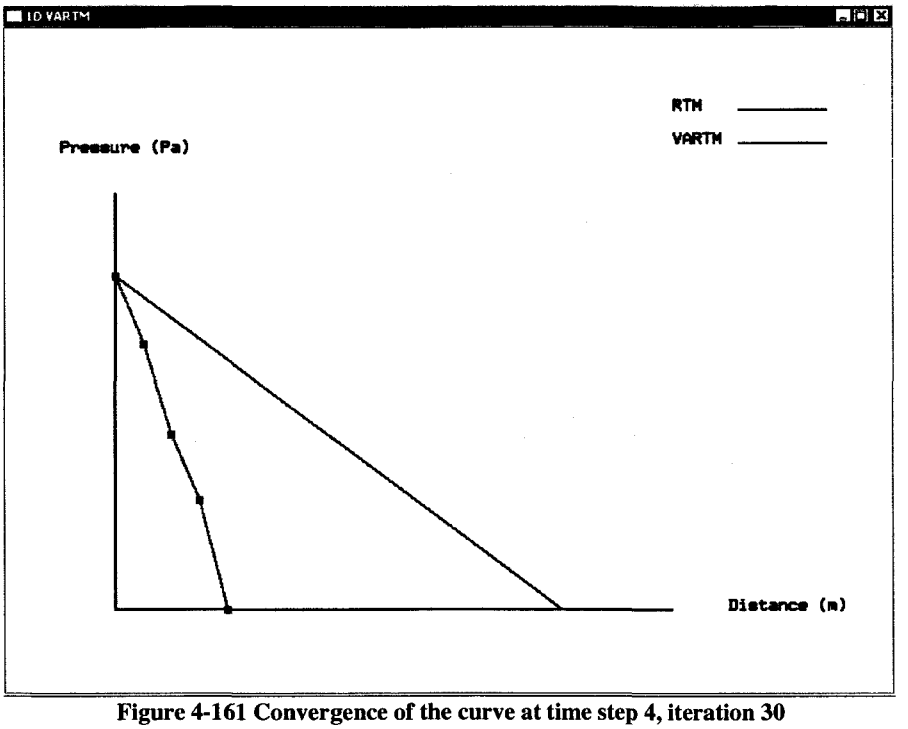

Figure 4-161 Convergence of the curve at time step 4, iteration 30

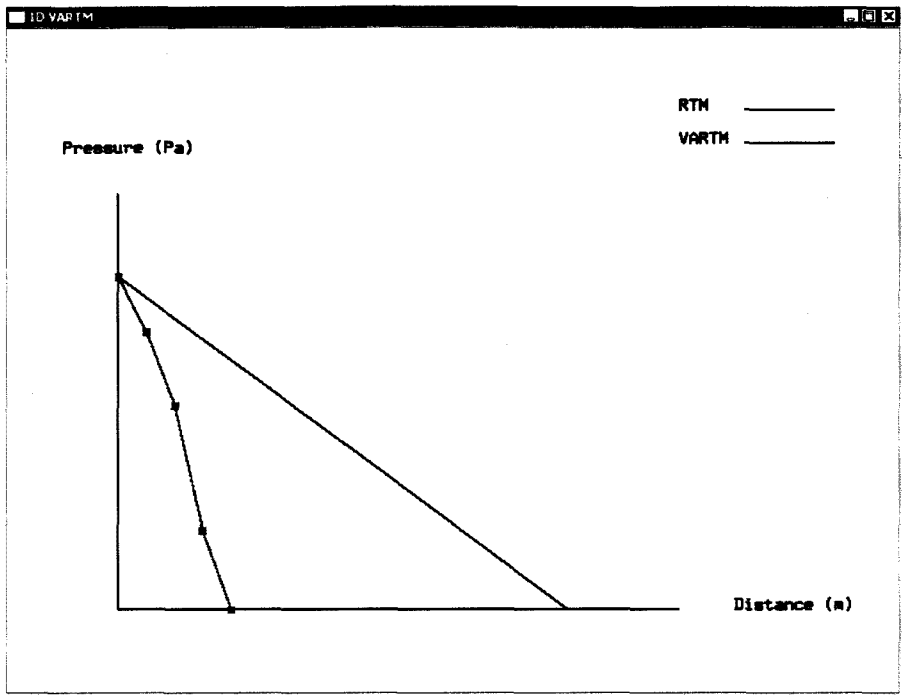

Figure 4-162 Convergence of the curve at time step 4, iteration 40

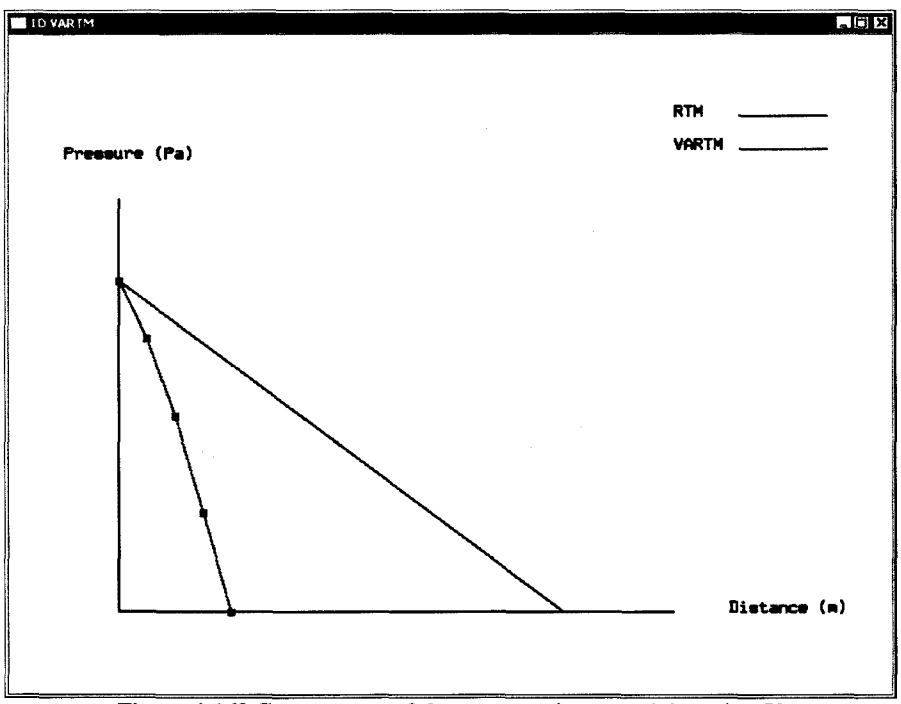

Figure 4-163 Convergence of the curve at time step 4, iteration 50

At the end of filling between nodes 5 and 6, the VARTM resin pressure profile became curved downwards, as analysis predicts that it should. Based on this behaviour of convergence, the evolution of the pressure curve with time was developed as shown in Figure 4-164.

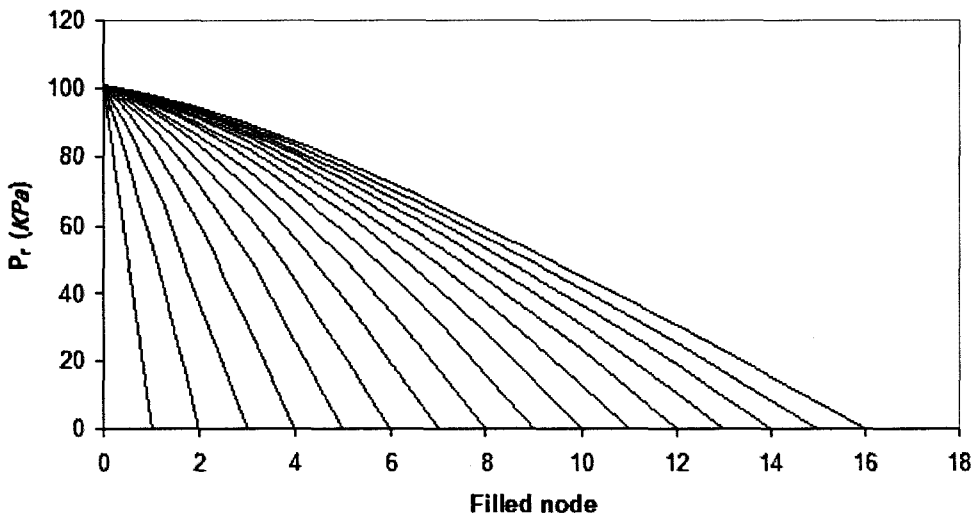

Figure 4-164 Evolution of resin pressure field during 1D VARTM flow

The time consumed for each node to be filled is tabulated in Table 4-1:

Table 4-1 Fill time during 1D VARTM flow

Nodes	Fill time (s)
1	0.0
2	2.7
3	4.1
4	5.3
5	6.4
6	7.6
7	8.6
8	9.8
9	11.0
10	12.3
11	13.8
12	15.4
13	17.1
14	19.0
15	21.0
16	23.2

In VARTM, the compaction pressure is the highest near the vent, thus the preform is compressed the most near the vent which causes the fibre volume fraction to be the highest. This can be seen in Figure 4-165, which is a plot yielded from the values obtained at the end of the simulation.

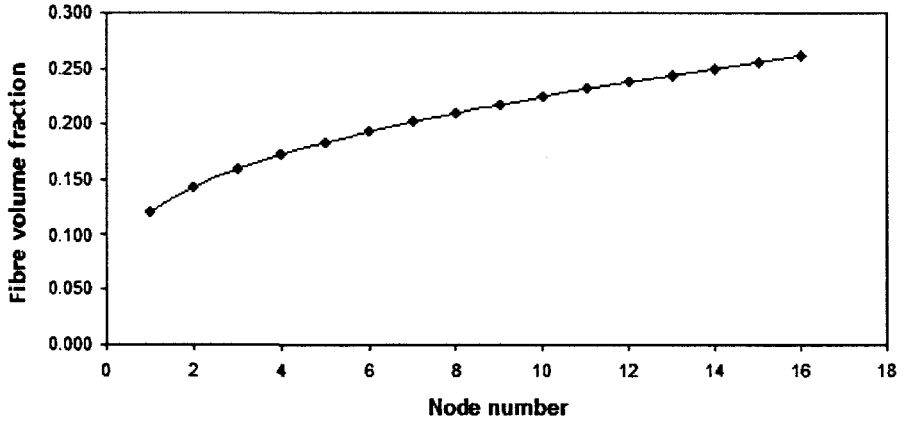

Figure 4-165 Fibre volume fraction (v_f) vs. node number

The permeability is also lowest when the compaction pressure is highest, making it difficult for the fluid to progress forward when the fabrics are compacted. This can be seen in Figure 4-166.

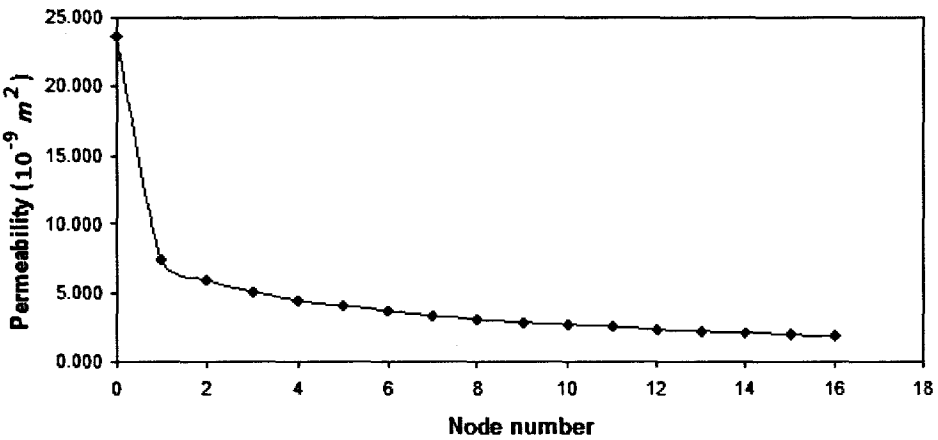

Figure 4-166 Permeability (*K*) vs. node number

Going back to the study that was done by Correia *et al* [42], the above graphs can be demonstrated to be valid. Referring back to Figure 2-23, it can be seen that the negative slope of the VARTM analytical curve increases as the flow moves further away from the inlet. The trend can be directly related to the increase in fibre volume fraction – equation (2.53) and decrease in permeability – equation (2.55), as the flow moves further away from the inlet. Experimental validation was not necessary for this simulation because of the fact that Correia's result have been well established and validated.

5 Conclusion and Recommendations

The main goal of this research was to develop a software for simulating the resin infusion during RTM and VARTM processes. Both cases involved the continuity and momentum equations which are fundamentals in fluid mechanics, as well as Darcy's law which is the base equation for flow through porous media. The partial differential equations developed from the continuity and momentum equations were discretized using the finite differences method.

For the simulations of RTM, these discretized algebraic equations were stored in a matrix and solved implicitly using the LU decomposition method. The solved values represented the pressure distribution within the meshed domain, and these values were used to push the flow front towards the unsaturated regions of the cavity. Visual C++ allowed the results to be seen graphically, where the user can clearly observe the shape of the flow front during the filling process, as well as the pressure distribution across the cavity. Fill times were inaccurate in some cases, but this was explained by the presence of edge effects. Edge effects occur during the filling process if the fabric is slightly smaller in size than the cavity itself – leaving say even a 0.1 mm gap between the cavity wall and the fabric creates a preferential flow path for the resin which leads to significant disruption of the filling process. The relation of Hagen-Poiseuille was used to simulate this effect during the filling process, hence the filling pattern as well as the fill time of simulations became satisfactorily close to the experimental results.

Simulations of VARTM in 1D involved slightly more complicated partial differential equations than the RTM case since the permeability and porosity do not remain constant during the filling process. Once the partial differential equation was properly discretized, the obtained algebraic equations were solved explicitly using the iteration method. Multiple iterations per time step eventually led to the convergence of solutions and the results matched well with the results from on credible sources. VARTM simulation was visually implemented as well where the compaction pressure versus the distance curve was updated continuously during the filling process, and it maintained the ideal pressure profile of parabolic shape throughout the entire process.

In future, assumed or measured preform permeability values should not be used during the simulations of RTM and VARTM. As discussed, measured values are highly variable and inaccurate. Instead, the flow front progression should be measured at the initial steps of filling via sensors, and the simulation should be capable of scaling the permeability values in order to match the fill time between these in-site measurement and simulations. Besides, the fill time estimation is not a very critical issue as long as the resin gel time is sufficiently long. The critical issue in RTM is the correct location of vents, and the software enables this. For VARTM, the software enables the quantification of local thickness in final parts. Regarding the software itself, many things are expected to be improved. For RTM simulations, a mesh refinement function at a selected regions should be implemented in order to greatly improve the accuracy of flow simulation near the inlet and outlet regions. Also, implementing curvilinear coordinates would increase the overall simulation capability as well. As for VARTM simulations, it is necessary to

expand the simulation tool in 2D as well as in curvilinear coordinates. Following the upgrades, a set of experiments should be done in order to validate the simulation results. In general, running the simulations on more powerful processors seems to be necessary as the computational power that was available during this work was not optimal. Hence, a greatly improved capability as well as shorter computational times can be expected using finer meshes. Final recommendation is to develop a graphical user interface for the software to make it friendlier towards the users.

References

[1] W. D. Callister Jr., in *Materials Science and Engineering*, (Ed: U. o. Utah), Wiley, Utah, USA **2003**.

[2] C. D. Rudd, A. C. Long, in *Liquid Moulding Technologies*, (Ed: U. o. Nothingham), Nottingham, UK **1997**.

[3] G. Shock, in *Reinforced Plastics for Commercial Composite Source Book*, (Ed: ASM), Metals Park, USA **1986**.

[4] H. Darcy, *Les Fontaines Publiques de la Ville de Dijon* **1856**.

[5] A. W. Chan, D. E. Larive, R. J. Morgan, *J. Compos. Mater* **1993**, *27*, 996

[6] C. Lekakou, M. A. K. Johari, D. Norman, M. G. Bader, *Composites A* **1996**, *27*, 401

[7] E. J. Carter, A. W. Fell, P. R. Griffin, J. Summerscales, *Composite A* **1996**, *27*, 255

[8] A. W. Chan, S. T. Hwang, *Polym. Eng. Sci.* **1991**, *31*, 1149

[9] J. P. Chick, C. D. Rudd, P. A. V. Leeuwen, T. I. Frenay, *Polym. Compos.* **1996**, *17*, 124

[10] J. R. Weitzenbock, R. A. Shenoi, P. A. Wilson, *Composites A* **1999**, *30*, 781

[11] J. R. Weitzenbock, R. A. Shenoi, P. A. Wilson, *Composites A* **1999**, *30*, 797

[12] K. L. Adams, B. Miller, L. Rubenfeld, *Polym. Eng. Sci* **1986**, 1434

[13] K. L. Adams, W. B. Russel, L. Rebenfeld, *Int. J. Multiphase Flow* **1988**, *14*, 203

[14] B. R. Gebart, P. Lidstrom, *Polym. Compos.* **1996**, *17*, 43

[15] P. Ferland, D. Guittard, F. Trochu, *Polym. Compos.* **1996**, *17*, 149

[16] R. S. Parnas, J. G. Howard, T. L. Luce, S. G. Advani, *Polym. Compos.* **1995**, *16*, 429

[17] T. S. Lundstrom, B. R. Gebart, E. Sandlund, *Polym. Compos.* **1999**, *20*, 146

[18] R. S. Parnas, K. M. Flynn, M. E. Dal-Favero, *Polym. Compos.* **1997**, *18*, 623

[19] R. V. Mohan, N. D. Ngo, K. K. Tamma, *Polym. Eng. Sci.* **1999**, *39*, 26

[20] R. Mathur, B. K. Fink, S. G. Advani, *Polym. Comops.* **1999**, *20*, 167

[21] M. Y. Lin, M. J. Murphy, H. T. Hahn, *Composites A* **2000**, *31*.

[22] X. L. Liu, *Composites A* **2000**, *31*, 1295

[23] B. Liu, S. Bickerton, S. G. Advani, *Composites A* **1996**, *27*, 135

[24] A. Boccard, W. I. .Lee, G. S. Springer, *J. Compos. Mater.* **1995**, *29*, 306

[25] J. Mogavero, J. Q. Sun, S. G. Advani, *Polym. Compos.* **1997**, *18*, 412

[26] J. P. Coulter, E. E. Higuerey, J. M. Troiano, H. H. Demicri, T. L. Nixon, *J. Mater. Process. Manuf. Sci.* **1997**, *5*, 173

[27] M. K. Kang, J. J. Jung, W. I. Lee, *Polym. Compos.* **2000**, *31*, 407

[28] S. Jiang, C. Zhang, B. Wang, *Composites A* **2002**, *33*, 471

[29] S. R. M. Kueh, R. S. Parnas, S. G. Advani, *Compos. Sci. Technol.* **2002**, *62*, 311

[30] E. M. Sozer, S. Bickerton, S. G. Advani, *Composites A* **2000**, *31*, 1383

[31] K. Han, L. J. Lee, *J. Comops. Mater.* **1996**, *30*, 1458

[32] D. R. Nielsen, R. Pitchumani, *Comops. Sci. Technol.* **2002**, *62*, 283

[33] K. Han, L. J. Lee, *J. Compos. Mater.* **1996**, *30*, 1475

[34] D. Abraham, R. McIlhagger, *Composites A* **1998**, *29*, 533

[35] C. Binetruy, J. Pabiot, (Ed: I. C. f. C. Materials), Paris, France **1999**, 178.

[36] R. Gauvin, A. Kerachni, B. Fisa, *J. Reinf. Plast. Compos.* **1994**, *13*, 371

[37] S. Ranganathan, R. G. Easterling, S. G. Advani, F. R. Phelan Jr., *Polym. Polym. Compos.* **1998**, *6*, 63

[38] T. D. Papathanasiou, P. D. Lee, *Polym. Compos.* **1997**, *18*, 242

[39] T. S. Lundstrom, B. R. Gebart, *J. Compos. Mater.* **1995**, *29*, 424

[40] T. S. Lundstrom, R. Stenberg, R. Bergstrom, H. Partanen, P. A. Birkeland, in *International Committtee for Composite Materials*, Paris, France **1999**, 309.

[41] V. Stanek, J. Szekel, *A.I.Ch.Eng. J.* **1974**, *20*, 974

[42] N. C. Correia, F. Robitaille, A. C. Long, C. D. Rudd, *Journal of Fluids Engineering* **2004**, *126*, 210

[43] T. S. Lundstrom, *Composites A* **2000**, *31*, 1345

[44] M. T. Senoguz, F. D. Dungan, A. M. Sastry, J. T. Klamo, *J. Compos. Mater.* **2001**, *35*, 1285

[45] A. C. Long, F. Robitaille, B. J. Souter, C. D. Rudd, in *Proc. TEXCOMP 5*, KLI Leuven, Leuven, Belgium **2000**.

[46] A. C. Long, F. Robitaille, B. J. Souter, C. D. Rudd, in *Proc. ICCM 13*, International Committee for Composite Materials, Beijing, China **2001**.

[47] F. Robitaille, A. C. Long, B. J. Souter, C. D. Rudd, in *Proc. ECCM 9*, Institute of Materials, Brighton, UK **2000**.

[48] F. Robitaille, A. C. Long, C. D. Rudd, in *Proc. 17th Conf.*, Polymer Processing Society, Montreal, Canada **2001**.

[49] F. Robitaille, A. C. Long, C. D. Rudd, B. J. Souter, in *Proc. ICMAC 2001*, Insititute of Materials, Belfast, UK **2001**, 91

[50] F. Robitaille, A. C. Long, C. D. Rudd, *Plastics, Rubber and Composites* **2002**, *13*, 238

[51] F. Robitaille, B. J. Souter, A. C. Long, C. D. Rudd, in *Proc. ICAC 98*, Hurgadah, Egypt **1998**, 251

[52] J. D. Anderson Jr., in *Computational Fluid Dynamics*, (Eds: J. P. Holman, J. R. Lloyd), McGraw-Hill, New York **1995**, 168

[53] J. J. D. Anderson, in *Mechanical Engineering*, McGraw - Hill, Singapore **1995**.

[54] J. D. Anderson Jr., in *Computational Fluid Dynamics*, (Eds: J. P. Holman, J. R. Lloyd), McGraw-Hill, New York **1995**, 77

[55] A. J. E. J. Dupuit, *Etudes Theoriques et Pratiques sur le Mouvement des aus dans les Canaus Decouverts et a Travers les Terrains Permeables.*

[56] P. Forchheimer, W. d. Boden, *Zeitschrift des Vereines Deutscher Ingenieure* **1901**, *45*, 1736

[57] R. L. Street, G. Z. Watters, J. K. Vennard, in *Elementary Fluid Mechanics*, Wiley, New York **1996**.

[58] B. R. Gebart, *J. Compos. Mater* **1992**, *26*, 1100

[59] A. W. Chan, D. E. Larive, R. J. Morgan, *Journal of Composite Materials* **1993**, *27*, 996

[60] A. Hammami, B. R. Gebart, *Polymer Comopsites* **2000**, *21*, 28

[61] T. G. Gutowski, G. Dillon, *Advanced Composites Manufacturing* **1997**, 138

[62] F. Robitaille, R. Gauvin, *Polymer Comopsites* **1998**, *19*, 198

[63] Dow Epoxy, in *Dow Epoxy Product Finder*, **2009**.

[64] I. Clearco, in *http://www.clearcoproducts.com/silicones_library.html*, **2009**, Viscosity Temperature Coefficient.

[65] J. Breard, *Materiaux composites a matrice polymere: Modelisation numerique de la phase de remplissage du procede RTM et determination experimentale de la permeabilite d'un renfort fibreux* **1997**.

[66] K. Hoes, *Development of a new sensor-based set-up for experimental permeability identification of fibrous media* **2003**.

[67] T. Luthy, *Computer methods in composite materials* **1998**, 433.

[68] R. Pan, Z. Liang, C. Zhang, B. Wang, *Polymer Comopsites* **2000**, *21*, 996.

[69] R. Gauvin, A. Kerachni, B. Fisa, *Reinforced Plastics and Composites* **1994**, *13*, 371

[70] J. Merotte, P. Simacek, G. Advani, *Composite A* **2009**.

Appendix

LU Decomposition Method

Once the finite differences method is applied over the meshed surface, a series of linearly independent equations are formulated. These equations are then stored in 3 matrices; the first matrix stores the coefficients of all unknown pressures, which can become enormously large if the mesh size is large. To solve such large sets of equations, thousands of repetitive calculations are needed – if it were to be solved in "traditional" way. However, many efficient numerical methods exist at present day, and with the exceptional computational power that is available, these calculations can be done in much less painful manner. The particular method that is implemented in this work is the LU decomposition method. LU – stands for lower and upper – decomposition is a method of solving a large set of linearly independent equations by breaking up the matrix into 2 matrices which contain the lower half triangle in one, and the upper half triangle in the other.

$$\begin{bmatrix} \alpha_{11} & 0 & 0 & 0 \\ \alpha_{21} & \alpha_{22} & 0 & 0 \\ \alpha_{31} & \alpha_{32} & \alpha_{33} & 0 \\ \alpha_{41} & \alpha_{42} & \alpha_{43} & \alpha_{44} \end{bmatrix} \cdot \begin{bmatrix} \beta_{11} & \beta_{12} & \beta_{13} & \beta_{14} \\ 0 & \beta_{22} & \beta_{23} & \beta_{24} \\ 0 & 0 & \beta_{33} & \beta_{34} \\ 0 & 0 & 0 & \beta_{44} \end{bmatrix} = \begin{bmatrix} a_{11} & a_{12} & a_{13} & a_{14} \\ a_{21} & a_{22} & a_{23} & a_{24} \\ a_{31} & a_{32} & a_{33} & a_{34} \\ a_{41} & a_{42} & a_{43} & a_{44} \end{bmatrix}$$

Figure A-0-1 LU decomposition

The reason for breaking up the matrix in two is because of the fact that the solution of a triangular set of equations is trivial. Since the matrix A is a product of two triangle matrices,

$$LU = A$$

this can easily be decomposed to solve the linear set,

$$Ax = (LU)x = L(Ux) = b$$

First, solving for the vector y such that

$$Ly = b$$

Then solving for the vector x,

$$Ux = y$$

Thus the above two equations can be solved by forward substitution and back substitution, respectively.

$$y_1 = \frac{b_1}{\alpha_{11}}$$

$$y_i = \frac{1}{\alpha_{ii}}\left[b_i - \sum_{j=1}^{i-1} \alpha_{ii} y_j \right]$$

$$i = 2, 3, ..., N$$

$$x_N = \frac{y_N}{\beta_{NN}}$$

$$x_i = \frac{1}{\beta_{ii}}\left[y_i - \sum_{j=i+1}^{N} \beta_{ij} x_j \right]$$

$$i = N-1, N-2, ..., 1$$

With this method, linear matrix equations of any size can be solved as long as the matrix is not singular. The availability of a powerful processors in current computer systems have allowed large matrices to be stored and inverted to obtain the solutions.